

## ABSTRACT

Title of Dissertation: TOMOGRAPHIC MEASUREMENT OF THE PHASE SPACE DISTRIBUTION OF A SPACE-CHARGE-DOMINATED BEAM

Diktys Stratakis, Doctor of Philosophy, 2008

Dissertation Directed By: Professor & Chair, Patrick G. O'Shea  
Professor, Rami A. Kishek  
Department of Electrical and Computer Engineering

Many applications of accelerators, such as free electron lasers, pulsed neutron sources, and heavy ion fusion, require a good quality beam with high intensity. In practice, the achievable intensity is often limited by the dynamics at the low-energy, space-charge dominated end of the machine. Because low-energy beams can have complex distribution functions, a good understanding of their detailed evolution is needed. To address this issue, we have developed a simple and accurate tomographic method to map the beam phase using quadrupole magnets, which includes the effects from space charge. We extend this technique to use also solenoidal magnets which are commonly used at low energies, especially in photoinjectors, thus making the diagnostic applicable to most machines. We simulate our technique using a particle in cell code (PIC), to ascertain accuracy of the reconstruction. Using this diagnostic we report a number of experiments to study and optimize injection, transport and acceleration of intense space charge dominated beams. We examine phase mixing, by

studying the phase-space evolution of an intense beam with a transversely nonuniform initial density distribution. Experimental measurements, theoretical predictions and PIC simulations are in good agreement with each other. Finally, we generate a parabolic beam pulse to model those beams from photoinjectors, and combine tomography with fast imaging techniques to investigate the time-sliced parameters of beam current, size, energy spread and transverse emittance. We found significant differences between the slice emittance profiles and slice orientation as the beam propagates downstream. The combined effect of longitudinal nonuniform profiles and fast imaging of the transverse phase space provided us with information about correlations between longitudinal and transverse dynamics that we report within this dissertation.

TOMOGRAPHIC MEASUREMENT OF THE PHASE SPACE DISTRIBUTION OF  
A SPACE-CHARGE-DOMINATED BEAM

By

Diktys Stratakis

Dissertation submitted to the Faculty of the Graduate School of the  
University of Maryland, College Park, in partial fulfillment  
of the requirements for the degree of  
Doctor of Philosophy  
2008

Advisory Committee:  
Professor Patrick G. O'Shea, Chair/Advisor  
Professor Rami A Kishek, (co-advisor)  
Professor Thomas M. Antonsen  
Professor Victor L. Granatstein  
Professor Richard F. Ellis

© Copyright by  
Diktys Stratakis  
2008



# Dedication

To my Mom and Dad,  
Mary and Emmanuel Stratakis

## Acknowledgements

The writing of a PhD dissertation can be a lonely experience, but it is obviously not possible without the support of numerous people. I would like to express my appreciation to Professor Patrick O'Shea, for his role as advisor and teacher. He provided a positive environment that I was seeking for so many years before, which allowed me to finish my work smoothly. I am deeply indebted to Prof. Rami Kishek for the countless hours we spent working together and for his continuous encouragements throughout the course of my research. I wish to thank Prof. Martin Reiser for his advice and suggestions over the last years. His expertise in the field of beam physics significantly influenced my research and the writing of this dissertation. I am honored to Dr. Irving Haber by his support and daily interaction. His experiences in beam physics made my research for this dissertation more efficient. I am grateful to Dr. Mark Walter. His assistance with hardware support was tremendous. Many thanks go to Dr. Hui Li who was the one who did the first steps in beam tomography for intense beams and provided incredible assistance during my first months in Maryland. I wish to thank Dr. Ralph Fiorito for his assistance with imaging techniques and cameras. I wish also to thank Brian Beaudoin and Brian Quinn for their suggestions and electrical support. I wish to thank Dr. Santiago Bernal for his valuable suggestions in my experiments. I benefited greatly from discussions with my officemate Chris Papadopoulos and I wish to thank him for that. I wish to thank my colleagues, also PhD students, Kai Tian and Charles Thangaraj for their valuable help during my experiments but also in the data analysis. I am especially grateful to Prof. Agis Iliadis for motivating me to apply to University

of Maryland and for his guidance, support and motivation during my first year in Maryland. Thanks also to Dr. D. Feldman, R. Feldman, Dr. N. Moody, Dr. D. Sutter, D. Cohen, Dr. T. Godlove, Dr. J. Newman, G. Bai who contributed to this dissertation in different ways. I wish to thank S. Lund from Berkeley National Lab for his valuable suggestions in improving the tomography diagnostic. Finally, I thank my friend Dr. Seok Jin Kim for the countless numbers we spent discussing the past, the present and the future.

Most of all I wish to thank my parents Mary and Emmanuel for their motivation, encouragement and support over those years. They were the source of my strength and happiness.

# Table of Contents

Table of Contents .....	v
List of Tables .....	ix
List of Figures .....	x
Chapter 1 Introduction .....	1
1.1 Electron Beam Properties .....	3
1.1.1 Transverse Phase Space .....	3
1.1.2 Beam Emittance .....	4
1.1.3 Beam Brightness .....	5
1.2 The Importance of the Phase Space Distribution.....	6
1.3 Beams with Space-Charge .....	7
1.4 Standard Techniques for Phase Space Mapping and Emittance Measurement ..	9
1.4.1 Quadrupole Scan.....	9
1.4.2 Pepper-pot .....	11
1.4.3 Slit-Scanner.....	12
1.5 History of Phase Space Tomography.....	13
1.6 Dissertation Overview .....	15
Chapter 2 Tomography Theory.....	19
2.1 Basic Theory .....	20
2.1.1 Beam Transfer Matrices.....	20
2.1.2 Space-charge Effects on Particle Motion.....	22
2.2 Tomography for Beams without Space-Charge.....	25
2.2.1 Filtered-Backprojection Algorithm.....	25
2.2.2 Extension of Tomography to Beam Physics .....	28
2.2.3 Example: Tomography with Quadrupoles .....	31
2.3 Tomography Extension to Beams with Space-Charge .....	36
2.4 Practical Tomography .....	39
2.4.1 Limitations .....	39
2.4.2 Tomography Configuration for UMER .....	40
2.4.3 Image Processing Requirements .....	42

2.4.4 Image Analysis Software .....	44
2.5 Summary .....	47
Chapter 3 Tomography Simulation.....	48
3.1 WARP Simulation .....	49
3.2 Error Analysis .....	51
3.2.1 Angular Resolution .....	52
3.2.2 Angular Span .....	54
3.2.3 Magnet Settings .....	55
3.3 Verification of Space-Charge Reconstruction .....	56
3.4 Initial Distributions .....	61
3.4.1 Semi-Gaussian Distribution .....	62
3.4.2 Hollow Velocity Distribution .....	62
3.4.3 Hollow Spatial Distribution .....	64
3.4.4 Five-Beamlet Distribution .....	65
3.4.5 Conclusion .....	69
3.5 Transverse Density Waves.....	69
3.6 Summary .....	73
Chapter 4 Tomographic Measurement of Phase-Space Evolution for Space-Charge Dominated Beams .....	74
4.1 University of Maryland Electron Ring (UMER) .....	75
4.2 Available Diagnostics in the Experiment .....	79
4.2.1 Bergoz Coil .....	79
4.2.2 Beam Position Monitors .....	79
4.2.3 Screens .....	80
4.3 Image Acquisition and Processing.....	81
4.3.1 Camera and Lenses .....	82
4.3.2 Video Capture and Camera Control.....	84
4.3.3 Image Acquisition Software .....	84
4.3.4 Tomography Automation.....	86
4.4 Beam Characterization near the UMER source – Tomography Verification...	87

4.4.1 Pinhole Scan.....	88
4.4.2 Phase Space at the Aperture by Tomography .....	94
4.5 Evolution of intense space-charge beams on UMER .....	96
4.5.1 Tomography Configuration and Phase Space Reconstruction.....	97
4.5.2 Phase Space Evolution of a Uniform Beam on UMER .....	99
4.5.3 Phase Space Evolution of a Nonuniform Beam on UMER .....	106
4.6 Summary .....	113
Chapter 5 Solenoidal Tomography .....	114
5.1 Principles of Solenoidal Tomography .....	115
5.1.1 Particle motion in Solenoidal Systems .....	115
5.1.2 Solenoidal Tomography for Beams with Space-Charge.....	119
5.2 Simulation and Validation of Solenoidal Tomography .....	121
5.2.1 Axisymmetric Distributions.....	123
5.2.2 Non-symmetric Distributions.....	125
5.3 Long Solenoid Experiment (LSE) .....	127
5.4 Experimental Results .....	131
5.4.1 “Uniform” Aperture .....	131
5.4.2 Emittance Growth .....	139
5.4.3 “Exotic” Beam Distributions .....	141
5.5 Summary .....	144
Chapter 6 Time-Resolved Tomography for Intense Particle Beams .....	146
6.1 Experiment Details .....	147
6.1.1 Fast Screens .....	147
6.1.2 Imaging .....	148
6.1.3 Generation of Longitudinal Perturbations .....	149
6.2 Longitudinal Perturbation Study.....	150
6.2.1 Time resolved (slice) tomography .....	151
6.2.2 Time integrated tomography.....	156
6.3 Parabolic Beam Pulse .....	159
6.4 Conclusion .....	166

Chapter 7 Summary and Conclusion .....	168
Appendix A: MATLAB Tomography Codes .....	173
A1: Code for calculation of scaling factors and rotation angles.....	173
A2: Code to calculate beam size, beam envelope slope and emittance .....	185
Appendix B: Camera Operating Procedures.....	187
Appendix C: XCAP Automation .....	189
Bibliography .....	195

## List of Tables

Table 3.1: Assumptions made to generate the beam phase space by WARP (left) and tomography (right).....	50
Table 3.2: Beam parameters of our simulated beams. Note that the beam is assumed to be round, initially.....	57
Table 3.3 Emittances obtained by WARP and Tomo-Code .....	61
Table 3.4: Beam parameters for the 7 mA beam. ....	62
Table 3.5: Emittances obtained from the phases-spaces in Fig. 3.9 by WARP and tomography .....	69
Table 3.6: Beam emittances at different positions along the beam line as calculated from the phase spaces generated by tomography and WARP .....	71
Table 4.1: UMER design parameters.....	77
Table 4.2: UMER Beam Parameters for the 10 keV beam.....	78
Table 4.3: Beam parameters from the pinhole scan.....	94
Table 5.1: Beam parameters used in the simulation .....	124
Table 5.2: Fitting parameters of the two short solenoids on the LSE.....	129
Table 5.3: Solenoid strengths and corresponding emittance measurements along the x axis from tomography and simulation. ....	136
Table 5.4: Solenoid strengths and corresponding emittance measurements along the y axis from tomography and simulation. ....	136
Table 5.5: Solenoid strengths and corresponding emittance measurements along x-axis from tomography for the multi-beamlet experiment. ....	144
Table 6.1: Beam parameters measured at the aperture from tomography. ....	153
Table 6.2: Beam currents and parameters measured at the aperture from tomography. ....	161



## List of Figures

Figure 1.1: Phase-space along the transverse direction $x$ . When forces are linear it can be approximated by a uniform ellipse (red line).....	4
Figure 1.2: Initially we have five distinct beamlets in configuration space. Downstream the beamlets merge in configuration space but are still separated in phase space.....	7
Figure 1.3: Example of the quadrupole scan. The beam size $X_{\text{rms}}^2$ is plotted versus the magnet focusing strength and a fit line (shown in red) is plotted through the actual data (black dots). From the fit line and Eq. 1.8 we can get the beam emittance. ....	10
Figure 1.4: Layout of the pepper-pot concept.....	11
Figure 1.5: Scanned wire diagnostic layout, adapted from ref. 16. ....	13
Figure 2.1: Layout showing a particle that enters a lens at $z_0$ and exits the lens at $z_1$ . ....	21
Figure 2.2: Illustration of the Radon Transform.....	26
Figure 2.3: Schematic layout of the beam transport line. The starting location is at $z_0$ and ending location is at $z_1$ . ....	29
Figure 2.4: Schematic layout of the beamline between $z_0$ and $z_1$ . The arrows at the bottom represent the transport matrices.....	33
Figure 2.5: Example demonstrating the procedure to obtain projections of the phase-space distribution. ....	35
Figure 2.6: Reconstructed phase space at $z_0$ by processing 87 projections after rotating the phase space by a full $180^\circ$ angle. The intensity parameter was 0.3 and the beam was emittance dominated ( $I = 0.6$ mA, $\epsilon = 6$ $\mu\text{m}$ ). ....	36
Figure 2.7: Schematic layout of the tomography configuration for UMER; (a) Orientation of quadrupoles; (b) Transfer matrices (indicated by arrows). The distance between A and B is 61.3cm, the distance between A and center of Q1 is $L_1 = 8.0$ cm, the quadrupole center to center distance is $L_2 = 16.0$ cm, and the distance between screen and center of Q4 is $L_3 = 5.3$ cm. ....	41

Figure 2.8: Plot shows the numerical solution of the beam envelope equation (Eq. 2.41). Step $t$ should be kept below 0.4 mm and the beam size as well focusing is assumed to be constant within this region. ....	45
Figure 3.1: Angular difference between adjacent projections versus the projection number for three different cases. ....	53
Figure 3.2: Phase-space distributions for the three different cases. Note that for all cases the total phase space rotation was $180^0$ . ....	54
Figure 3.3: Phase Space reconstruction for different phase space rotations. ....	55
Figure 3.4: X'X phase space distribution of the pencil beam with different simulated systematic errors. (a) 1% error, (b) 3% error, (c) 5% error ....	56
Figure 3.5: Recovered phase spaces from WARP (left side) and Tomography (right side) for beams with different intensity parameters: (a) $\chi=0.3$ (b) $\chi=0.72$ (c) $\chi=0.9$ ....	60
Figure 3.6: The Gaussian velocity distribution that is rotated around a circle of radius $\alpha$ ....	64
Figure 3.7: Schematic layout of the five beamlet distribution. Note that $2b$ is the diameter of the beam pipe. Distances are not to scale. ....	66
Figure 3.8: Beam distributions in configuration space (left) and beam distribution in phase space (right) from direct WARP simulation at $z = z_0$ ....	67
Figure 3.9: Phase spaces for the 7mA obtained by WARP (second column) and Tomography (third column) at $z = z_1$ using different input distributions. ....	68
Figure 3.10: Phase space from simulations of the 7 mA beam after propagating for different distances, clearly indicating the propagation of transverse density waves: tomography (top) vs. direct WARP result (bottom) (cf. ref. [47]). Phase space after passing through (a) 0; (b) 1; (c) 3; (d) 5; and (e) 7 quadrupoles upstream of Q1. The symbol $z$ indicates the total distance the beam has traveled. ....	72
Figure 4.1: Layout of UMER: (a) Schematic representation; (b) Actual Photo .....	76
Figure 4.2: Aperture wheel at the gun exit. Note that there are six different apertures, each one resulting to a beam with different intensity. ....	78

Figure 4.3: Screen assembly on UMER. Note that the mirror is at an angle $\phi = 45^0$ to allow the light to come out from the window. ....	81
Figure 4.4: Images of the same beam with the same camera but different lenses. The aperture of a lens determines the amount of light that passes through the lens to the sensor. The focal length is noted as F. The macro lens (far right) allows the most close-up images. ....	83
Figure 4.5: Screen shots of the GUI of the XCAP imaging software; (a) Basic features; (b) Image processing tools .....	85
Figure 4.6: Diagram of the UMER Tomography control system structure .....	87
Figure 4.7: Schematic representation of the principle of the pinhole scan. ....	89
Figure 4.8: Actual photo indicating the aperture and the screen. Note that solenoid was turned off for the pinhole scan. ....	89
Figure 4.9: Photos of individual beamlets for different positions of the pinhole. The top number shows the position of the pinhole relevant to the central beamlet. The bottom number shows the position of the knob. The bias voltage in the experiment was set at 30 V and typical beam radii of the beamlets on the screen are 6 mm. ....	91
Figure 4.10: Averaged phase space distribution at the beam aperture obtained from the pinhole scan. The vertical lines show the range of three UMER beams: 0.7 mA, 7 mA, and 23 mA. ....	92
Figure 4.11: (a) Phase space for the 23mA beam at the aperture plane generated by: (a) Solenoidal Tomography; (b) Pinhole Scan (blue dots). Red lines are locations where the beam centroid along y is calculated (red dots). ....	95
Figure 4.12: Tomography experimental configuration on UMER. ....	98
Figure 4.13: Phase space transformation example: (a) $x'$ vs. $x$ phase space; (b) same phase space but after the transformation $x' \rightarrow x' - x \tan \phi$ , where $\tan \phi$ was -5.6 mrad/mm. ....	99
Figure 4.14: Beam distribution in configuration space (top) and $XX'$ phase-space (bottom) 76 cm from the beam aperture: (a) Experiment; (b) WARP simulation .	

The subtracted slope (in units of mrad/mm) is 3.03. Clearly, a halo in configuration space is visible in the experiment.....	101
Figure 4.15: Beam distribution in configuration space (top) and YY' phase-space (bottom) 76 cm from the beam aperture: (a) Experiment; (b) WARP simulation. The subtracted slope (in units of mrad/mm) is 4.77. Clearly, a halo in configuration space is visible in the experiment.....	102
Figure 4.16: Beam evolution along UMER in configuration space (top) and XX' phase space (bottom). The 4xrms emittances (in $\mu\text{m}$ ) and subtracted slopes (mrad/mm) are 32.7, 3.22 (RC3); 70.0, 2.96 (RC6); 71.5, 3.36 (RC7); 50.0, 3.07 (RC9); and 42.7, 3.22 (RC13), respectively. ....	104
Figure 4.17: Beam evolution at different locations along UMER in configuration space (top) and YY' phase space (bottom). The 4xrms emittances (in $\mu\text{m}$ ) and subtracted slopes (in mrad/mm) are: 42.5, -6.70 (RC3); 52.6, -5.71 (RC6); 43.6, -5.71 (RC7); 54.3, -7.24 (RC9); and 96.8,-7.25 (RC13), respectively.....	105
Figure 4.18: Schematic layout of the UMER five beamlet mask. Note that $r_{\text{let}}$ and $b$ are the beamlet and UMER pipe radius, respectively. Distances are not drawn to scale.....	107
Figure 4.19: Merger of the 5 beamlets at IC2. Configuration space (top) and xx' phase space (bottom) from: (a) experiment; (b) WARP simulation. The subtracted slope (in units of mrad/mm) is -1.40.....	109
Figure 4.20: Five-beamlet evolution at different locations along the UMER ring in configuration space (top) and XX' phase space (bottom). The subtracted slope (in units of mrad/mm) are 3.08 (RC3), 3.00 (RC6), 3.53 (RC7), and 3.84 (RC13).....	110
Figure 4.21: Five-beamlet evolution at different locations along the UMER ring in configuration space (top) and YY' phase space (bottom). The subtracted slope (in units of mrad/mm) is -4.51 (RC3), -1.36 (RC6), -6.46 (RC7), and -5.90 (RC13).....	112
Figure 5.1: Schematic layout of the solenoidal tomography configuration. S1 and S2 are the two solenoids that we scan to get the projections. Simulation is initialized	

at $z_0$ and the phase space is reconstructed at $z_1$ . The geometry of the configuration is similar to the LSE. ....	121
Figure 5.2: Tomographically reconstructed phase space at the plane of the screen (first column) compared with simulated (middle column) for two beams with different $4\sigma_{rms}$ emittance $\epsilon_{rms}$ and current (I): (a) $\epsilon_{rms} = 6 \mu m$ and $I=1$ mA; (b) $\epsilon_{rms} = 16 \mu m$ and $I=10$ mA. Far right column corresponds to the beam distribution in configuration space at the same location.....	124
Figure 5.3: Distribution of the same beam at two different locations: (a) at the start ( $z=0$ cm); (b) at the screen ( $z=43.0$ cm).....	126
Figure 5.4: Phase space at the screen location generated by WARP directly (middle column) in comparison to tomography before rotating the photos by $\theta_r$ (first column) and after (third column).....	127
Figure 5.5: Experimental configuration of the LSE. : (a) schematic layout; (b) actual configuration; (c) Axial field on the axis of symmetry for solenoid currents 4.15A (S1 ) and 3.2 A (S2). ....	130
Figure 5.6: Configuration space (left column), $xx'$ phase space (right column) comparison between experiment (top) and simulation (bottom) for three different magnet pair settings: (a) case a; (b) case b; and (c) case c. ....	134
Figure 5.7: Configuration space (left column), $yy'$ phase space (right column) comparison between experiment (top) and simulation (bottom) for three different magnet pair settings: (a) case a; (b) case b; and (c) case c. ....	135
Figure 5.8: Beam distribution at the screen for case b when a uniform beam (no hole) is assumed initially.....	137
Figure 5.9: Cathode imaging at the screen location: (a) in experiment; (b) in simulation. To simulate the hole effect in WARP we assume that beam emerges through the gun aperture with a uniform distribution (but with a hole inside) similar to that shown in Fig. 5.3(a).....	138
Figure 5.10: Evolution of the beam envelope, X, and Y, for the three different magnet pairs as obtained from WARP simulation. The dashed lines show the central position of the solenoids. ....	140

Figure 5.11: Five beamlet distribution in the LSE; (a) Aperture, (b) Actual photo at the screen that shows an image of the aperture. Note that $2b$ is the diameter of the beam pipe in LSE.....	142
Figure 5.12: Configuration space (left column), $XX'$ phase space (right column) from the experiment for four different magnet pair settings (Table 5.5): (a) case 1; (b) case 2; (c) case 3; and (d) case 4. ....	143
Figure 6.1: Beam signal at the Bergoz. The red profile shows the current profile with perturbation on. The black curve shows the profile with the perturbation turned off. The main beam current was 25 mA. The perturbation aptitude is roughly 25% of that of the main beam. The camera gate was set at 10 ns (green dashed line). ....	151
Figure 6.2: Beam phase space distribution recovered by Tomography at the gun aperture ( $z = 0$ cm). (a) Without perturbation; (b) with perturbation turned on. The subtracted slope was -6.5 mrad/mm (no perturbation) and -9.7 mrad/mm (with perturbation). Note that both phase-spaces are at the same scale.....	153
Figure 6.3: Beam configuration space (top) and measured phase space by tomography (bottom) at the screen location: (a) Perturbation off; (b) Perturbation on. Notice that the beam with perturbation has higher emittance. Images are obtained with a 10 ns gate. The subtracted slope was -7.4 mrad/mm (perturbation off) and -6.7 mrad/mm (perturbation on).....	155
Figure 6.4: Beam signal at the Bergoz. The red profile shows the current profile with perturbation on. The black curve shows the profile with the perturbation turned off. The beam current was 25 mA. The perturbation is roughly 25% of the main current. The camera gate was set at 100 ns and was integrating over the whole beam pulse (green dashed line).....	157
Figure 6.5: Beam configuration space (top) and measured phase space by tomography (bottom). (a) Perturbation off; (b) Perturbation on. Images are time-integrated over the whole beam pulse. The subtracted slope was -7.4 mrad/mm for both cases. ....	158

Figure 6.6: Signal collected at the Bergoz coil showing the longitudinal current profile.....	160
Figure 6.7: Beam slices on the screen obtained by progressively moving the camera 3 ns gate window from the head to the tail of the beam pulse. Each photo is the result of 55 frame integrations. ....	162
Figure 6.8: Beam in configuration space and in phase space for slices a, b, c, d, e, and f. Phase spaces are generated using the initial conditions shown in Table 6.2. Note that the slope of the phase space is not subtracted. ....	164
Figure 6.9: Beam parameters measured in the experiment: (a) Beam size; (b) Emittance; (c) Slope of phase space (from Eq. 4.4). ....	166
B.1: External trigger application: (a) Scope reading; (b) Pulsers that control camera and beam on UMER.....	188

# Chapter 1 Introduction

Intense particle beams have applications in many different research areas which impact our lives. Such applications include accelerator-driven neutron sources [1], higher-luminosity high-energy colliders, free electron lasers (FEL) [2], heavy-ion inertial fusion drivers (HIF) [3], cancer therapy [4], and nuclear waste treatment [5]. Neutron sources and FELs have important applications in material research, helping us better understand the structure of matter and improving the quality of materials. Free electron lasers contribute to the probing and processing of components for electronics, microtechnology and nanotechnology. Finally, heavy-ion inertial fusion drivers promise the production of large and unlimited amounts of energy which can be harnessed to provide an affordable and environmentally attractive source of electrical power. All these applications are premised on the considerable challenge of generating, transporting, accelerating, and focusing large amounts of particles confined in a narrow region of phase space, without significant particle losses or deterioration of beam quality. A bunch charge of  $24 \mu C$  confined into a 695 ns pulse (line charge density equal to  $0.13 \mu C / m$ ) with  $138 \mu m$  transverse normalized rms emittance are typical parameters for such beams [1].

The limit of achievable beam quality is largely determined by the dynamics at the low-energy end of the machine [6], which is dominated by space charge forces [7]. Some challenging scientific issues arise from the space charge and collective behavior in such high current beams. Typically, in that regime the beam distribution is not in detailed equilibrium with the external focusing forces and the process of



relaxation to equilibrium can be dynamically complex and can result in emittance growth, halo formation, collective instabilities, and x-y energy transfer and coupling downstream. To investigate these effects and to fully characterize the beam properties, knowledge of the actual phase space distributions and emittances of the beam in certain locations is required.

In this dissertation we focus our research on developing a technique to accurately map the phase space of intense beams. In order to do so, we adapted the ideas of tomography, which is a commonly used method in the medical community. We followed a two step approach: First, using the particle-in-cell code WARP [8], we simulated the tomography process and compared the recovered phase space with the one generated directly by WARP. This allowed us to investigate the limitations of the technique. Second, we developed an experimental apparatus in order to measure the phase spaces of intense beams. Then, we used the tomography diagnostic to shed light on the consequences of the space charge forces on the transport of these beams. Particularly, we studied emittance growth, phase space mixing and halo evolution and compared our results with theory and simulation.

The outline of this chapter is as follows: In Sec. 1.1 we define the basic beam parameters that characterize an electron beam. In Sec. 1.2 we provide a motivation example and show the importance of the phase space distribution. In Sec. 1.3 we define space-charge and discuss its effect on beam transport. In Sec. 1.4 we review standard techniques for phase-space mapping that are used in the accelerator community. Next, in Sec. 1.5 we provide a short history of the tomography process. Finally, in Sec. 1.6 we discuss the dissertation overview.

## 1.1 Electron Beam Properties

The quality of an electron beam is determined by its brightness and emittance. Both quantities require knowledge of the phase space distribution. In Sec. 1.1.1 we define the beam phase space, in Sec. 1.1.2 we define the beam emittance and in Sec. 1.1.3 we define the beam brightness.

### 1.1.1 Transverse Phase Space

Ideally all particles within a beam should move along the same direction, let say along  $z$ , with the same velocity,  $v$ . However, since there is always a spread in the magnitude and direction of the beam velocity, the motion of each individual particle can be described by three spatial coordinates  $(x, y, z)$  and three velocity coordinates  $(v_x, v_y, v_z)$ . The space formed by those 6-coordinates is called *phase space*. It represents a snapshot of one possible state of the system. Although, it is impossible to show all six phase-space dimensions simultaneously we gain insight in the particle dynamics by viewing the projection of the particle motion in a single direction  $(x, v_x)$ . If there is no acceleration, for reasons that will become clearer in the next section it is often more convenient to plot  $(x, x')$  were  $x'$  is the particle angle with the axis of propagation ( $x' = dx/dz = v_x/v_z \approx v_x/v$ ). The coordinates  $(x, x')$  describe the trace of the particle along the axial direction  $x(z)$  at a given  $z$  and hence the space they define is known as *trace space*. Clearly, for drifting beams, phase space and trace space provide the same information for given values of  $v$ , so from now on when we refer

to phase space we mean plots of  $(x, x')$ . When forces are linear the phase space has the form of an ellipse and an example is illustrated in Fig. 1.1.

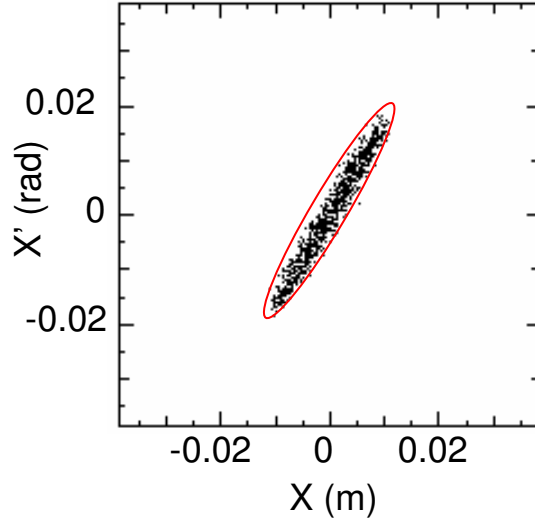


Figure 1.1: Phase-space along the transverse direction  $x$ . When forces are linear it can be approximated by a uniform ellipse (red line)

### 1.1.2 Beam Emittance

Emittance is a measure of the compactness of the phase space occupied by the particles and provides a quantitative basis to describe the quality of the beam. There are a number of different definitions of emittances. One of them is the total emittance which is defined as the effective volume (or area) of the trace space distribution. A disadvantage of this definition is that it remains always constant (if there is no acceleration). A more advantageous definition of the emittance [7] is as the product of the beam width and divergence, where the divergence arises from the spread of the velocities. Then:

$$\mathcal{E}_{x,rms} = \sqrt{\langle x^2 \rangle \langle x'^2 \rangle - \langle xx' \rangle^2}, \quad (1.1)$$

where the moments  $\langle x^2 \rangle$ ,  $\langle x'^2 \rangle$ , and  $\langle xx' \rangle$  can be found from the phase space information. This emittance is referred as rms unnormalized emittance and is conserved under linear, time-independent forces, and no acceleration. The advantage of using Eq. 1.1 is that it is not conserved in the presence of nonlinear forces and therefore is a better description of the quality of the beam. Often we select to multiply Eq. 1.1 by four since then, when the forces are linear, it becomes equal to the total emittance.

The emittance  $\epsilon_{x,rms}$  is not constant if there is an energy change, for example when we accelerate the beam. Hence, in the accelerator community often we define the rms *normalized emittance* given by

$$\epsilon_{x,rms,n} = \beta\gamma\sqrt{\langle x^2 \rangle \langle x'^2 \rangle - \langle xx' \rangle^2}, \quad (1.2)$$

where  $\beta = v/c$  and  $\gamma = (1 - \beta^2)^{-1/2}$ ;  $v$  is the beam velocity and  $c$  is the speed of light.

The normalized emittance is conserved under acceleration (assuming linear forces).

### 1.1.3 Beam Brightness

Emittance however is not enough to describe the beam quality completely. One can reduce the beam emittance by using collimating slits, however this reduces the total current. What counts for beam quality, is the number of particles for a given emittance. Hence, we introduce a quantity known as *brightness* and is defined [7] as  $B = J/d\Omega$  which is current per unit solid angle. Brightness is a measure of the density of particles in phase-space. Often, it is more convenient to use the averaged brightness which is directly related to the beam emittance by [7]

$$\bar{B} = \frac{I}{8\pi^2 \epsilon_{x,rms} \epsilon_{y,rms}}. \quad (1.3)$$

We conclude that both brightness and emittance require information of the phase space distribution and hence its knowledge is of fundamental importance to describe the beam quality.

## 1.2 The Importance of the Phase Space Distribution

In this section we present one example that illustrates the importance of the phase space distribution. Experiments and simulations show that a multibeamlet approach to generate high current intense beams offers a number of potential advantages over a single beam injector for Heavy Ion applications [3]. A similar experiment can be conducted on UMER were by using a five-beamlet mask in the electron gun we can aperture the beam to generate five distinct but interacting beamlets and observe their interaction. Figure 1.2 shows the beam evolution in configuration space (top – left column) and in phase space (bottom – left column) as predicted by the simulation [9]. Further downstream (Fig. 1.2-right column) simulations predict that the beamlets merge in real space leaving no trace of their initial structure giving the impression that the beam behaves “equivalent” to a uniform beam. Interestingly, simulation shows a different behavior in phase space where the beamlets remain distinct. Therefore, in order to be able to describe the beam behavior successfully knowledge of the phase space distribution, besides the configuration space distribution, is required.

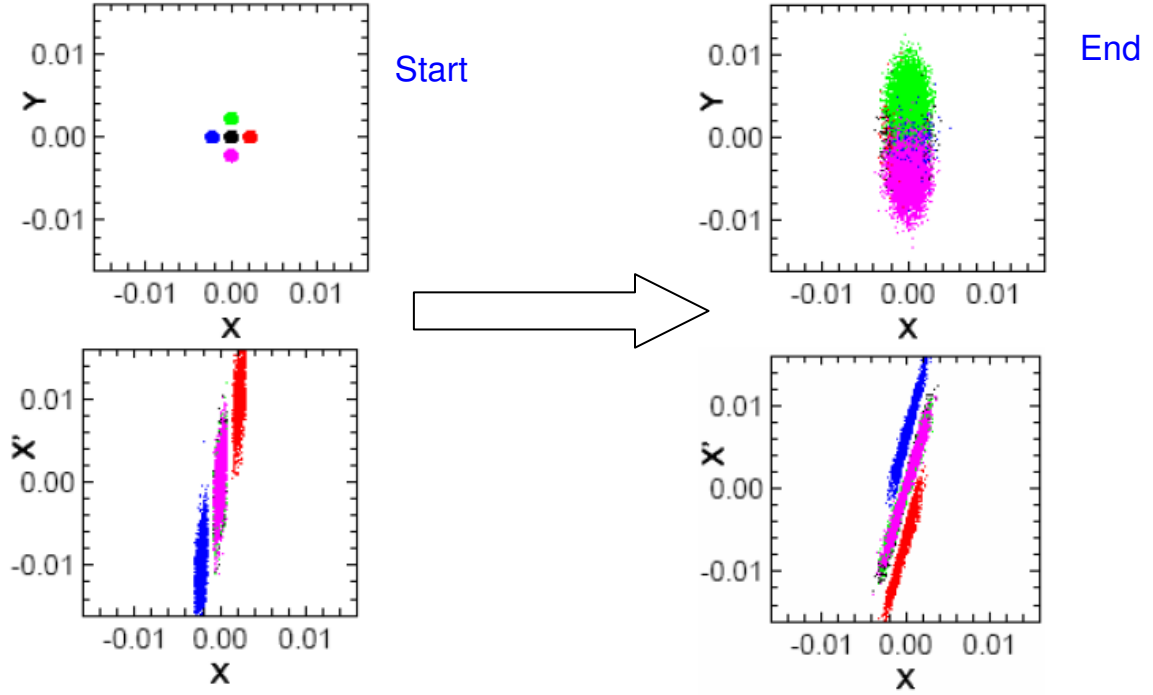


Figure 1.2: Initially we have five distinct beamlets in configuration space. Downstream the beamlets merge in configuration space but are still separated in phase space.

### 1.3 Beams with Space-Charge

The generation and transport of electron beams with high brightness and low emittance is constrained by the mutual repulsion among electrons, which is known as space-charge. Intense beams consist of many charged particles that can create magnetic and electric fields (known as self-fields). These fields can result in a net repelling force given by

$$F_{SPACE-CHARGE} = F_{MAGNETIC} + F_{ELECTRIC} , \quad (1.4)$$

where

$$F_{MAGNETIC} = -\frac{v^2}{c^2} F_{ELECTRIC} , \quad (1.5)$$

When the beam is relativistic ( $v$  comparable to  $c$ ) space-charge becomes negligible since as can easily deduced from Eq. (1.5) the self-fields forces cancel. Then, single-particle behavior dominates and each particle moves only under the influence of the external applied forces. However, near the source, where the energy is low, space-charge becomes comparable to the externally applied field. Then, particle-to-particle interactions occur via Coulomb forces and the single particle behavior gives way to collective behavior. In that case the beam can be viewed as a nonneutral plasma where the averaged focusing forces replace the fixed neutralizing background [7]. The fluid nature of the space-charge dominated beam makes it capable of carrying waves that can persist for several hundreds of focusing periods [6] and even after acceleration. Such waves if not well controlled can cause emittance growth and halo formation at the low energy end of the machine. Therefore, a good understanding of beams with space-charge is crucial and phase-space reconstruction will be an important tool to achieve this goal.

In order to study the dynamics of such intense beams in a cost efficient way we have designed and recently commissioned the University of Maryland Electron Ring (UMER) [10, 11]. Using low energy (10keV) and high current (up to 100 mA), electron beams with extreme intensities can be produced [7]. Details about the UMER ring will be discussed in Chap. 4 (see Sec. 4.1).

## 1.4 Standard Techniques for Phase Space Mapping and Emittance

### Measurement

Standard methods [12] that are commonly used in the accelerator community to map the beam phase space, are the quadrupole scan (Sec.1.4.1), pepper pot (Sec. 1.4.2), and slit wire scan (Sec. 1.4.3). Here we will briefly review these techniques and report their advantages and disadvantages.

#### 1.4.1 Quadrupole Scan

The quadrupole scan technique assumes that the phase space is an ellipse that can be described by

$$\hat{\gamma}x^2 + 2\hat{\alpha}xx' + \hat{\beta}x'^2 = \varepsilon_x, \quad (1.6)$$

where  $\hat{\beta}, \hat{\gamma}, \hat{\alpha}$  are the Twiss parameters and  $\varepsilon_x$  is the beam emittance assumed to be a constant of the motion. As the beam moves from location 1 to location 2 these parameters are related by [13]

$$\begin{pmatrix} \hat{\beta}_2 \\ \hat{\alpha}_2 \\ \hat{\gamma}_2 \end{pmatrix} = \begin{pmatrix} m_{11}^2 & -2m_{11}m_{12} & m_{12}^2 \\ -m_{11}m_{21} & m_{11}m_{22} + m_{21}m_{12} & -m_{12}m_{22} \\ m_{21}^2 & -m_{21}m_{22} & m_{22}^2 \end{pmatrix} \begin{pmatrix} \hat{\beta}_1 \\ \hat{\alpha}_1 \\ \hat{\gamma}_1 \end{pmatrix}, \quad (1.7)$$

where  $m_{ij}$  are the elements of the transport matrix between those two locations. The beam size at position 2 is related to the Twiss parameters at the initial position  $(\hat{\beta}_1, \hat{\gamma}_1, \hat{\alpha}_1)$  and transport matrix elements by,

$$x_{rms} = \sqrt{\hat{\beta}_2 \varepsilon_x} = \sqrt{m_{11}^2 \hat{\beta}_1 \varepsilon_x - 2m_{11}m_{12} \hat{\alpha}_1 \varepsilon_x + m_{12}^2 \varepsilon_x \hat{\gamma}_1}. \quad (1.8)$$



Hence, in the quadrupole scan technique, the Twiss parameters can be obtained by placing a magnet between positions 1 and 2 and inserting a screen at location 2. Then by measuring the beam size at that point as a function of the magnet focusing strengths and curve-fitting the data we can obtain  $\hat{\beta}_1, \hat{\gamma}_1, \hat{\alpha}_1$ , and the emittance. An example of such curve-fitting [14] is shown in Fig. 1.3. The technique has two important limitations: First, in the analysis we make the usual assumption that the transverse phase space distribution fills an ellipse; and second, the method becomes questionable when the beam has space charge [15].

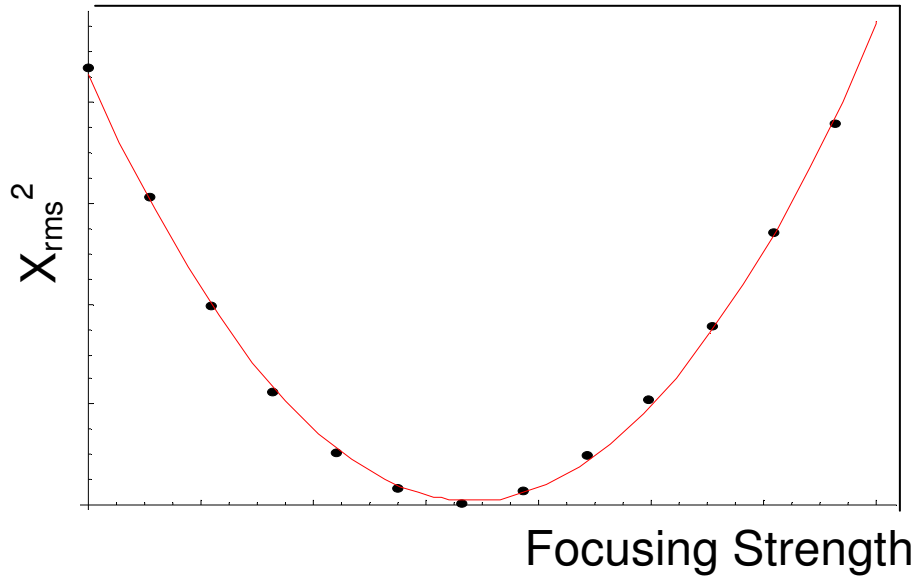


Figure 1.3: Example of the quadrupole scan. The beam size  $X_{rms}^2$  is plotted versus the magnet focusing strength and a fit line (shown in red) is plotted through the actual data (black dots). From the fit line and Eq. 1.8 we can get the beam emittance.

### 1.4.2 Pepper-pot

Pepper-pots measure the phase space distribution by using apertures to sample specific regions in transverse space. The beam is intercepted a pepper-pot plate, which is normal to the beam and contains a regular array of identical holes over its entire surface. The position of the beam passing through its hole is known as *beamlet*. A downstream screen measures the location and intensity of each beamlet. The holes are small enough so that the beams passing through become emittance dominated (no space-charge). In that case the beam drifts along a straight line between the pepper-pot and screen. Knowing the position of the beamlets at both mask,  $x_{sj}$ , and screen,  $x_j$  and the distance between them,  $L$ , we can find the angle  $x'$  of each of each beamlet by using the formula:  $x' = x_j - x_{sj} / L$ .

A schematic layout of the pepper pot concept is demonstrated in Fig. 1.4.

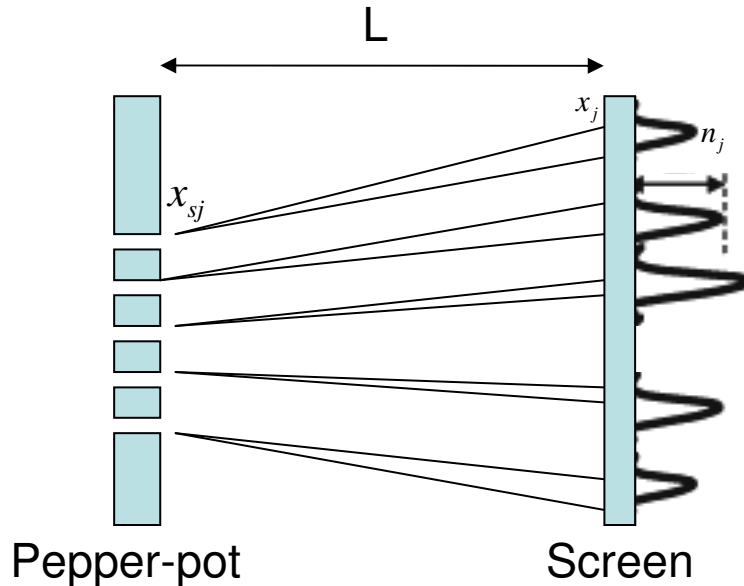


Figure 1.4: Layout of the pepper-pot concept

Pepper-pots are commonly used in the accelerator community. However, in order to get a good resolution of the reconstructed phase space, a sufficient number of beamlets should be produced. Hence, when the beam size is small (of the order of mm), very small and closely spaced holes are needed. In this regime, construction of such mask would pose serious practical difficulties. Additionally, if the holes are very close of each other, the images of the beamlets may overlap increasing so the error in the measurement. Finally, being an intercepting diagnostic, the hole reduces the beam intensity and hence it make the detection of faint features like beam halos more difficult.

### **1.4.3 Slit-Scanner**

Finally, in-slit based emittance measurements the beam is collimated by set of (vertical and horizontal) slits scanned across the beam, and then the collimated beamlets drift a given length and finally are analyzed by a collector upstream. The layout of a slit wire is shown in Fig. 1.5. The process is as follows: A detector with an analyzing slit moves over the cross section of a beam to sample different values of  $x$ . A wire beam collector moves within the detector to sample different values of  $x'$ . A serious problem is the limited signal to noise ratio of the beam signal after passing the slit scanners. Furthermore, due its geometry it's averaging over  $y$  and hence assumes that motion in  $x$  and  $y$  is decoupled.

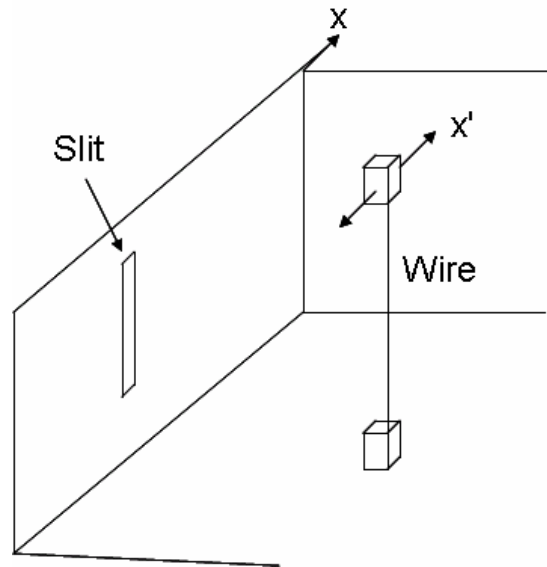


Figure 1.5: Scanned wire diagnostic layout, adapted from ref. 16.

## 1.5 History of Phase Space Tomography

Computerized tomography is well known in the medical community and was originally developed to process x-ray images. A Norwegian physicist Abel (1826) first published a concept of tomography for an object with axisymmetric geometry. In particular, Abel presented the method of obtaining the profile of a circularly symmetric 2-D object from its projection [17]. Nearly one hundred years later, an Austrian mathematician Radon (1917) extended the idea for arbitrary-shaped objects by developing a theorem which stated that an object in  $n$ -dimensional space can be recovered from a sufficient number of projections onto  $(n-1)$ -dimensional space [18].

In beam physics it is possible to map the phase space by using information taken from the spatial density distribution at the same point. A simple scaling equation relates the spatial beam projections to the Radon transform of the transverse phase space. This was stated already 30 years ago, when Sander et al. [19] used

tomography to reconstruct the phase space distribution from transverse spatial profiles of the beam. In their technique they imaged the beam at different positions along the beam line and then reconstructed the phase space distribution by using tomographic computer programs. The physical availability of profile monitors along the beam line limited the number of spatial projections of the beam to three; therefore the resolution of the reconstructed phase space was poor. In a similar fashion, Fraser [20] reconstructed the phase space by tomography by using either two or three projections. Again, because of the small numbers of views the phase space plots lacked structure.

Phase space tomography was implemented successfully and with greater accuracy by McKee et al. [21]. In that study, McKee, in order to recover the density information in phase space combined the ideas of tomography with quadrupole scanning. To account for the beam stretching that occurred while the magnet was scanned, McKee was scaling the profiles by using a scaling parameter. McKee showed that both scaling parameter and angle of projection can be calculated from the beam transport matrix. Since then, the same approach was followed by several authors [22, 23]. Yakimenko et al. [24] by using nine quadrupoles was able to obtain projections on the screen that corresponded to beams with different phase advances (projection angles) but all had the same size. So, there was no need to account for the stretching problem, however, the large transport line required (because the many quadrupoles) can increase the error of the measurement.

All these tomography diagnostics were implemented for relativistic beams where space-charge was negligible. Therefore, the applied tomography algorithm

ignored space-charge effects. However, when the beam is non-relativistic, the space charge force has to be accounted in the analysis. One method that has been proposed [25] treats space charge as a linear correction that is estimated from the beam envelopes. The first experimental results have been reported for a beam with space-charge using this approach. Still, however, many questions remain and we will address them in the next section.

## **1.6 Dissertation Overview**

Even though tomography has been used over the last few years as a diagnostic to map the beam phase space, some questions remain about the limitations of the method. Can the technique be used for beams with intense space charge? Could a simple linear space charge approximation accurately reproduce the beam phase space? In addition, will tomography map the phase space for beams with different and more complex distributions?

Solenoids are commonly used as focusing elements at low energies, especially in photoinjectors [26], and immersed guns for flat-beam production [27]. Many ion injectors and low-energy machines use solenoids to match proton beams into a radio-frequency quadrupole as well as to transport high space charge beams [28]. It is therefore advantageous to develop a technique that uses solenoids for phase space mapping. Therefore, how can solenoids be used for tomography?

Additionally, the evolution of the phase space of merging beamlets has been shown to be important in simulations [29] and experiments [30] for Heavy ion fusion applications where the concept of merging multiple beams is used to generate high-

current beams. Furthermore, given the similarities of dynamics between the coulomb and gravitational forces (both interact though long range inverse square law forces) it has been suggested [31] that a good understanding of the phase space mixing of nonuniform charged particle beams can be used to examine many different physical processes in astrophysics such as colliding and merging galaxies [32, 33]. Therefore, it is important to examine the detailed evolution and degree of phase-mixing of such nonlinear particle beams in both configuration and phase space.

Finally, for beam applications such as X-ray FELS and Spallation Neutron Sources, knowledge of the time-sliced parameters of beam current, energy spread and transverse emittance is an important requirement to understand their evolution. For instance characterization of the transverse phase space of the beam at the injector exit is necessary, as it allows the tuning and verification of the photoinjector properties. Such as an example is emittance compensation [34], a process which is used to correct for the correlation between the phase space angle and the longitudinal position of slices. Even though a number of studies conducted so far perform time-resolved phase space maps and slice emittance measurements [35-37], time-resolved measurements for space-charge dominated beams was never been examined. For example, how does the transverse slice emittance evolve within a beam pulse for a beam with space-charge?

This dissertation will address the topics mentioned above. The outline of our work is as follows: In Chap. 2 we review the basic beam theory, discuss the single particle motion and define space-charge. Next, we describe the tomography algorithm

and relate it to beam physics. Then, we describe our approach to extend it to beams with intense space-charge.

In Chap. 3 we describe the process we use to verify our diagnostic by simulating a tomography experiment with the particle-in-cell code WARP. We examine the effect of various errors in the data collection process on the reconstructed phase space (such as the number of projections, rotation angle, and uncertainties in measurements). Furthermore, we simulate the process by using different beam distributions and beams with different content of space-charge and report our results.

In Chap. 4 we use tomography to study the influence of space-charge forces on the beam transport. We address issues such as emittance growth, phase mixing and halo evolution for intense space-charge beams. First we study the evolution of an initially “uniform” beam with space charge. Then, we examine phase-mixing for a beam with an initially non-uniform distribution. For this experiment, we create five distinct but interacting beamlets, observe their interaction and compare our results with simulation and theory.

In Chap. 5 we discuss our approach to extend tomography to use solenoidal magnets. First we verify the technique by simulating the process by the same way we did in Chap. 3. Then, we apply the diagnostic in the experiment and compare our results with simulation. Furthermore, we discuss the relation between emittance growth and beam size for a beam passing through a solenoid. Finally, we provide a generalized algorithm to use tomography to cases where the beams are not axisymmetric.



In Chap. 6 we report time resolved measurements of phase space tomography for intense particle beams. Specifically, we study the correlation between transverse and longitudinal dynamics in phase space by applying different longitudinal perturbations. We show that a longitudinal perturbation can affect the transverse phase space.

Finally, in Chap. 7 we summarize the results of this dissertation and provide a list of interesting topics for future research.

## Chapter 2 Tomography Theory

Measurement of the transverse phase space distribution is an important tool to understand transverse particle dynamics in accelerators. Standard methods that are commonly used in the accelerator community to map the beam phase space (such as the quadrupole scan, pepper pot, and slit wire scan) were briefly reviewed in Chap. 1 and as it was evident they had some limitations. Therefore, it is advantageous to develop new methods to accurately reconstruct the beam phase space.

This chapter describes how to measure the transverse phase space distribution by combining the ideas of quadrupole-scanning with Tomographic image techniques. Prior work [21, 24], demonstrated that it is possible to map the beam phase space by measuring spatial projections of the beam. However, these previous methods were applied to relativistic beams with no space-charge. In this chapter we discuss the difficulties arising in cases where space-charge is present and demonstrate an algorithm for Tomographic phase space mapping for intense space-charge dominated beams.

The outline of this chapter is as follows: In Sec. 2.1 we briefly review the basic beam theory, discuss the motion of a single beam particle and define space-charge. In Sec. 2.2 we review the tomography algorithm and its relations to the phase space measurement for beams without space-charge. In Sec. 2.3 we show the extension algorithm to use tomography to beams with space-charge. In Sec. 2.4 we discuss the modifications we do to apply the diagnostic for our experiments. Finally, we review the image analysis software for tomography and show a step by step example where we describe how to use it to reconstruct the beam phase-space.

## 2.1 Basic Theory

A beam consists of a group of particles that have small energy spread compared to their average translational energy, and where the particle transverse motion is at very small angles with respect to the beam translational orbit. We briefly review the motion of a single beam particle and discuss the implications when space-charge is present.

### 2.1.1 Beam Transfer Matrices

In this section we describe the transverse particle motion at the exit of a beam transport location, such as a lens or a simple drift segment, relative to the orbit at the entrance. As discussed in Chap.1 the position of the particle can be represented as a point in a six dimensional space. Assume that the beam propagates in the z-direction with a longitudinal momentum and size much higher than the momentum and size in the transverse directions. Then, the transverse particle orbit at some axial position can be represented by the four-dimensional vector  $(x, x', y, y')$ , where  $x$  (or  $y$ ) is the transverse displacement from the horizontal plane  $x$  (or  $y$ ). The quantity  $x'$  (or  $y'$ ) is the angle the particle makes in that plane with respect to the main axis  $z$ . In many practical cases the forces in the  $x$  and  $y$  directions are independent and we can calculate the particle motion in  $x$  and  $y$  separately using the two-dimensional vectors  $(x, x')$  and  $(y, y')$ , respectively. We shall concentrate our analysis of orbits that are separable in  $x$  and  $y$ .

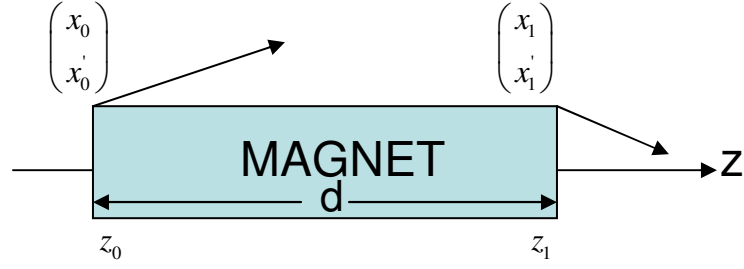


Figure 2.1: Layout showing a particle that enters a lens at  $z_0$  and exits the lens at  $z_1$ .

Consider the motion of a particle along the transverse  $x$ -direction in a lens of length  $d$  as shown in Fig. 2.1. If the exit vector is  $(x_1, x_1')$  and the entrance vector is  $(x_0, x_0')$  then the particle equation of motion is:

$$\frac{d^2 x}{dz^2} = -\kappa_0 x, \quad (2.1)$$

where  $F = \kappa_0 x$  is the focusing force of the lens assumed to be linear. Equation 2.1 has the following solutions:

$$x_1 = x_0 \cos(\sqrt{\kappa_0} d) + \frac{x_0'}{\sqrt{\kappa_0}} \sin(\sqrt{\kappa_0} d), \quad (2.2)$$

$$x_1' = -x_0 \sqrt{\kappa_0} \sin(\sqrt{\kappa_0} d) + x_0' \cos(\sqrt{\kappa_0} d). \quad (2.3)$$

In matrix notation, the above equations can be written as:

$$\begin{pmatrix} x_1 \\ x_1' \end{pmatrix} = \begin{pmatrix} \cos(\sqrt{\kappa_0} d) & \frac{1}{\sqrt{\kappa_0}} \sin(\sqrt{\kappa_0} d) \\ -\sqrt{\kappa_0} \sin(\sqrt{\kappa_0} d) & \cos(\sqrt{\kappa_0} d) \end{pmatrix} \begin{pmatrix} x_0 \\ x_0' \end{pmatrix} = T \begin{pmatrix} x_0 \\ x_0' \end{pmatrix}. \quad (2.4)$$

The matrix  $T$  is known as the *transport matrix* of the lens and  $\kappa_0$  is often called the *focusing function* and is related to the strength of the lens. For quadrupole magnets the focusing function is [7]

$$\kappa_0 = \frac{qg}{m\gamma\beta c}, \quad (2.5)$$

where  $g$  is the quadrupole field gradient;  $q$ ,  $m$ , and  $c$  are the particle charge, mass and speed of light, respectively. In practice, it is common to model the quadrupole by using a “hard-edge” approximation where the magnetic field is constant inside the quadrupole over a certain length, known as effective length  $L_{eff}$ , and drops to zero outside. From Eq. 2.2 we see that particles oscillate harmonically when traveling through the lens. Those oscillations are known as *betatron oscillations* with *betatron wavelength*,  $\lambda_{\beta 0}$ , which for our case is  $\lambda_{\beta 0} = 2\pi / \sqrt{\kappa_0}$ .

As it easy follows from Eq. 2.4 when the beam is passing through a drift section ( $\kappa_0$  is zero), the transport matrix becomes

$$T = \begin{pmatrix} 1 & d \\ 0 & 1 \end{pmatrix}. \quad (2.6)$$

Next, we are interested to study the influence of space-charge on the particle motion.

### 2.1.2 Space-charge Effects on Particle Motion

In the previous chapter we assumed that individual particles are moving only under the influence of the external focusing forces. However, as the current is increased the superimposed electric field generated by the particles themselves becomes non-negligible generating phenomena known as space-charge (see Sec. 1.3). Space-charge results to a repelling force,  $F_{SC}$ , and therefore Eq. 2.1 becomes

$$\frac{d^2x}{dz^2} = -\kappa_0 x + F_{SC}. \quad (2.7)$$

Space-charge force has been shown to be linear for uniform distributions [7]. Then, Eq. 2.7 can be written as

$$\frac{d^2x}{dz^2} = -\kappa_0 x + \frac{Kx}{R(z)^2} = \kappa x, \quad (2.8)$$

where  $R(z)$  is the radius assumed that the beam is round;  $K$  is the generalized beam perveance a unitless quantity that depends on the beam current and is given by [7]

$$K = \frac{qI}{2\pi\epsilon_0 m v^3}, \quad (2.9)$$

where  $I$  is the current;  $v$  is the velocity of the beam; and  $\epsilon_0$  is the permittivity. As we can see from Eq. (2.8) space charge decreases the focusing efficiency of the lens by a factor of  $K/R(z)^2$ . This leads to an increase of the amplitude of the particle oscillations and the particles are said to perform *depressed betatron oscillations* with a wavelength  $\lambda_\beta = 2\pi/\sqrt{\kappa}$ .

It is often more convenient to describe the average beam evolution by using rms quantities. Then, the beam transport for an axisymmetric channel is governed by the 2-D rms envelope equations [38]

$$\frac{d^2 \bar{R}(z)}{dz^2} + \kappa_0 \bar{R}(z) - \frac{K}{\bar{R}(z)} - \frac{\epsilon^2}{\bar{R}(z)^3} = 0, \quad (2.10)$$

where  $\bar{R}$  is  $2 \times rms$  beam radius and  $\epsilon$  is the  $4 \times rms$  emittance. One of the advantages of using the beam envelope equations is that even though they are proven for a beam with a uniform distribution ( $\bar{R} = R$ ) they can describe the evolution of nonuniform

beams as long as they energy, current, rms size and divergence are equivalent to that of a uniform beam [7, 38].

From Eq. (2.10) we can see that the average behavior of the beam is determined by three forces: the focusing force, the space charge force and the thermal pressure force from the emittance. When these forces are balanced

$$\kappa_0 \bar{R}(z) = \frac{K}{R(z)} + \frac{\epsilon^2}{R(z)}, \quad (2.11)$$

and the beam is known as *matched*. Depending on which of the two terms in the right side of Eq. (2.11) dominate, the beam is space-charge dominated ( $\frac{K}{R} > \frac{\epsilon^2}{R}$ ) or

emittance-dominated ( $\frac{K}{R} < \frac{\epsilon^2}{R}$ ).

Another way to quantify space-charge is by introducing the dimensionless intensity parameter  $\chi$  which can be expressed as the ratio of space-charge force to external focusing force and is given by [39]

$$\chi = \frac{K}{\kappa_0 R}. \quad (2.12)$$

If,  $0 < \chi \leq 0.5$  the beam is emittance dominated, if  $0.5 < \chi < 1$  it is space charge dominated. The betatron wavelength and depressed wavelength can be expressed in terms of the intensity parameter  $\chi$  by

$$\frac{\lambda_\beta}{\lambda_{\beta 0}} = (1 - \chi)^{-1/2}. \quad (2.13)$$

Clearly, as  $\chi$  approaches unity the betatron wavelength becomes extremely large.

## **2.2 Tomography for Beams without Space-Charge**

We now review the tomography algorithm (Sec. 2.2.1) and show its extension to reconstruct the beam phase space distribution (Sec. 2.2.2).

### **2.2.1 Filtered-Backprojection Algorithm**

Several algorithms [40] are available to compute high quality reconstructions from projection data, e. g., Algebraic Reconstruction Technique, Maximum Entropy Tomography, filtered-backprojection algorithm (FBA), etc. The FBA algorithm is the most common method to reconstruct a two-dimensional image and is generally believed that it provides a reconstructed image of high quality with normally available computer capacity and computational times [40]. This is the algorithm that we use and hence we describe in detail along the lines below.



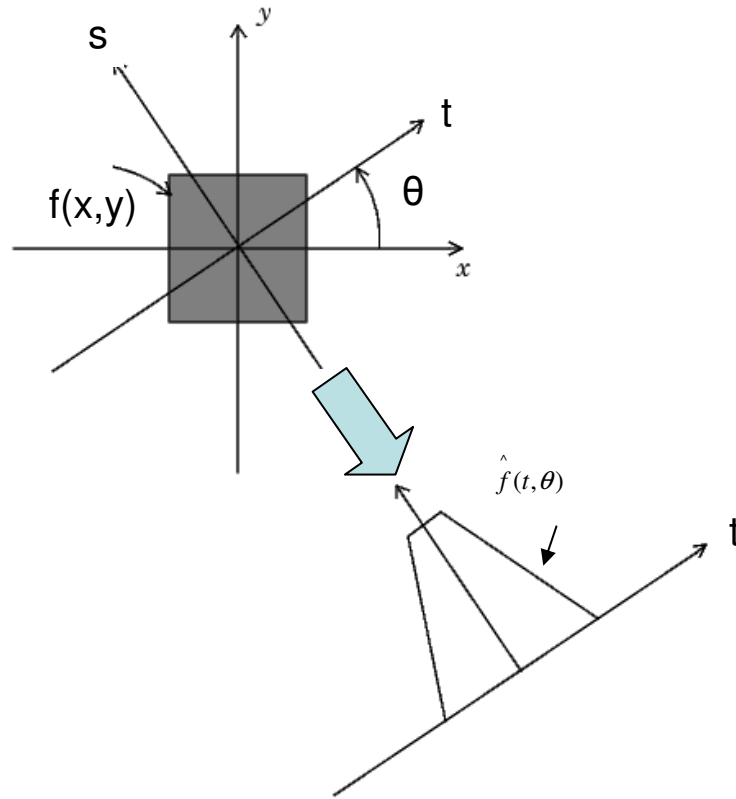


Figure 2.2: Illustration of the Radon Transform

Suppose that  $f(x, y)$  corresponds to a two dimensional distribution. Then the integral

$$\hat{f}(t, \theta) = \int_{-\infty}^{\infty} \int_{-\infty}^{\infty} dx dy f(x, y) \delta(x \cos \theta + y \sin \theta - t) \quad (2.14)$$

defines the transverse projection of the distribution  $f(x, y)$  along the axis  $t = x \cos \theta + y \sin \theta$ , placed at an angle  $\theta$  relative to the x-axis. Such a projection is known as the *Radon transform* of the function  $f(x, y)$  and is shown in Fig. 2.2. If  $F(u, v)$  is the two-dimensional Fourier transform of the function  $f(x, y)$ , then its inverse Fourier transform is given by

$$f(x, y) = \int_{-\infty}^{\infty} \int_{-\infty}^{\infty} F(u, v) e^{j2\pi(ux+vy)} dudv. \quad (2.15)$$

By exchanging the rectangular coordinate system in the frequency domain (u,v) for a polar coordinate system (w,  $\theta$ ) Eq. (2.15) becomes

$$f(x, y) = \int_0^{\pi} \int_{-\infty}^{\infty} F(w, \theta) |w| e^{j2\pi wt} dw d\theta. \quad (2.16)$$

Likewise, the Fourier transform of the Radon transform is

$$S(w, \theta) = \int_{-\infty}^{\infty} \hat{f}(t, \theta) e^{-j2\pi wt} dt. \quad (2.17)$$

Using the Fourier Slice Theorem [40] we can write  $F(w, \theta) = S(w, \theta)$  and therefore

$$f(x, y) = \int_0^{\pi} \int_{-\infty}^{\infty} S(w, \theta) |w| e^{j2\pi wt} dw d\theta, \quad (2.18)$$

or simpler

$$f(x, y) = \int_0^{\pi} Q(t, \theta) d\theta, \quad (2.19)$$

where Q is given by

$$Q(t, \theta) = \int_{-\infty}^{\infty} S(w, \theta) |w| e^{j2\pi wt} dw, \quad (2.20)$$

and is called “filtered projection” [40]. Therefore, if a number of projections between 0 and  $\pi$  are known, the distribution can be reconstructed by backprojecting the filtered version of the projections according to Eq. (2.19).

### 2.2.2 Extension of Tomography to Beam Physics

Now, we will show that beam images in configuration space are related by a simple scaling equation to projections of the phase space distribution. The idea is the following: As discussed in Sec 2.1.1 the transverse beam evolution can be described by a 4-dimensional phase space distribution  $\mu(x, x', y, y')$ . Placing a screen along the beam path gives a two dimensional projection of this distribution, known as the *configuration space*, and is given by

$$g(x, y) = \iint \mu(x, x', y, y') dx' dy' . \quad (2.21)$$

Integration over y leads to the beam profiles along x

$$c(x) = \int g(x, y) dy = \iiint \mu(x, x', y, y') dx' dy' dy . \quad (2.22)$$

We are interested to reconstruct the 2-dimensional phase space distribution  $\mu(x, x')_z$  at a particular  $z$ , which is given by

$$\mu(x, x')_z = \iint \mu(x, x', y, y') dy dy' . \quad (2.23)$$

The corresponding spatial projection of this distribution is

$$h(x) = \int \mu(x, x')_z dx' = \iiint \mu(x, x', y, y') dy dy' dx' . \quad (2.24)$$

From Eq. (2.22) and Eq. (2.24) we can see that

$$c(x) = h(x) \quad (2.25)$$

Therefore, the beam profile obtained from the integration of the distribution along y is equivalent to the spatial projection of the phase space distribution.

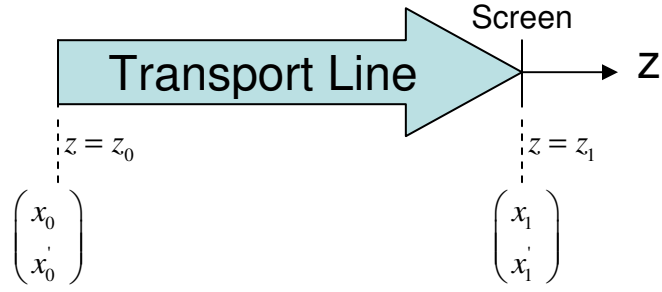


Figure 2.3: Schematic layout of the beam transport line. The starting location is at  $z_0$  and ending location is at  $z_1$ .

Suppose that our beam transport line is that shown in Fig. 2.3. Then, if  $g(x_1, y_1)_{z_1}$  is the beam distribution at a location  $z_1$  downstream, according to Eq. 2.25 we can write

$$c(x_1) = \int g(x_1, y_1)_{z_1} dy_1 = h(x_1) = \int \mu(x_1, x_1')_{z_1} dx_1', \quad (2.26)$$

where  $\mu(x_1, x_1')_{z_1}$  is the 2-D phase distribution at  $z_1$ . Using the Dirac delta function, it can be written in the equivalent form

$$c(x) = \int \int \mu(x_1, x_1')_{z_1} \delta(x_1 - x) dx_1 dx_1', \quad (2.27)$$

where  $x$  is a point within the beam distribution at  $z_1$ . According to Liouville's theorem [7] the particle density remains constant, therefore

$$\mu(x_0, x_0')_{z_0} = \mu(x_1, x_1')_{z_1}, \quad (2.28)$$

where  $\mu(x_0, x_0')_{z_0}$  is the 2D phase space distribution at the starting location  $z_0$ . If we assume that we have a linear system, the particle motion between  $z_0$  and  $z_1$  obeys

$$\begin{pmatrix} x_1 \\ x_1' \end{pmatrix} = M_1 \begin{pmatrix} x_0 \\ x_0' \end{pmatrix}, \quad (2.29)$$

where  $M_1 = \begin{pmatrix} M_{11} & M_{12} \\ M_{21} & M_{22} \end{pmatrix}$  is the transport matrix. Typically the transport line can consist of drift sections and several lenses. By combining Eq. (2.28) with Eq. (2.29) we can write:

$$c(x) = \iint \mu(x_0, x'_0)_{z_0} \delta(M_{11}x_0 + M_{12}x'_0 - x) dx_0 dx'_0. \quad (2.30)$$

In order to relate Eq. (2.30) to the Radon transform we define the scaling factor,  $s$ , by [21]

$$s = \sqrt{M_{11}^2 + M_{12}^2}, \quad (2.31)$$

and the phase space rotation angle  $\theta$ , by [21]

$$\tan \theta = \frac{M_{12}}{M_{11}}. \quad (2.32)$$

Now, using Eq. (2.31) and Eq. (2.32), Eq. (2.30) becomes

$$c(x) = \frac{1}{s} \iint \mu(x_0, x'_0)_{z_0} \delta(x_0 \cos \theta + x'_0 \sin \theta - \rho) dx_0 dx'_0, \quad (2.33)$$

where  $\rho = x/s$ .

Comparing Eq. (2.14) with Eq. (2.33) we can write

$$\hat{\mu}(\rho, \theta)_{z_0} = \hat{\mu}(x/s, \theta)_{z_0} = sc(x/s). \quad (2.34)$$

From Eq. (2.34) we can deduce that a simple scaling equation relates the spatial beam projections to the Radon transform,  $\hat{\mu}(x/s, \theta)_{z_0}$  of the transverse phase space. This is a very useful result since the beam spatial distribution can be easily obtained in experiments, e.g., using a phosphor screen. Both, scaling factor and

angles of the projection can be easily calculated from the beamline overall transport matrix and are functions of the magnet focusing.

The complete beam tomography procedure can therefore be as follows:

For a given magnet setting:

1. Calculate the transport matrix  $M_1$  between  $z_0$  and  $z_1$
2. At point  $z = z_1$ , get the beam distribution  $g(x, y)$  and calculate the profile by using Eq. 2.26.
3. Calculate the rotation angle and scaling factor by using Eq. 2.31 and Eq. 2.32
4. Relate the beam profile to the Radon transform by scaling the profile vertically by  $s$  and horizontally by  $x/s$  according to Eq. 2.34
5. Filter the projections by calculating  $Q$  from Eq. 2.20
6. Change the magnet setting and repeat steps 1-5

At the end of the scan integrate the filtered projections,  $Q$ , over the rotation angle by using Eq. 2.19.

### **2.2.3 Example: Tomography with Quadrupoles**

In the previous section we studied theoretically how to relate the beam profiles to the Radon transform of the phase space. Here we are interested to demonstrate an example of this process. Suppose that the transport line of Fig. 2.3 consist of a quadruple lens of effective length  $L_1$  followed by a drift section of length  $L_2$ . Such configuration is illustrated in Fig. 2.4.

Our goal is to measure the phase space at  $z_0$  by collecting beam profiles at  $z_1$ . We will follow step by step the process described in section 2.2.2. First, we have to calculate the transfer matrix  $M_1$ . For our beamline

$$M_1 = M_D M_Q, \quad (2.35)$$

where  $M_D$  is the transport matrix of the drift section given by Eq. (2.6) and  $M_Q$  is the transport matrix of the quadrupole given by Eq. (2.4). By multiplying those matrices we get

$$M_1 = \begin{pmatrix} -L_2 \sqrt{\kappa_0} \sin(\sqrt{\kappa_0} L_1) + \cos(\sqrt{\kappa_0} L_1) & \frac{1}{\sqrt{\kappa_0}} \sin(\sqrt{\kappa_0} L_1) + L_2 \cos(\sqrt{\kappa_0} L_1) \\ -\sqrt{\kappa_0} \sin(\sqrt{\kappa_0} L_1) & \cos(\sqrt{\kappa_0} L_1) \end{pmatrix}. \quad (2.36)$$

Next, we can use this information to get the rotation angle and scaling factors. Hence, by using Eq. (2.32) the rotation angle is

$$\theta = \tan^{-1} \left( \frac{\frac{1}{\sqrt{\kappa_0}} \sin(\sqrt{\kappa_0} L_1) + L_2 \cos(\sqrt{\kappa_0} L_1)}{-L_2 \sqrt{\kappa_0} \sin(\sqrt{\kappa_0} L_1) + \cos(\sqrt{\kappa_0} L_1)} \right), \quad (2.37)$$

and from Eq. (2.31) the scaling factor is

$$s = \sqrt{\left[ \frac{1}{\sqrt{\kappa_0}} \sin(\sqrt{\kappa_0} L_1) + L_2 \cos(\sqrt{\kappa_0} L_1) \right]^2 + \left[ -L_2 \sqrt{\kappa_0} \sin(\sqrt{\kappa_0} L_1) + \cos(\sqrt{\kappa_0} L_1) \right]^2}. \quad (2.38)$$

In the analysis we assumed focusing quadrupoles ( $\kappa > 0$ ); however, the same set of equations can be used for defocusing quadrupoles by just replacing  $\kappa_0$  with  $-\kappa_0$ . In

typical experiments, quadrupole and drift lengths are fixed, therefore the projection angle and scaling factor are only functions of the magnet strength  $\kappa_0$ .

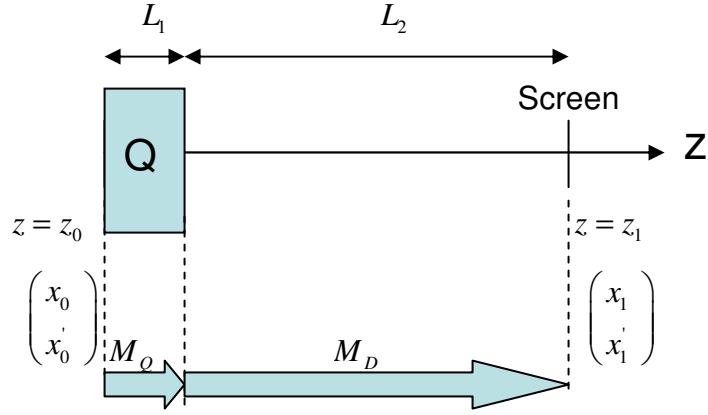


Figure 2.4: Schematic layout of the beamline between  $z_0$  and  $z_1$ . The arrows at the bottom represent the transport matrices.

Filtered projections,  $Q$ , at  $z_1$  for different focusing strengths can be used to derive the phase-space distribution. In Fig. 2.5 we show the procedure to obtain those projections for three different magnet settings. First, we have to obtain the beam distribution  $g(x, y)$  at  $z_1$  for each case. We can do so by placing an imaging diagnostic there. Figure 2.5 (first row) shows beam distributions  $g(x, y)$  at  $z_1$  for three different magnet settings (indicated at the top of the photo). Figure 2.5 (second row) illustrates the corresponding transport matrix,  $M_1$ , (from Eq. 2.36) were we assumed  $L_1 = 3.72$  cm,  $L_2 = 12.28$  cm and  $3.61 \times 10^{-4}$  G/Acm for the quadrupole length, drift length and field gradient, respectively. From the beam distributions and Eq. 2.26 we calculate the beam profiles  $c(x)$  (Fig. 2.5, third row). Now we have to scale those profiles and relate them to the Radon transform of the phase space (see



Eq. 2.34). Our results are demonstrated in the fourth row of Fig. 2.5 as well as the value of the corresponding rotation angle and scaling factor (calculated from Eq. 2.37 and Eq. 2.38). Finally, we have to filter those profiles by using Eq. 2.20. Such profiles are illustrated at the last column of Fig. 2.5. The final step is to integrate over the whole range of angles (Eq. 2.19). As we will show in the next chapter, usually a large number of projections within the whole (0, 180) degree range is necessary to do an accurate reconstruction. In our example we had to collect 87 projections by varying the strength of the magnet from  $\kappa_0 = 371.8 \text{ m}^{-2}$  to  $\kappa_0 = -230.1 \text{ m}^{-2}$  and our reconstructed phase space is shown in Fig. 2.6.

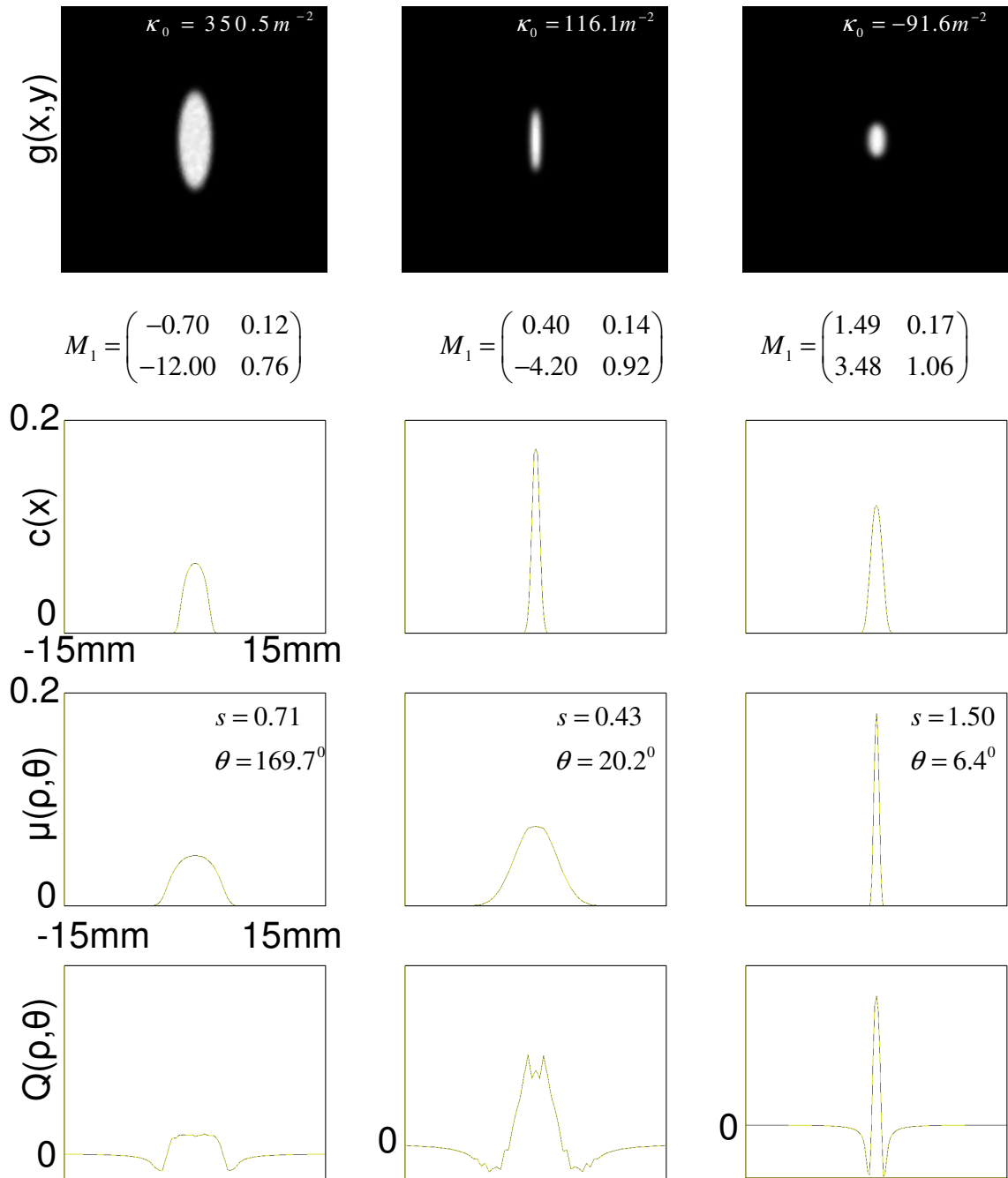


Figure 2.5: Example demonstrating the procedure to obtain projections of the phase-space distribution.

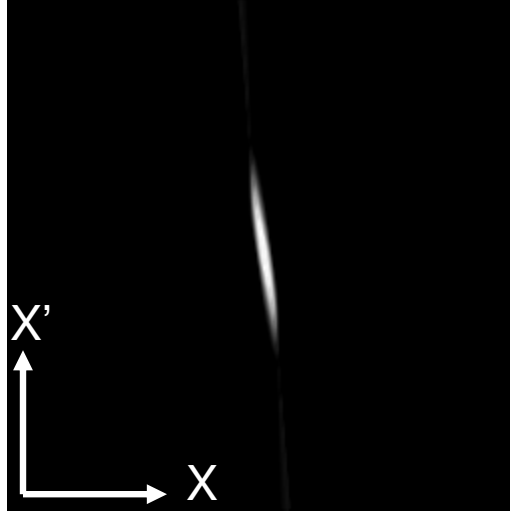


Figure 2.6: Reconstructed phase space at  $z_0$  by processing 87 projections after rotating the phase space by a full  $180^0$  angle. The intensity parameter was 0.3 and the beam was emittance dominated ( $I = 0.6$  mA,  $\varepsilon = 6$   $\mu$ m).

### 2.3 Tomography Extension to Beams with Space-Charge

In the previous section we showed that both scaling factor and projection angle can be derived from the beam transport matrix. The analysis was assuming no-space charge. As it is evident from Eq. 2.7 calculation of the transport matrix is complicated in the presence of space charge. The problem is that the space-charge force, in general, depends on the particle distribution and therefore can have very complex functions making the solution of the differential equation very difficult.

In order to simplify the analysis some assumptions need to be made about the density distribution and the resulting space charge forces. One proposed method [25] to calculate the transport matrix is to assume a uniform beam distribution. Then, the

space charge forces become linear and according to Eq. 2.8 the net focusing strengths (generalized to a non-symmetric beam) become [7]:

$$\kappa_x = \kappa_{x0} - \frac{2K}{X(X+Y)}, \quad (2.39)$$

$$\kappa_y = \kappa_{y0} - \frac{2K}{Y(X+Y)}, \quad (2.40)$$

where  $\kappa_{x0}, \kappa_{y0}$  are quadrupole focusing strengths defined by Eq. 2.5, and  $X, Y$  are the  $2 \times rms$  beam sizes for x and y directions, respectively. Clearly, when space charge is not significant, only the terms  $\kappa_{x0}, \kappa_{y0}$  will be used in generating the transfer matrices and the case becomes equivalent to the discussions in Sec 2.2.2; however, for a more intense beam the defocusing space charge terms  $-\frac{2K}{X(X+Y)}$  and  $-\frac{2K}{Y(X+Y)}$  must be included in the matrix analysis.

In order to obtain the net focusing strength, knowledge of the beam sizes  $X$  and  $Y$  is needed. In typical experiments it's difficult to place a diagnostic over the desired transport line to get any information of the detailed evolution of  $X$  and  $Y$ . However, assuming no emittance growth we can calculate the beam envelopes by using Eq 2.10, generalized to non-symmetric distributions and given by [38]

$$X'' + \kappa_{x0}X - \frac{2K}{X+Y} - \frac{\epsilon_x^2}{X^3} = 0, \quad (2.41)$$

$$Y'' + \kappa_{y0}Y - \frac{2K}{X+Y} - \frac{\epsilon_y^2}{Y^3} = 0. \quad (2.42)$$

In order to solve those differential equations we have to assume some initial conditions  $(X_0, X'_0, Y_0, Y'_0, \epsilon_x, \epsilon_y)$  at the starting point  $z_0$ . This is a significant difference with the tomography for beams without space-charge (see Sec. 2.2.2) where no such assumption was necessary.

To check the validity of our assumptions we compare at  $z_1$  the calculated from the beam envelope and measured from the screen, beam sizes. In case they do not agree well we adjust the initial conditions and repeat our envelope calculations until we get a better agreement. Once the evolution of  $X, Y$  with respect of  $z$  is known we calculate the net focusing functions by using Eq. (2.39) and Eq. (2.40). Finally, from Eq. (2.31) and Eq. (2.32) we calculate the scaling factor and the rotation angle, respectively.

The complete beam tomography procedure for beams with space-charge is as follows:

1. Estimate the initial conditions at the starting location  $z_0$ .
2. Identify the correct initial conditions at  $z_0$ : For each magnet setting, solve the beam envelope equations and compare the calculated beam size to that from the measurement. If the two values are not within 10%, estimate new initial conditions and repeat the process until good agreement is achieved.
3. For each magnet setting solve numerically the envelope equation, get  $X\{z\}$ ,  $Y\{z\}$  along the beam line at 0.4 mm (or less) steps, and calculate the focusing strength for each step by using Eq. 2.39 and Eq. 2.40.

4. Use those focusing strengths to calculate the transport matrix (for each step) and then obtain the total transport matrix by multiplying those matrices. Now follow the steps 2-5 described in Sec. 2.2.2.
5. Change magnet focusing and repeat steps 3-4.

At the end of the scan integrate the filtered projections,  $Q$ , over the rotation angle by using Eq. 2.19.

## 2.4 Practical Tomography

### 2.4.1 Limitations

Phase space tomography requires the beam distribution to be rotated to a full  $180^\circ$  angle. Often this cannot be achieved by a single magnet because of several restrictions imposed by the experiment. Such restrictions are listed below:

Beam pipe: The beam size must be kept within a reasonable range when it travels through the accelerator in order to avoid the beam hitting the pipe or possible image-charge effects. Simulations indicate that image forces can have a significant impact on the beam dynamics, since it can cause emittance growth.

Screen size: Tomography relies on the beam distribution captured on the screen. Therefore, the beam size at the measurement point must be controlled to remain within the phosphor screen.

Magnet strength: In practice, the magnet strength is limited by the power supplies or hardware used. For instance, such a restriction can be the magnet current which on UMER cannot exceed  $\pm 3.5$  A. Additionally, operating at high quadrupole currents can destroy the quadrupole printed circuit.

Therefore, given those limitations, in some cases one quadrupole is not enough for a full  $180^0$  rotation of the phase-space. For instance, on UMER we have to employ three and sometimes four quadrupoles to ensure high quality phase spaces. Such configuration not only ensures a full rotation of the phase space but also guarantees that the beam remains far from the beam pipe and therefore the effect of image forces is negligible. Details about the UMER configuration will be discussed in the next section.

## 2.4.2 Tomography Configuration for UMER

Our tomography configuration on UMER is different than the one used in previous tomography works for two main reasons: First, on UMER, because of the above restrictions (see Se. 2.4.1), we have to use more quadrupoles than other studies which typically employed only one magnet. A schematic layout of the UMER configuration is demonstrated in Fig. 2.7(a). It consists of two sets of altering gradient (FODO) sections. Point A ( $z = z_0$ ) is located at the middle between two UMER quadruples and point B ( $z = z_1$ ) is at the location of our imaging diagnostic. The transport matrix consists of five drift matrices and four quadrupole matrices and is given by

$$M_1 = M_{D_5} M_{Q_4} M_{D_4} M_{Q_3} M_{D_3} M_{Q_2} M_{D_2} M_{Q_1} M_{D_1}, \quad (2.43)$$

and is illustrated schematically in Fig. 2.7(b). The particle motion will obey the equation

$$\begin{pmatrix} x_1 \\ y_1 \\ x_1 \end{pmatrix} = M_1 \begin{pmatrix} x_0 \\ y_0 \\ x_0 \end{pmatrix}. \quad (2.44)$$

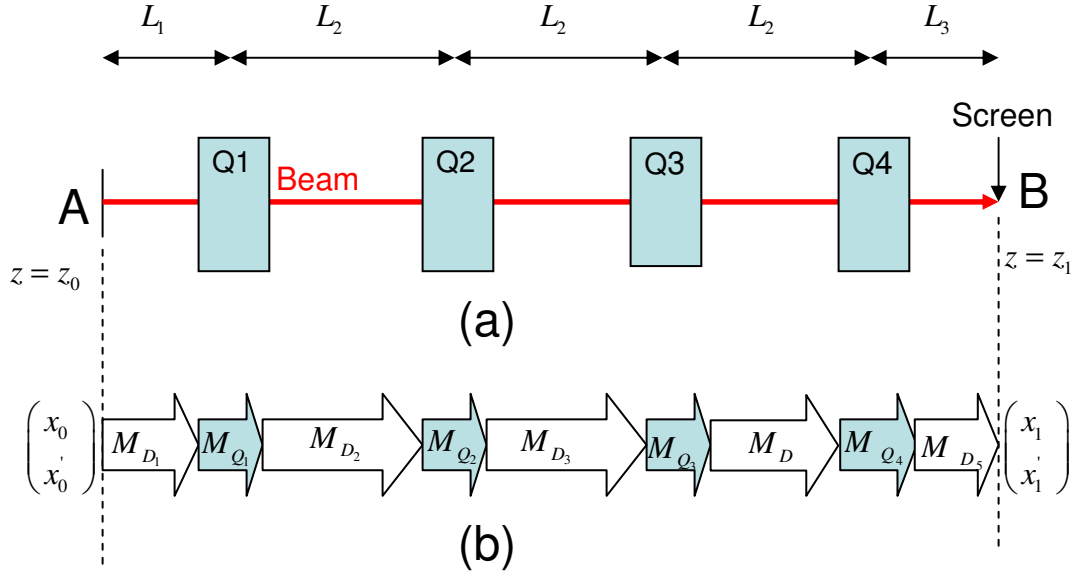


Figure 2.7: Schematic layout of the tomography configuration for UMER; (a) Orientation of quadrupoles; (b) Transfer matrices (indicated by arrows). The distance between A and B is 61.3cm, the distance between A and center of Q1 is  $L_1 = 8.0$  cm, the quadrupole center to center distance is  $L_2 = 16.0$  cm, and the distance between screen and center of Q4 is  $L_3 = 5.3$  cm.

The second different thing of our tomography analysis is the location of the phase space reconstruction. Following the process in Sec. 2.2.2 and using the matrix

of Eq. 2.43 we get knowledge of the phase space  $\begin{pmatrix} x_0 \\ y_0 \\ x_0 \end{pmatrix}$  at point A. This is not always



practical. For example it would be more desirable to reconstruct the phase space at point B since there we have a screen and so we can compare directly the reconstructed phase distribution with the actual beam distribution in configuration space. This phase space can be easily found by projecting the already known phase space at point A by using

$$\begin{pmatrix} x_d \\ x'_d \end{pmatrix} = M_{10} \begin{pmatrix} x_0 \\ x'_0 \end{pmatrix}, \quad (2.45)$$

where  $M_{10}$  is transport matrix corresponding to the magnet settings we are interested to get the phase space. We can combine now Eq. 2.44 and Eq. 2.45 and obtain a net transport matrix

$$M_{1,net} = M_1 M_{10}^{-1} \quad (2.46)$$

Therefore, using Eq. 2.46 as our transport matrix in our tomography analysis we can reconstruct the phase spaces at the location of the screen.

### 2.4.3 Image Processing Requirements

In this section we discuss precautions and requirements while doing image analysis so that we can successfully reconstruct the phase-space distribution.

In our data analysis the beam photos were saved as grayscale images. They consist of  $i$  and  $j$  spatial coordinates and their respective intensity values (known as *pixels*). They can be thought as 2D matrices,  $G$ , where the elements  $G(i, j)$  represent the intensity values at a given location  $(i, j)$ . The distance between adjacent pixels defines the resolution  $T$  (known as mm per pixel for beam photos). The range of the intensities allowed for each pixel is determined by the *bit depth*. For a bit of  $n$ , the

pixel has a depth of  $2^n$ . Hence, for 8 bit image, each pixel can have an intensity depth value of 256. The bit rate and resolution are determined by the camera specifications. Obviously, the higher the bit the more details about the image can be seen, however, this increase the computer memory requirement and slows the processing time. For our analysis we vary the bit from 8 to 16. When getting the photos care must be taken regarding the following effects:

Image Saturation While collecting the photos the image brightness can exceed the available intensity range an effect known as *saturation*. Therefore, care must be taken to avoid saturating the images by either decreasing the image brightness or using a camera with higher bit rate.

Image Intensity: The addition of all pixels of an image is known as total intensity. If  $N$  is the total number of pixels in  $i$  and  $j$  directions, then the total intensity is

$$I = \sum_j^N \sum_i^N G(i, j) \quad (2.47)$$

For beams the total image intensity is a measure of the available particles. While varying the magnet strength the numbers of particles have to be conserved. Therefore, a good practice is to measure the intensity of each individual photo after the scan. This might infer information about particle losses or about lens and screen linearity.

Image Centering: Misalignments caused either by the screen or the magnets often can lead to beam offsets. This means that the beam centroid do not match the actual photo center. Therefore, before doing Tomography, a post-centering process is usually necessary after collecting the beam photos in the experiment.

#### 2.4.4 Image Analysis Software

In this section we review the codes we developed for reconstruction and the order we use them in the process. We wrote four MATLAB codes that will: (1) Calculate the transport matrix, scaling factors and rotation angles (Code: `x_ScalF_RotA_Calc.m` - see Appendix A1); (2) Center the beam photos and calculate the total intensity (Code: `Photo_Cleaning.m` [41]); (3) Process the beam photos and by using the FBA method reconstruct the phase space (Code: `Tomography.m` [41]) and (4) Use the phase space to calculate the beam emittance (Code: `EmitCalc.m` – see Appendix A2).

We discuss now the procedure we follow and the order we use the above codes to reconstruct the phase space distribution.

Step1: First we generate a table which contains the values of the desired magnet strengths. Next, we run `x_ScalF_RotA_Calc.m`:

The code reads those values, solves numerically the beam envelope equations (using Eq. 2.41 and Eq. 2.42), obtains a set of values for  $X_i(z)$  and  $Y_i(z)$  at a step  $t$  and calculates the corresponding focusing strength,  $\kappa_{xi}(z)$ , by using Eq. 2.39. This is illustrated in Fig. 2.8. Then, by assuming a constant focusing within each step the code gets the transport matrix  $M_i$  and finally calculates the net transport matrix by doing a superposition of those matrices ( $M_1 = M_{i+2}M_{i+1}M_i \dots$ ). From the net matrix it calculates the scaling factors and rotation angles for a given set of initial conditions. The output of the code is a table that contains the quadrupole strengths, the resulting

scaling factors and corresponding rotation angles. Same approach applies for the y direction also.

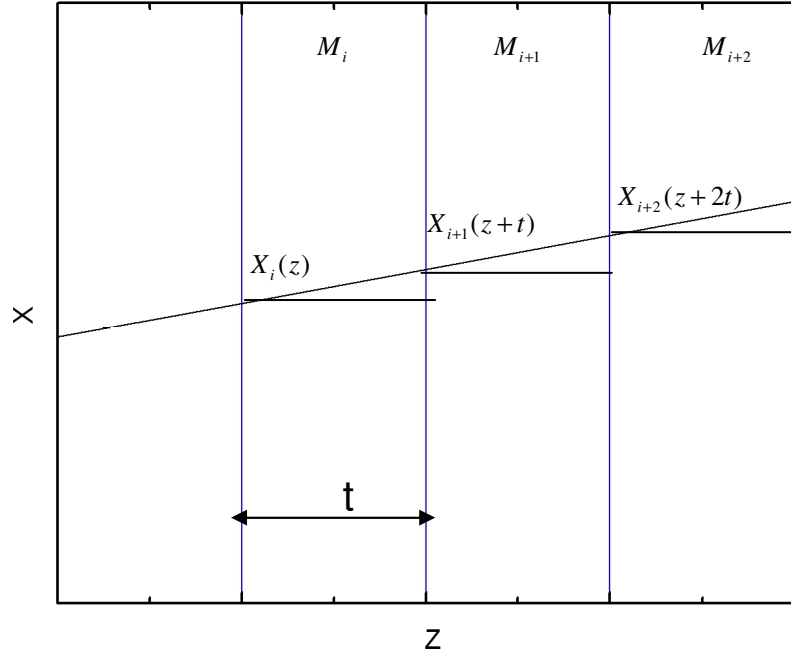


Figure 2.8: Plot shows the numerical solution of the beam envelope equation (Eq. 2.41). Step  $t$  should be kept below 0.4 mm and the beam size as well focusing is assumed to be constant within this region.

Step2: Run Photo\_Cleaning.m:

The code calculates the beam centroid by using the formula:

$$x_c = \sum_i^N \sum_j^N iG(j,i)/I, \quad (2.48)$$

$$y_c = \sum_i^N \sum_j^N jG(j,i)/I. \quad (2.49)$$

where  $I$  is the total beam intensity given by Eq. 2.47. Then, it calculates the distance from the photo center  $(N/2, N/2)$  and brings the beam photo at that center by doing

the following transforms:  $x_c \rightarrow x_c - (x_c - N/2)$  and  $y_c \rightarrow y_c - (y_c - N/2)$ . After that it saves the new image. Finally, it calculates the total intensity,  $I$ , of each photo by using Eq. 2.47 and saves it in a file.

Step3: Run Tomography.m:

The code reads the beam photos created in step 2 and converts it to ASCII-text delimited strings, with each delimiter separating relative pixel intensities. Then by reading the table generated in step 1 it assigns a projection angle and scaling factor to each photo set. Next the program calculates the profiles along x and y and scales them appropriately following the procedure described in Sec. 2.2.2. Finally, it uses those profiles to reconstruct the phase space distribution.

Step4: Run the EmitCalc.m:

The code calculates the  $4 \times rms$  unnormalized emittance by using the formula  $\epsilon_x = 4\sqrt{\langle x^2 \rangle \langle x'^2 \rangle - \langle xx' \rangle^2}$  (see Sec. 1.1.2). To do so it converts the phase space in Step 3 to ASCII-text delimited strings, with each delimiter separating relative pixel intensities. Then, if  $N$  are the number of pixels in vertical and horizontal directions and  $M(i, j)$  is the phase space at a point  $i, j$  it calculates the second order moments by using the equations

$$\langle x^2 \rangle = T^2 \left[ \sum_i^N \sum_j^N i^2 M(j, i) \right] / I, \quad (2.50)$$

$$\langle x'^2 \rangle = T^2 \left[ \sum_i^N \sum_j^N j^2 M(j, i) \right] / I \quad (2.51)$$

$$\langle xx' \rangle = T^2 \left[ \sum_i^N \sum_j^N (ij) M(j, i) \right] / I, \quad (2.52)$$

were  $I$  is the total intensity and  $T$  is the spacing between adjacent pixels (in mm/pixel). Then, the total emittance is

$$\epsilon_x = \frac{4T^2}{I} \sqrt{\left[ \sum_i^N \sum_j^N i^2 M(j,i) \right] \left[ \sum_i^N \sum_j^N j^2 M(j,i) \right] - \left[ \sum_i^N \sum_j^N (ij) M(j,i) \right]^2}. \quad (2.53)$$

where we are assuming that the centroid of the phase-space is at the origin.

## 2.5 Summary

We described the basic theory to apply tomography to reconstruct the beam phase-space. We showed that the technique makes no *a priori* assumptions about the beam distribution when the beam has negligible space-charge. We also extended the technique to beams with space charge. Our approach assumes uniform distributions where the space-charge force becomes linear. Next, we reviewed the tomography magnet configuration for UMER and demonstrated the necessity to use multiple magnets for our reconstruction. Finally, we reviewed the computer codes that we use for our analysis.

## Chapter 3 Tomography Simulation

Over the last 30 years tomography has been successfully applied to reconstruct the phase space distribution for relativistic beams [20, 21, 24, 42]. Because of the high beam energy, space-charge effects were ignored on those studies. In Chap. 2 we proposed a method to extend further the tomography algorithm to beams with space-charge. The model assumed linear space-charge forces. Even though the first experimental data were reported [25, 43], still some questions remain about the limitations of the method. Can the technique be used for beams with intense space charge? Could a simple linear approximation accurately reproduce the beam phase space and if yes how many projections are required? In addition, will tomography map the phase distribution for beams with complex distributions? For instance, what would happen if the beam starts with a hollow velocity distribution (repeatedly observed in thermionic gridded guns)? In order to answer such questions, we simulate a tomography beam experiment using the electrostatic particle-in-cell code WARP [8]. In our simulation we use beams with different initial distributions and with different degrees of space-charge intensity. We show that tomography produces phase spaces with superior accuracy even for cases when the beam space-charge is high. Furthermore, we discuss the effects of various errors in the data collection process for the reconstruction and show that the crucial factor is not necessary the number of projections but the range of angles over which projections are taken.

The outline of this chapter is as follows: In Sec. 3.1, we provide a short general description about the simulation process we use. Then, in Sec. 3.2, we examine the effect of various errors in the data collection process on the reconstructed phase space (number of projections, rotation angle, and uncertainties in measurements). In Sec. 3.3, we examine the accuracy of the diagnostic for beams with different space-charge intensity. Next, in Sec. 3.4 we input different initial beam distributions in the simulation (for instance hollow-velocity or five beamlet distributions) and check the accuracy of our tomography analysis. In Sec. 3.5 we use tomography to simulate transverse density waves. Finally, in Sec. 3.6 we report a summary of our results and derive our conclusions.

### **3.1 WARP Simulation**

As discussed in Chap. 2 application of tomography to beams with space charge requires some assumptions to be made, for instance use of linear space charge forces. In this section we are interested to validate the reconstruction approach, by simulating the tomography process using the self-consistent electrostatic particle-in-cell code WARP [8]. In the simulation, WARP will include all these effects that tomography is ignoring and are summarized in Table 3.1.



Table 3.1: Assumptions made to generate the beam phase space by WARP (left) and tomography (right)

<b>WARP</b>	<b>Tomography</b>
Nonlinear space charge	Linear space charge
Emittance growth allowed	Constant emittance
Image charge forces included	Image charge forces ignored
Arbitrary distribution	Uniform distribution

The computer code WARP has been successfully benchmarked against UMER experimental data in the past [44]. The code simulates space charge effects in 2D or 3D by advancing particles in a transverse slice under the impact of external forces and self-consistent self-fields. The self-fields are calculated on a mesh of sufficient resolution to capture the beam potential variations and the particles are advanced using the leap-frog algorithm. In our case we use the x-y 2.5-D slice model which has been shown to be accurate [45] since the beam is long in z compared to the pipe diameter and varies little during its propagation over a longitudinal distance comparable to the beam diameter. In WARP we use a 512x512 grid for the Poisson solver, a step size of 2 mm along z, and 640,000 particles. Running a large number of test simulations with more particles or higher resolution resulted in no perceptible difference in the final result.

We select the magnet configuration for our simulation to be as close as possible to that on UMER; therefore, we use the four quadrupoles layout shown in

Fig. 2.7 in Chap. 2. Simulating the tomography under that geometry will give us more confidence about its future applicability in the actual experiment (see chapter 4). Since the quadrupole nonlinearities are found to play a minor role in the behavior of the beam [45] their magnetic fields are modeled using a hard edge approximation

where the effective length is defined as  $l_{eff} = 1/B_{peak} \int_{-\infty}^{\infty} B(z, r=0) dz$ .

The simulation is initialized upstream of Q1 (point A – the center of a dipole on the equivalent UMER lattice) and the photos and phase space are generated downstream of Q4 (point B – the position of the fluorescent screen on UMER). For each quadrupole current setting, we run a simulation; collect a snapshot of the beam density in configuration space at B and save it in 8-bit tif format. The tomographic reconstruction is applied to those simulated images to produce a phase space that will then be compared to the actual phase space obtained directly from the simulation. The phase space generated directly by WARP does not make the assumptions that tomography does (these assumptions are listed in Table 3.1) and therefore will be used as a prototype to compare the quality of our tomography process. Repeating this process for different initial distributions and with different degrees of space charge intensity provide us with confidence in the technique.

### 3.2 Error Analysis

We use the simulation to investigate the effects of various errors in the data collection process such as the angular step needed (Sec. 3.2.1), the total angular span required (Sec. 3.2.2) and the effect of magnet strength uncertainties in the

reconstruction (Sec. 3.2.3). For all cases presented in this section the beam parameters are: 0.6 mA, 6.0  $\mu\text{m}$ , 0.3, 1.3 mm for the beam current, emittance, intensity parameter and size, respectively. In our simulation we assume the beam starts with a semi-Gaussian (S-G) distribution, which is commonly used for modeling space-charge-dominated beams. In such a distribution the particle density is uniform across the beam, while the velocity profile is Gaussian with uniform temperature. This distribution is preferred since it approaches thermal equilibrium in the space-charge limit.

### 3.2.1 Angular Resolution

In this section we study how the angle difference between two adjacent projections affects the quality of the tomographic reconstructed phase space. We show that if this difference is high it can lead to numerous artifacts on the reconstructed image. To illustrate this point, in Fig. 3.1 we plot the angular difference (angular step) between adjacent projections versus the projection number for three different cases. In Fig. 3.2 we show the resulting reconstructed phase space. For all cases the total rotation of the phase space distribution was  $180^\circ$ . Case 1 corresponds to the case with the highest angular step (relevant to Case 2 and 3) where its maximum value reached  $30^\circ$ . For this case, the appearance of aliasing streaks is evident (15% of the peak intensity) along the phase space distribution. The appearance of streaks is less visible (5% of the peak intensity) when the maximum angular step is below  $24^\circ$  (case 2). However, in case 3 where the angular step is kept minimum (less than  $14^\circ$ ), the aliasing streaks clearly disappear. Therefore, we can conclude that the final

reconstruction is sensitive to the angular difference between two adjacent projections. If the angular step is higher than  $14^\circ$  it can result to aliasing streaks with intensity that scales as the angular difference.

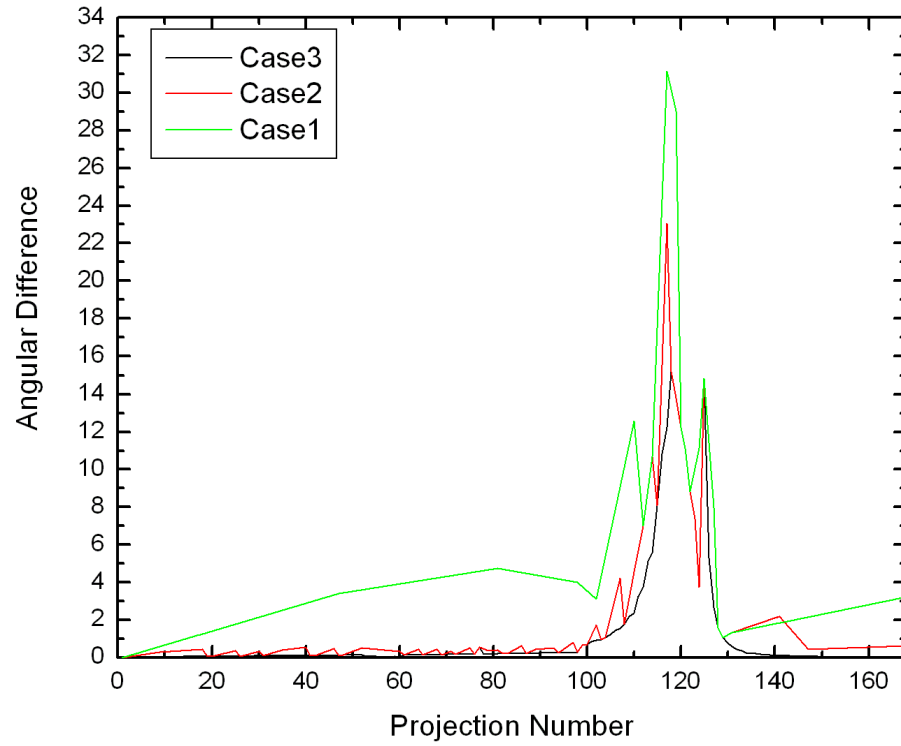


Figure 3.1: Angular difference between adjacent projections versus the projection number for three different cases.



Figure 3.2: Phase-space distributions for the three different cases. Note that for all cases the total phase space rotation was  $180^{\circ}$ .

### 3.2.2 Angular Span

In this section we will test the sensitivity of the reconstructed phase space to the total rotation angle of the phase space. We show that when the phase space rotation is less than  $180^{\circ}$  it can result to serious artifacts which become worse as the total rotation decreases. In order to illustrate this point we select to do a reconstruction for three different phase space rotations and our results are demonstrated in Fig. 3.3. The number inside the photo indicates the total phase-space rotation achieved. As it is evident when the total rotation is far from  $180^{\circ}$  aliasing lines are visible. For the case of  $169.2^{\circ}$  rotation, the intensity of the aliasing lines reaches 25% of the peak intensity making it difficult to distinguish the reconstructed image. The artifacts become less visible as the rotation is increased to  $174.6^{\circ}$  (10% of the peak intensity) and eventually disappear as the phase space rotation approaches  $179.2^{\circ}$ . Therefore, we conclude that a close to  $180^{\circ}$  phase space rotation is necessary for minimization of any noise artifact.



Figure 3.3: Phase Space reconstruction for different phase space rotations.

### 3.2.3 Magnet Settings

Finally, since in real experiments there is an uncertainty between the actual value and the set value in quadrupole current, we want to address the issue of quadrupole current systematic errors in the phase space recovery process. Figure 3.4 depicts the recovered electron beam phase space using 168 projections, with (a) 1% simulated systematic error, (b) 3% simulated systematic error, and (c) 5% simulated systematic error. We conclude that the uncertainty in the quadrupole current values will affect the recovered phase space. Quantitatively, if we measure the beam emittance we get 5.7, 5.4, 5.1  $\mu m$  for the cases where we have 1, 3%, and 5% error, respectively. Comparing these values to the emittance that we found for the case where no uncertainties in currents were present (6.0  $\mu m$ ) we conclude that small systematic errors in the quadrupole current have a moderate impact on the resulting emittances.

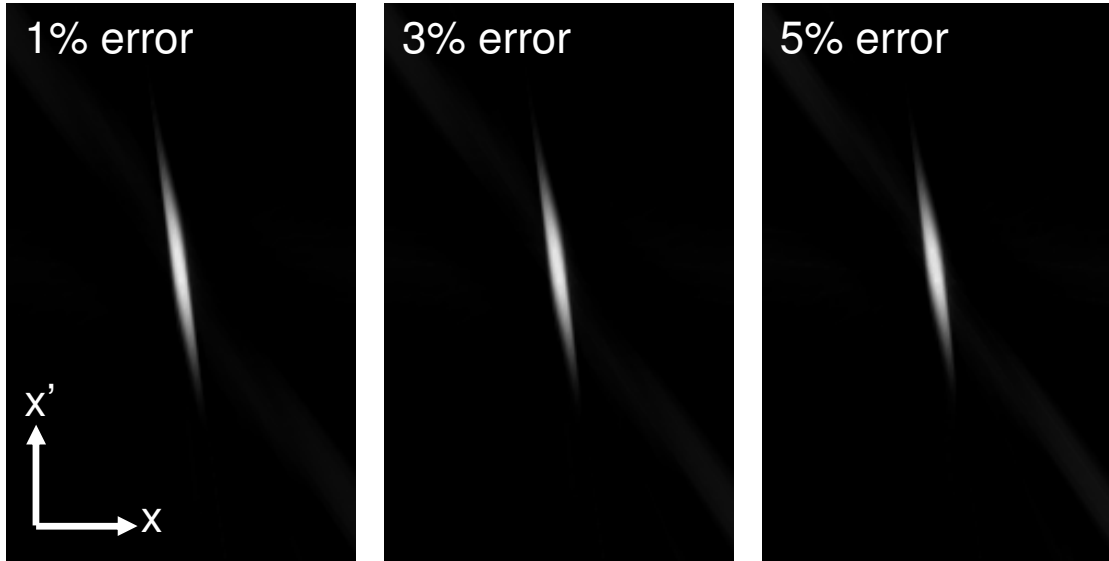


Figure 3.4:  $X'X$  phase space distribution of the pencil beam with different simulated systematic errors. (a) 1% error, (b) 3% error, (c) 5% error

### 3.3 Verification of Space-Charge Reconstruction

In this section we are interested to simulate our tomography diagnostic for beams with different space-charge intensity. Our aim is to test how accurate finally tomography is when the beam enters the space-charge dominated regime. Following the process we described in Sec. 3.1, the accuracy of our tomography diagnostic will be examined by comparing its reconstructed phase spaces to the phase-spaces generated directly by WARP. In our simulation we use three beams one of which is emittance dominated, while the other two are strongly space charge dominated. The current, initial beam size and intensity parameter of those three beams is listed in Table 3.2.

Table 3.2: Beam parameters of our simulated beams. Note that the beam is assumed to be round, initially.

$\chi$	$I(mA)$	$r_0(mm)$	Total Projections	Maximum Angular Step	Angular Span
0.30	0.6	1.3	168	$14.0^0$	$179.2^0$
0.72	7	2.8	152	$14.9^0$	$178.0^0$
0.90	24	4.8	126	$20^0$	$175.0^0$

$r_0$  :initial beam size

For the simulation we use the configuration illustrated in Fig. 2.7 and reconstruct the phase space at  $z = z_1$ . We assume the beam starts with a semi-Gaussian (S-G) distribution. The number of projections, the total angular span and the maximum angular step between adjacent projections for each case is shown in Table 3.2. The settings of the scanning magnets were such to ensure that the beam was remained far from the beam pipe eliminating so particle losses and image forces. Due to the very large beam sizes obtained while scanning the magnets for the 24 mA beam, the total phase space rotation was restricted to  $175^0$ . The recovered phase spaces at  $z = z_1$  are shown in Fig. 3.5. All plots correspond to the case where the focusing strength for Q1 and Q3 was set  $\kappa_1 = \kappa_3 = -235.2 \text{ m}^{-2}$  (along x) and Q2 and Q4 was set at  $\kappa_2 = \kappa_4 = 235.2 \text{ m}^{-2}$  (along x).



Figure 3.5(a) corresponds to an electron beam with current equal to  $I = 0.6$  mA and intensity parameter  $\chi = 0.30$ . The tomography recovered phase space is shown in Fig. 3.5(a) (right). Due to the low current, space charge forces are relatively low and were neglected in our analysis. Figure 3.5(b) shows the recovered phase spaces for the  $I = 7$  mA. Since its intensity parameter is  $\chi = 0.72$  this is a space-charge dominated electron beam, therefore space charge effects must be taken into account in the tomography reconstruction process. The simple method we employ here, (described in detail in section 2.2), is a linear space charge correction estimated from the beam envelopes. Finally, Fig. 3.5(c) depicts phase space recovery for a very intense beam with  $I = 24$  mA and  $\chi = 0.90$ . Table 3.3 summarizes the calculated emittances from WARP and Tomography for those three beam intensities.

The difference in emittances is at its highest for the 24 mA beam. This is mainly for two reasons: One is the aliasing streaks (clearly seen in Fig. 3.5(c)). Those streaks are a source of error in the emittance calculation from tomography. In our simulation the total rotation was only  $175^\circ$  and as shown in Sec 3.2.1 streaks can appear if the phase space rotation is not complete. The second reason is the substantial amount of space-charge which in turn can result to non-linear forces not included in our analysis. Still, given the high beam intensity, the agreement is good and the error is far less from other methods such as a quadrupole scan [15].

Tomography accurately reconstructed the phase space for beams with moderate content of space-charge ( $\chi \leq 0.72$ ). The emittance error was below 5%. Therefore, our linear approximation model is proven to be effective in the reconstruction in the presence of moderate amount of space charge. Simulations for

more intense beams ( $\chi = 0.9$ ) suggest a higher percentage of error but still the agreement between tomography and simulation is relatively good.

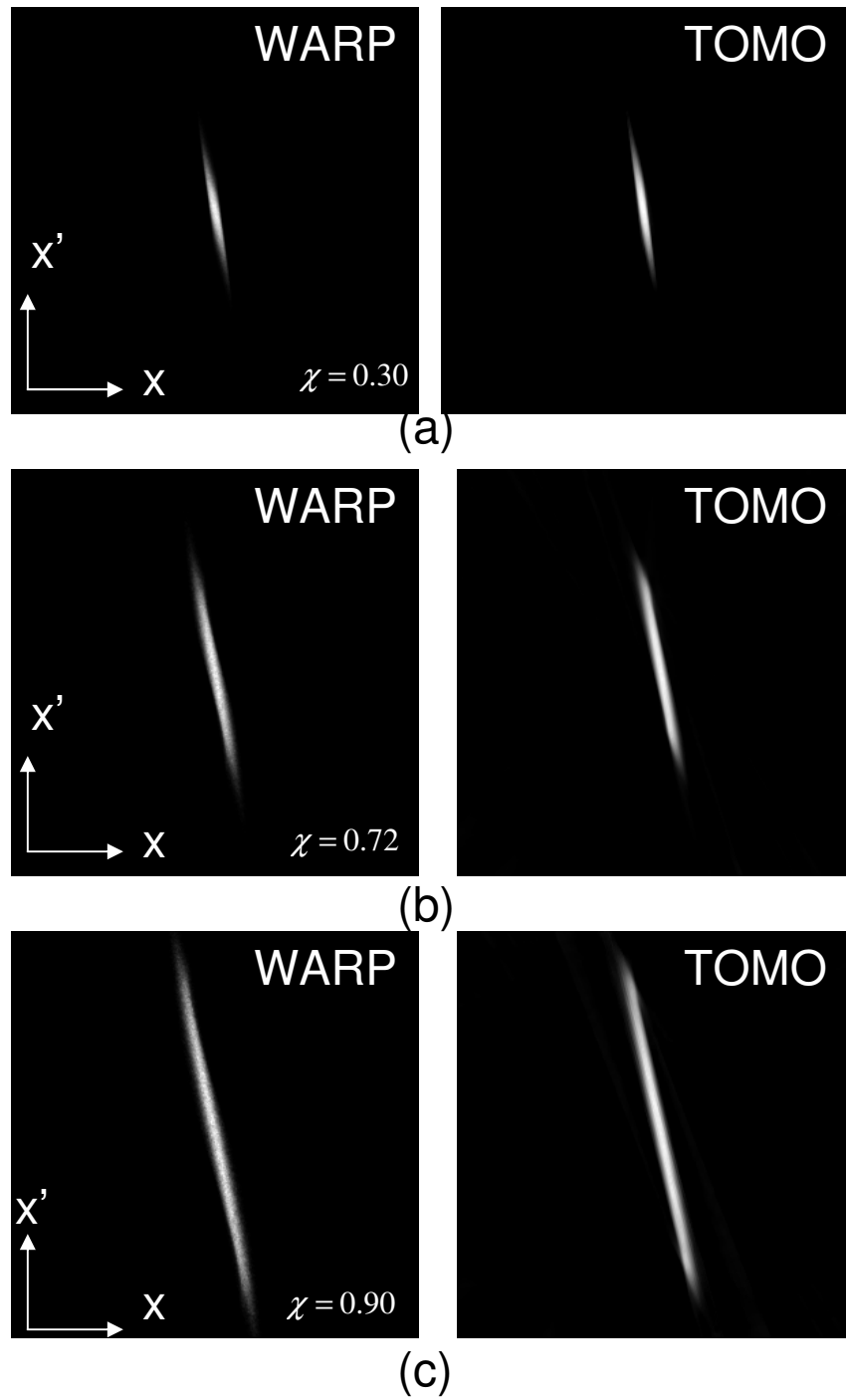


Figure 3.5: Recovered phase spaces from WARP (left side) and Tomography (right side) for beams with different intensity parameters: (a)  $\chi=0.3$  (b)  $\chi=0.72$  (c)  $\chi=0.9$

Table 3.3 Emittances obtained by WARP and Tomo-Code

$\chi$	$I(mA)$	$\varepsilon_x(\mu m), WARP$	$\varepsilon_x(\mu m), TOMO$	Error (%)
0.30	0.6	6.1	5.9	3.2
0.72	7.0	14.5	15.2	4.8
0.90	24.0	29.0	31.1	7.2

### 3.4 Initial Distributions

In beam physics the initial beam phase space distribution is an important factor in determining its evolution. Part of the challenge of any distribution measurement technique is that it should make *no a priori* assumption about those initial distributions but instead should be equally accurate for different input profiles. In this section we simulate our tomography diagnostic using four different initial distributions and will compare our reconstruction with direct WARP simulation. Similarly as described in Sec 3.1, we will initiate our simulation at  $z = z_0$  and reconstruct the phase space at  $z = z_1$ . The distributions to be explored are the Semi-Gaussian (see Sec. 3.4.1), Hollow-Velocity (see Sec. 3.4.2), Hollow-Spatial (see Sec. 3.4.3) and Five-Beamlet (see Sec. 3.4.4). The WARP generated and tomography reconstructed phase spaces are shown in Figure 3.9 at the second and third column, respectively. The calculated 4xrms emittances are listed in Table 3.5. For all cases the beams are equivalent in rms sense, meaning that they have the same current, energy, rms emittance and size. The detailed beam parameters used for our analysis are listed

in Table 3.4. The number of projections, angular steps and spans are identical to those used for this beam in Sec 3.3 (second row of Table 3.2).

Table 3.4: Beam parameters for the 7 mA beam.

Beam Energy	10 keV
$\beta (= v/c)$	0.2
Beam Current	7 mA
Mean Beam Radius	2.8 mm
Mean Beam Divergence	-13.3 mrad (in x)
Emittance, 4xrms	15 $\mu\text{m}$

### 3.4.1 Semi-Gaussian Distribution

We start our simulation by assuming that the beam starts with a semi-Gaussian at  $z = z_0$ . Such a distribution is shown in Fig. 3.8(a). This case is identical to the case described in Sec. 3.3. The beam distribution at  $z = z_1$  is shown in Fig. 3.9(a) and clearly there is good agreement between tomography and simulation.

### 3.4.2 Hollow Velocity Distribution

A hollow velocity distribution is of interest not only because it has been experimentally observed on UMER [46] but also it tends to be a general feature of thermionic gridded electron guns. In a gridded electron gun, a grid located in front of the cathode is used to control the beam current and beam shape. However, when the beam reaches the grid a certain percentage of the current can pass through while

others will be intercepted by the mesh and form the grid current. Such a current will modify the field lines that the beam particle sees and hence strongly perturbing its initial particle distribution. Through this process some particles gain substantial amount of transverse energy causing hollowness in velocity space.

It has been shown [44] that such a hollow distribution can be modeled if we use a radially hollowed velocity (with azimuthal symmetry) that is obtained by rotating a Gaussian distribution with width  $v_{th}$  and offset  $\alpha$  from the origin around a circle of radius  $\alpha$ . The cross section of such a distribution is illustrated in Fig. 3.6. In our case, the parameters  $v_{th}$  and  $\alpha$  are calculated to be 0.0011 and 0.0033, respectively. In that way the beam rms size and emittance are equal to the Semi-Gaussian distribution case in the previous section. The beam distribution at  $z = z_0$  is illustrated in Fig. 3.8(b). Downstream, at  $z = z_1$ , the initial uniform beam in configuration space becomes hollow (Fig. 3.9(b)). This is due the fact that, initially, not all particles have the same velocities and hence evolve different along the beamline. Hollowness is visible also in phase space and interestingly enough tomography captures those details with high level of accuracy. This is also quantified by the emittances which agree within 4%.

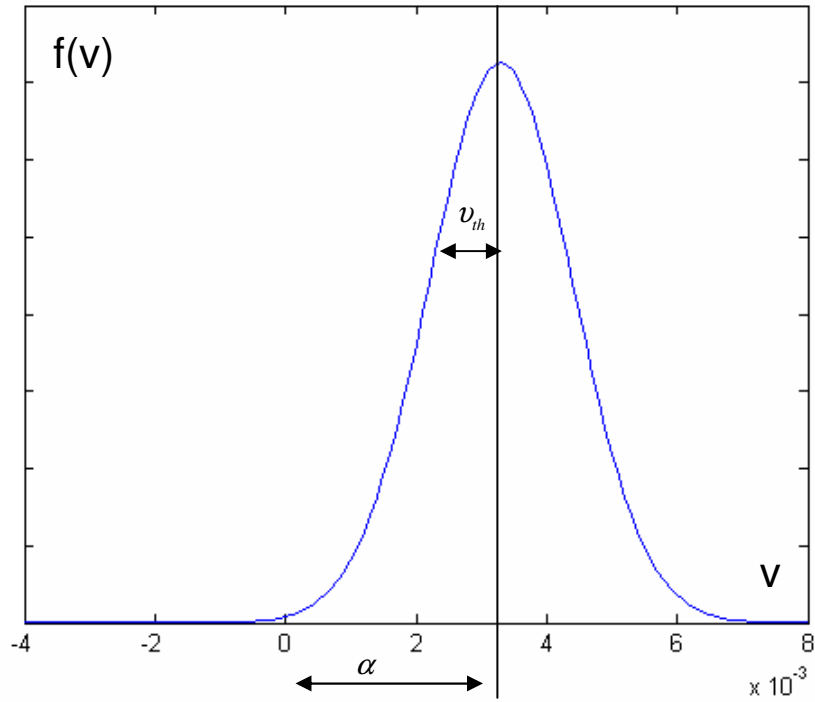


Figure 3.6: The Gaussian velocity distribution that is rotated around a circle of radius  $\alpha$

### 3.4.3 Hollow Spatial Distribution

Of particular interest is a beam distribution that is not uniform in configuration space. Such a situation can exist in many experiments due to nonlinear focusing or nonuniform emission from the cathode. We model a hollow density distribution with a sharp edge at radius  $r_0$ . Then, if the degree of hollowness is quantified by a dimensionless parameter,  $h$ , the hollow spatial distribution in our simulation is described by

$$f(r, h) = h + (1 - h) \frac{r^2}{r_0^2}, \quad (3.1)$$

where for our case  $h=0.5$ . If  $r_u$  is the radius of the equivalent uniform beam (see Table 3.4) in rms sense, then the ratio  $r_u / r_0$  is determined by

$$\frac{r_u}{r_0} = \sqrt{\frac{2(h+2)}{3(h+1)}}, \quad (3.2)$$

and therefore  $r_u / r_0 = 1.055$ . The initial hollow velocity distribution used in our simulation is illustrated in Fig. 3.8(c). Downstream, hollowness is still visible in configuration space (Fig. 3.9(c)) but the phase spaces are fairly uniform. Good agreement between tomography and simulation is visible. This is also quantified by the emittances which agree within 4%.

#### 3.4.4 Five-Beamlet Distribution

Finally, we incorporate a highly asymmetric or non-round initial beam distribution. Such a highly nonuniform distribution introduces nonlinear space charge forces [7]. Therefore, it will be a good test of the validity of our linear tomography model. To generate an asymmetric distribution we use a quincunx pattern in the xy (similar to the number 5 of a die) where we intercept a uniform S-G beam with a 5-beamlet mask. Such an experiment has applications in heavy ion fusion where the concept of merging multiple beamlets has been used extensively [29, 30].

Figure 3.7 shows a schematic layout of the initial beamlet distribution and Fig. 3.8(d) shows the actual photo at  $z = z_0$ . Assuming uniform beamlets, the initial size, current and emittance of each beamlet is [7]:

$$r_{let} = \sqrt{r_u^2 - 1.6\delta^2}, \quad (3.3)$$



$$\mathcal{E}_{let} = \frac{r_{let}}{r_u} \mathcal{E}, \quad (3.4)$$

$$I_{let} = \frac{I}{5}, \quad (3.5)$$

where  $r_u$ ,  $I$ ,  $\mathcal{E}$  is the size, current, and emittance of the equivalent uniform beam (see Table 3.4), respectively;  $\delta$  is the beamlet center to center distance;  $r_{let}$ ,  $I_{let}$ ,  $\mathcal{E}_{let}$ , are the radius, current and emittance for each beamlet, respectively. At  $z = z_1$  the beam distribution in configuration space and phase-space is shown in Fig. 3.9(d). An interesting result is the almost merging of the beamlets in configuration space but at the same time the beamlets are separated in phase space. Another surprising fact is the superior agreement between WARP and Tomography (third column) despite the linear approximation used in our model. Such result suggests that our tomography method appears promising to reconstruct phase spaces of complex nonuniform distributions.

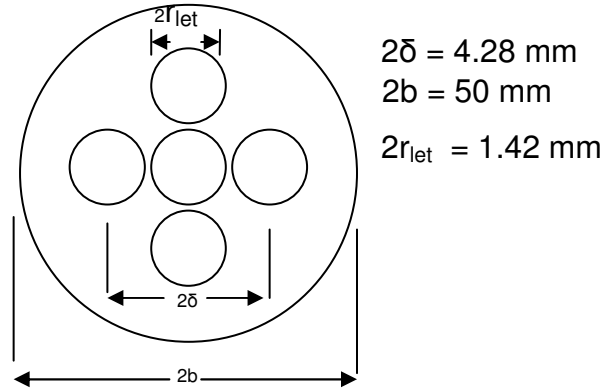


Figure 3.7: Schematic layout of the five beamlet distribution. Note that  $2b$  is the diameter of the beam pipe. Distances are not to scale.

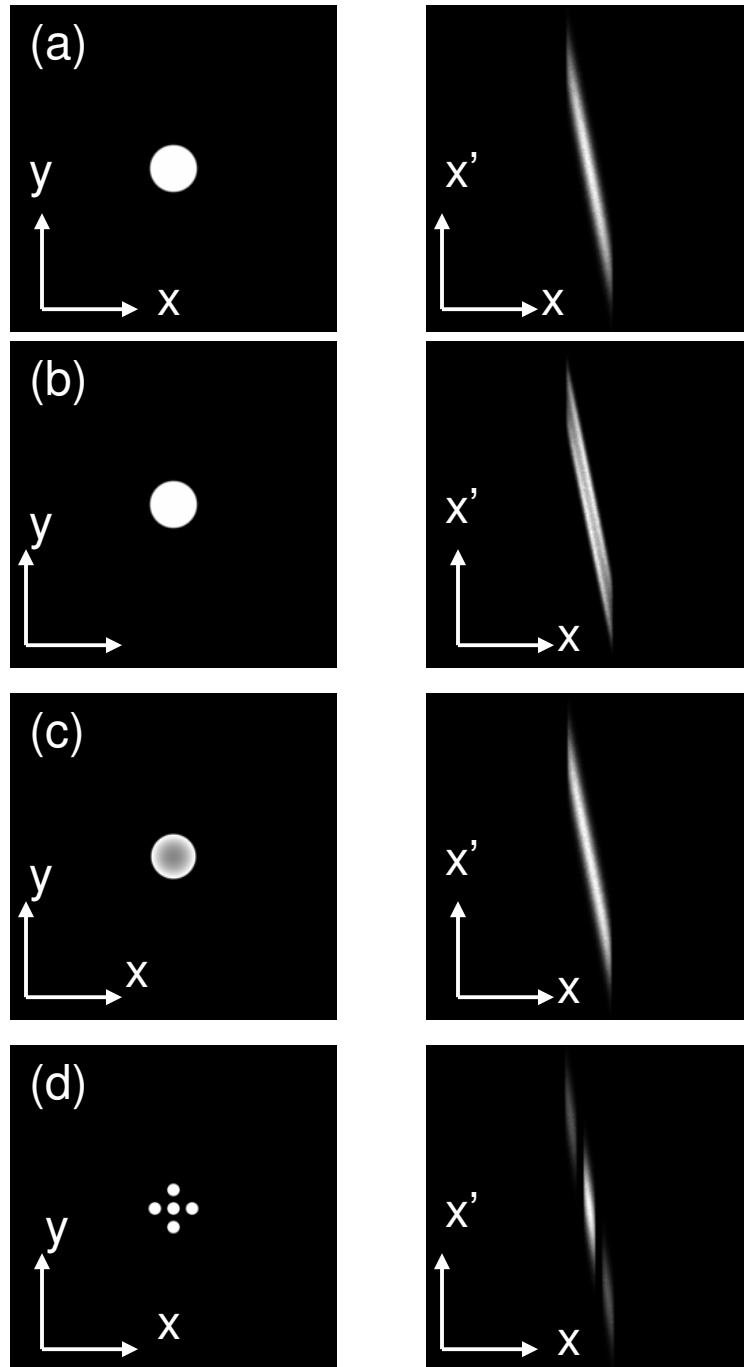


Figure 3.8: Beam distributions in configuration space (left) and beam distribution in phase space (right) from direct WARP simulation at  $z = z_0$

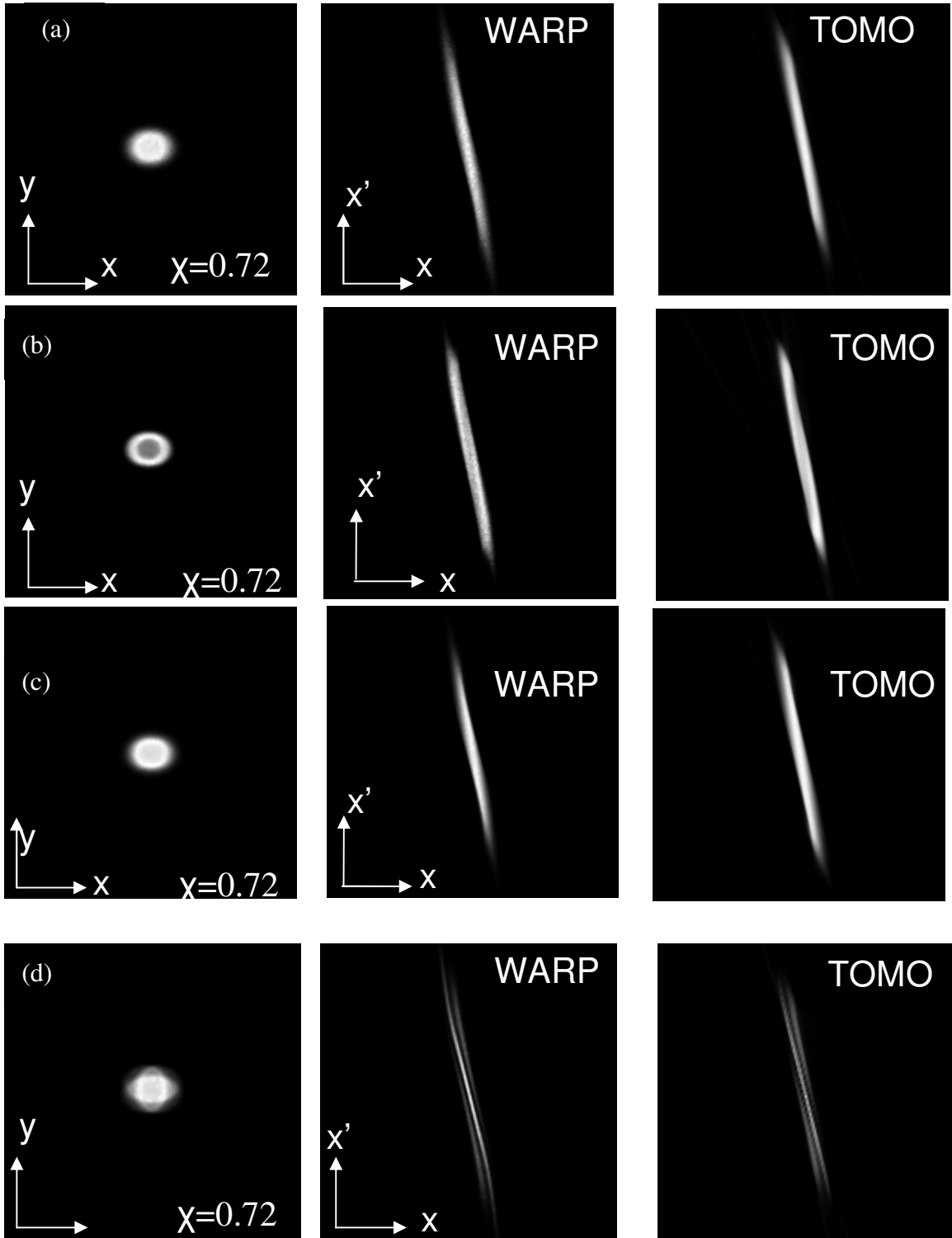


Figure 3.9: Phase spaces for the 7mA obtained by WARP (second column) and Tomography (third column) at  $z = z_1$  using different input distributions.

Table 3.5: Emittances obtained from the phases-spaces in Fig. 3.9 by WARP and tomography

Distribution	$\varepsilon_x (\mu m), WARP$	$\varepsilon_x (\mu m), TOMO$	Error (%)
Semi-Gaussian	14.5	15.2	4.8
Hollow Velocity	14.3	14.9	4.0
Hollow Space	14.7	14.2	3.5
Five-Beamlet	16.7	15.6	6.5

### 3.4.5 Conclusion

In this section we simulated the tomography diagnostic for beams with different initial distributions. We showed that by treating beams with non uniform distributions as equivalent (in rms sense) to uniform beams we can obtain very accurate phase space maps. This was true also when we used highly asymmetric distributions (such as the five beamlet distribution in Sec 3.4.4). Even though such distribution will introduce non linear space-charge forces our linear model proves to be effective in the reconstruction process with an error less than 7%.

## 3.5 Transverse Density Waves

Beams normally reach an equilibrium state only after traversing a long distance in a transport system. Thus, beams are typically far from equilibrium near their source. Many factors contribute to the beam evolution towards equilibrium,

causing emittance growth in the process: envelope mismatch, nonlinearities and anisotropies in the focusing system, dispersion and bending, collimation, etc. An example of a nonequilibrium beam distribution is the Semi-Gaussian (S-G) distribution introduced above. It can be used, for example, to model the wavelike beam evolution described by Bernal et al. [47]. A space-charge dominated electron beam emerging from an aperture develops a ring of charge near its edge that progresses towards the beam's center as the beam propagates in a solenoid or quadrupole system. Simulations with WARP starting with a S-G distribution accurately reproduce the density modulation in the experiment. In a similar fashion, Kishek *et al.*, [48] reports space-charge modes, similar to those observed before, in simulations of nonequilibrium charged particles beams with anisotropy.

We are interested in using tomography as a diagnostic tool to study nonequilibrium dynamics in space-charge-dominated beams. In order to do that, we simulate the 7 mA beam starting with a SG distribution and observe the beam evolution by mapping its phase space. The phase space is reconstructed by scanning quadrupoles Q1, Q2, Q3 and Q4, and is projected downstream of Q4 as described in Sec. 2.4.2. Since we are interested in investigating beam propagation over a long distance, we add a series of alternating-gradient quadrupole (FODO) cells downstream of Q1, with appropriate strength so that the beam remains matched as it passes through them. Our results are shown in Fig. 3.10, which demonstrates that tomography is powerful enough to capture the details of the distribution including the “wings” that correspond to the propagating space charge waves. The number inside each photo indicates the number of quadrupoles upstream of Q1 (does not include the

4 quadrupoles used for tomography). The sharp edges of the initial spatial distribution result in a strong force imbalance at the beam edges. As a consequence, the beam-edge particles experience forces that are very different from those affecting the bulk particles. Edge particles tend to move outside the beam as the latter is transported in the FODO lattice (Figs. 3.10(c), 3.10(d)). However, the strong external focusing brings the edge particles back near the beam edge (Fig. 3.10(e)), creating a wavelike density modulation downstream. Table 3.6 summarizes the emittance measurements as calculated by tomography and WARP. We can conclude that the quality of the tomography process can be established by its ability to capture the wave-like behavior on the recovered phase space, in good agreement with the WARP-generated phase spaces. Beside this good agreement, the emittance values agree also very well with error close to 5%.

Table 3.6: Beam emittances at different positions along the beam line as calculated from the phase spaces generated by tomography and WARP

<b>Z (cm)</b>	61.3	77.3	109.3	141.3	173.3
<b><math>\epsilon_{x,\text{Tomography}}</math> (<math>\mu\text{m}</math>)</b>	15.2	15.2	14.8	14.1	15.7
<b><math>\epsilon_{x,\text{WARP}}</math> (<math>\mu\text{m}</math>)</b>	14.5	14.7	14.5	15.0	14.8

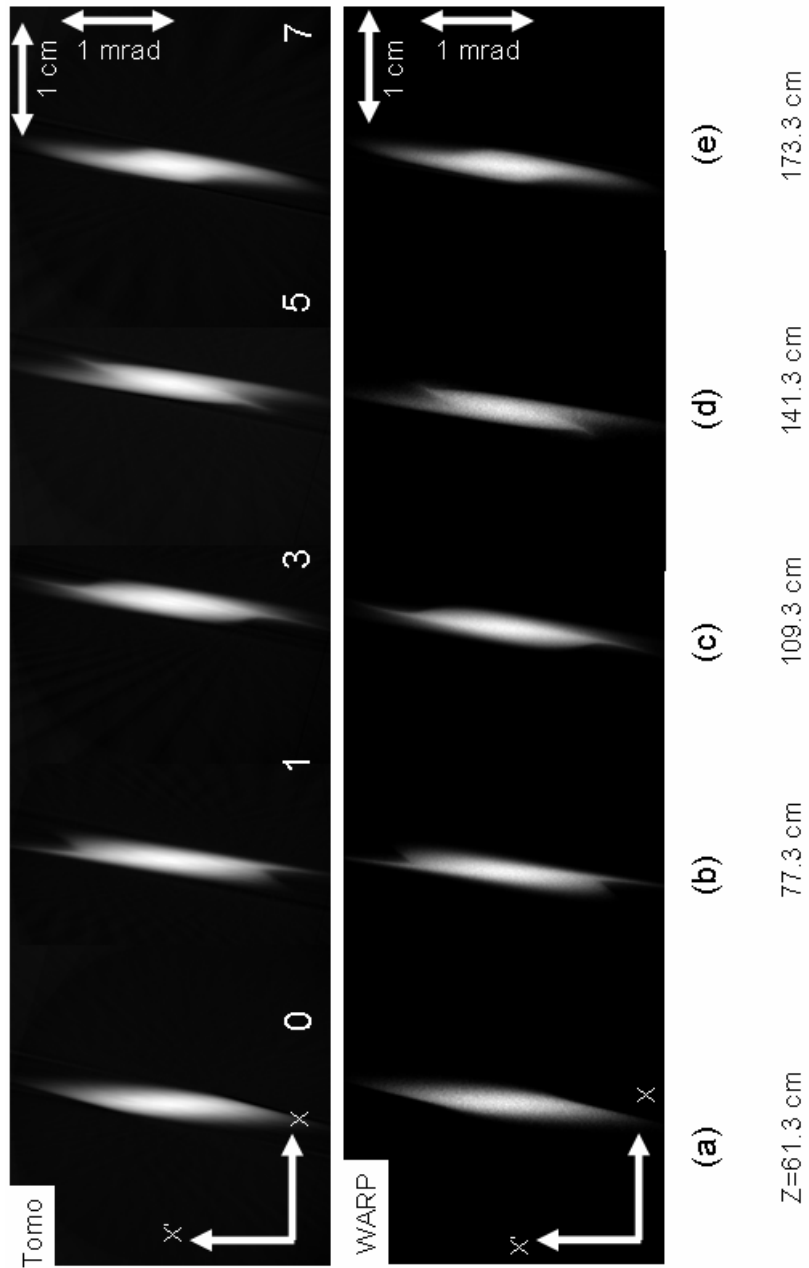


Figure 3.10: Phase space from simulations of the 7 mA beam after propagating for different distances, clearly indicating the propagation of transverse density waves: tomography (top) vs. direct WARP result (bottom) (cf. ref. [47]). Phase space after passing through (a) 0; (b) 1; (c) 3; (d) 5; and (e) 7 quadrupoles upstream of Q1. The symbol  $z$  indicates the total distance the beam has traveled.

### **3.6 Summary**

Using the particle-in-cell code WARP we have simulated a beam experiment and applied tomography techniques to map the phase space for beams in both emittance- and space charge-dominated regimes. For beams with space charge we are applying our tomography algorithm by assuming linear forces and no emittance growth. The validity of our reconstructed phase space was tested by comparing our results to the direct phase space generated by WARP (without tomography) which is highly accurate since it is not making the assumptions that our tomography algorithm does. For low current beams, we found excellent agreement between tomography and simulation. For more intense beams where space charge effects are present, still very good agreement exists, with the error close to 7%. Furthermore, we applied tomography for beams with different, more complex, particle distributions. We showed that by treating beams with non-uniform distributions as equivalent (in rms sense) to uniform beams we can obtain very accurate phase space maps. We are now ready to apply the diagnostic in the experiment.



## **Chapter 4 Tomographic Measurement of Phase-Space**

### **Evolution for Space-Charge Dominated Beams**

Many of the downstream propagation beam characteristics, such as beam emittance and brightness, can be strongly influenced from the upstream behavior [6], therefore a good understanding of the initial beam distribution and its evolution is important. Improved beam properties downstream have been reported by partitioning a single beam into smaller charge bunchlets right at the RF gun exit [49]. Additionally, experiments [30] and simulations [29] show that a multi-bunch approach to generate high-current intense beams offers a number of potential advantages over a single beam injector for Heavy Ion applications. Furthermore, experiments with multi-beamlet distributions have been recommended [31, 33] to mimic phenomenology inherent to time-dependent collective dynamics in galaxies such as colliding and merging galaxies [32]. Those examples illustrate the necessity of a good understanding of the evolution of multi-beamlet distributions.

Taking advantage of the intense beams and flexible design of UMER, in this chapter we apply our tomography diagnostic to a series of experiments to examine emittance growth, halo formation, phase mixing and charge homogenization. We use beams with different intensities and different transverse initial density distributions and compare our results with predictions from theory and simulations.

The outline of this chapter is as follows: In Sec. 4.1, we provide a short general description of UMER. In Sec. 4.2 we review the available UMER diagnostics. In Sec. 4.3, we describe the imaging hardware and software we used in the experiment. We also describe the process we use to automate the tomography process. Next, in Sec. 4.4 we cross check the phase spaces recovered by tomography in the experiment with phase spaces obtained with a different technique. In Sec. 4.5 we use tomography to describe the phase space evolution of intense, space charge dominated beams with initially uniform and nonuniform distributions and report some interesting physical insights. Finally, in Sec 4.6 we present a summary and conclusions.

## **4.1 University of Maryland Electron Ring (UMER)**

Experiments in this chapter are carried out on UMER [10, 11], a 10 keV nonrelativistic electron ring. Figure 4.1(a) shows the schematics of UMER and a list of UMER beam parameters is provided in Table 4.1. UMER is an 11.52 m-circumference ring that consists of 18 sections with four quadrupoles. Each ring section has two dipoles which provide two  $10^0$  bends. Three induction modules (one built and two more are under construction) will provide longitudinal focusing. At the injection of  $\beta = v/c = 0.2$ , the beam is nonrelativistic, implying it is highly sensitive to space charge forces. Beams are produced by an electron gun of Pierce geometry with a 4 mm radius cathode.

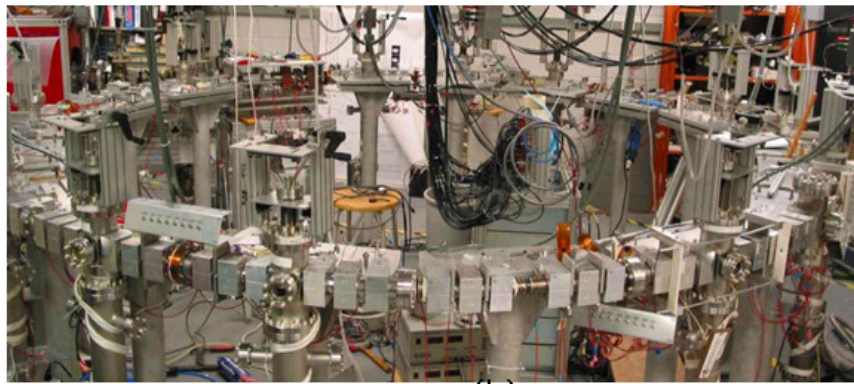
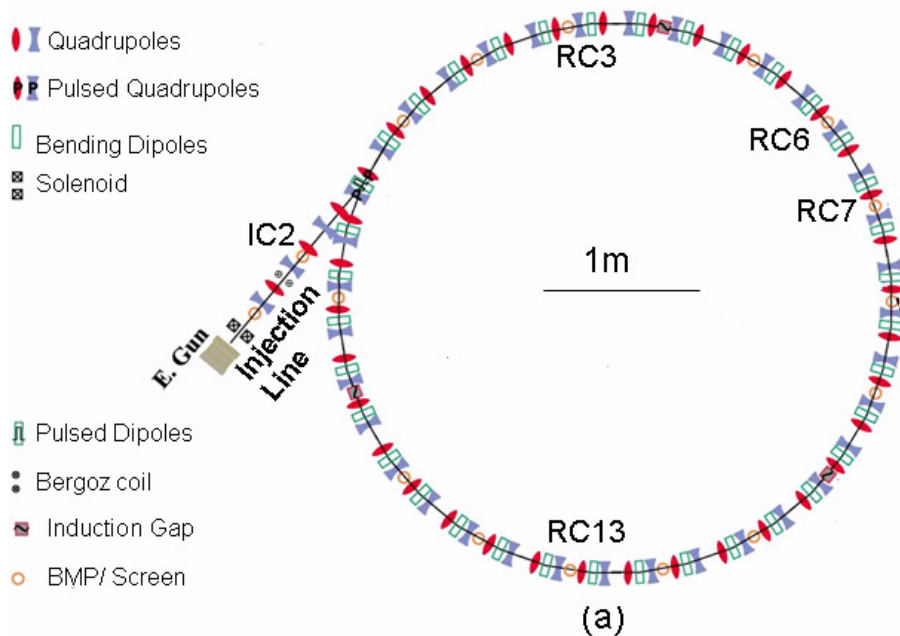


Figure 4.1: Layout of UMER: (a) Schematic representation; (b) Actual Photo

An adjustable Anode-Cathode gap enables us to vary the generalized perveance, and hence the strength of the space-charge forces. Furthermore, similar adjustments can be made by an aperture wheel right at the exit of the anode gun. The UMER aperture plate has 6 holes (apertures) in different sizes, including the full beam aperture and the five-beamlet mask and is shown in Fig. 4.2. The desired aperture can be selected by using the small rotary feedthrough (knob) next to the gun.

The size of each aperture and the resulting beam current are illustrated in Table 4.2. Table 4.2 includes also other beam parameters such as, the initial slope from the beam envelope  $r'_0$ , and beam emittance  $\varepsilon$ . Details about the calculation of those parameters are discussed in Sec. 4.4.

After passing through the mask and before entering the ring the beam passes a 1.4 m injection/matching section which employs one solenoid after the source and six quadrupoles. With a zero-current phase advance  $\sigma_0$  of  $76^\circ$  and lattice periodicity  $S$  of 0.32 m, UMER beams have a betatron oscillation wavelength  $\lambda_{\beta 0}$  equal to 1.51 m.

Table 4.1: UMER design parameters

Beam Energy	10 keV
$\beta = v/c$	0.2
Pulse Length	50-100 ns
Ring Circumference	11.52 m
Lap Time	197 ns
Pulse Repetition Rate	10-60 Hz
FODO Period	0.32 m
Zero-current Phase Advance, $\sigma_0$	$76^\circ$
Zero-current Betatron Tune, $\nu_0$	7.6
Tune Depression	$\geq 0.2$

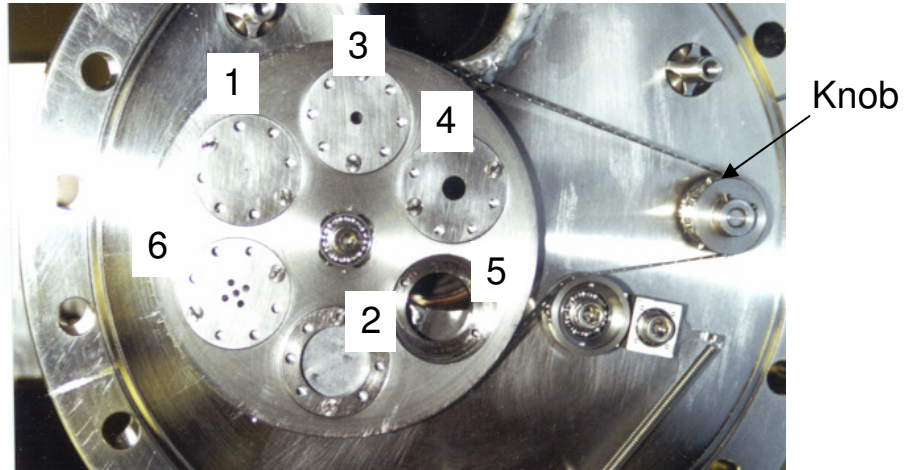


Figure 4.2: Aperture wheel at the gun exit. Note that there are six different apertures, each one resulting to a beam with different intensity.

Table 4.2: UMER Beam Parameters for the 10 keV beam.

Aperture #	$r_0$ (mm)	$I$ (mA)	$\varepsilon$ ( $\mu\text{m}$ )	$r_0'$ (mrad)	$r$ (mm)
1	0.25	0.7	7.6	-1.27	1.5
2	0.875	7	25.5	-4.3	3.19
3	1.5	23	39.0	-6.7	4.89
4	2.85	78	86.6 <sup>2</sup>	-	8.70
5	3.2	104	97.3 <sup>2</sup>	-	9.92
6	3.41 <sup>1</sup>	28	103.8 <sup>2</sup>	-	6.41

( $r_0$ : beam radius at the aperture;  $r$ : beam radius of a matched beam with  $\sigma_0 = 76^0$ ;  $\varepsilon$ :  $4xrms$ , unnormalized emittance;  $r_0' = 4 \langle r_0 r_0' \rangle / r_0$ : initial beam slope of the beam envelope)

<sup>1</sup>Estimated by using Eq. 3.3

<sup>2</sup>Obtained by scaling with the pencil beam (assuming a uniform beam).

By design, UMER provides a low-cost, well diagnosed research platform for investigating beam dynamics. In the next section we will briefly review the available ring diagnostics.

## **4.2 Available Diagnostics in the Experiment**

UMER has a number of available diagnostics that will be used in our experiment to carefully monitor the beam transport. Those are: A Bergoz coil for current measurement (see Sec. 4.2.1), Beam Position Monitors for current profiling and measurement (see. Sec 4.2.2) and Fluorescent Screens for measuring the transverse beam distribution (see Sec. 4.2.3). In the next subsections we will briefly review those diagnostics.

### **4.2.1 Bergoz Coil**

The beam current was diagnosed by using a Bergoz [50] fast current transformer located between the second and third quadrupoles in the injector section. The rise time of the Bergoz coil was measured to be 2.8 ns [51].

### **4.2.2 Beam Position Monitors**

All but four sections of the ring house diagnostic chambers consisting of a fast capacitive beam position monitors (BPMs) [51]. The monitors consist of four striplines with a  $77^\circ$  arc to decouple X and Y directions. Voltages measured along those striplines are been used to locate the beam centroid. In addition, those signals are been used for high resolution beam profiling, and current loss monitoring. BPMs have a very fast time response, which is about 1.7 ns.

### 4.2.3 Screens

Fluorescent screens are attached to the bottom plate of the BPM and provide information of the transverse beam distribution. Two additional screens are located along the injector line at diagnostic chambers: IC1 (31.1 cm from the aperture) and IC2 (81.98 cm from the aperture). The screens are based on P-43 phosphor ( $\text{Gd}_2\text{O}_2\text{S:Tb}$ ) which has peak emission on green (545 nm). The plane of the screen is 2.7 cm upstream from the chamber center and its diameter is 31.75 mm. The beam image is reflected by a mirror oriented at  $45^\circ$  to the beam line and monitored through a window in each chamber. This is illustrated in Fig. 4.3. One drawback of these screens is their response time, which is 1.6  $\mu\text{s}$  and hence they allow only to measure time-integrated beam profiles. In Chap. 6 we will review some new type phosphor screens, currently installed at the Long Solenoid Experiment, that have very fast response time ( $<3\text{ns}$ ) and so allow time-resolved measurements.

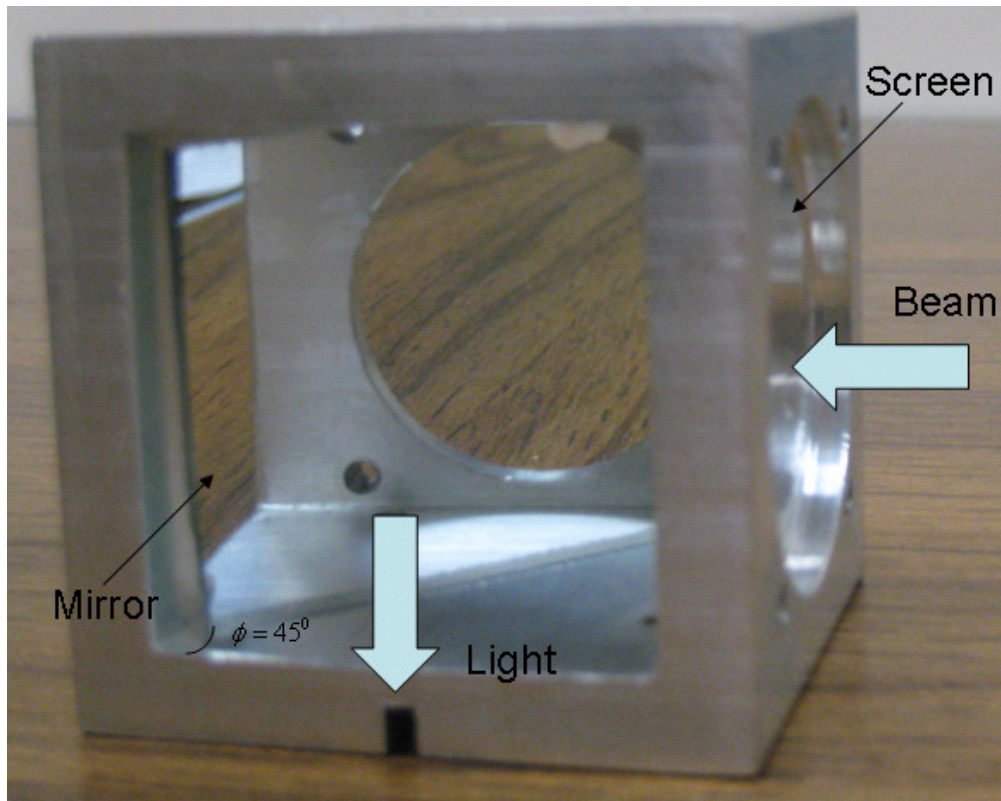


Figure 4.3: Screen assembly on UMER. Note that the mirror is at an angle  $\phi = 45^\circ$  to allow the light to come out from the window.

### 4.3 Image Acquisition and Processing

In this section we review the characteristics of the imaging system used in the experiments and provide details about the camera (Sec. 4.3.1), hardware control (Sec. 4.3.2) and image-acquisition software (Sec. 4.3.3). Finally, in Sec. 4.3.4 we discuss the procedure we use to automate tomography.



### 4.3.1 Camera and Lenses

An advanced, high resolution progressive scan, fully programmable digital charged coupled device (CCD) camera from IMPERX (model IPX-1M48-L) was used in our experiments. A CCD is a light-sensitive integrated circuit that stores irradiated image data in such a way that each acquired pixel is converted into an electrical charge. The camera uses an objective lens to focus the incoming light and if we place the CCD array at the focused point where this optical image is formed we can capture the image. The camera used in our experiments has a high resolution (1000x1000 pixels) in order to reveal as many details of the beam distribution as possible. Furthermore, it captures 8 to 12 bit images allowing so a high intensity range per pixel (see Sec. 2.4.3). The camera is equipped with an electronic shutter that is used to control the exposure time on the light sensor. Since the minimum exposure time for this camera is  $50 \mu s$  it is used only for time resolved measurements on UMER. The start of the exposure can be controlled through an external trigger. This allows the camera to be synchronized to an external timing pulse. Using the trigger option we synchronized the camera with the beam pulse so that the shutter was open when a beam pulse was fired and closed immediately after that (before the second pulse arrives). The camera receives the trigger signal coming through a connector located on the back of the camera. The maximum number of frames that can be captured are 30 frames/sec (camera read out time was 33 msec). Hence, in our experiments the beam frequency was reduced to 20Hz (50 msec time between pulses) to allow plenty of time for the camera to perform the read-out. More details about the

camera specifications and operating procedures for UMER can be found on Appendix B.

For our experiment we use a macro lens (AF Micro-NIKKOR 60mm f/2.8D). A macro lens is a lens with the ability to focus from infinity to extremely close distances (up to 0.22 m), allowing it to capture images of tiny objects in frame-filling, larger-than-life sizes. This is advantageous for our experiment for two main reasons: (1) It allows us placing the lens very close to the screen and so space is not a concern (up to 0.22m); (2) The lens provides high quality images since it cover the beam photo with a large number of pixels. To illustrate the second point we do a comparison of a macro lens with two other lenses and show our results in Fig. 4.4. As we can see the macro lens gives the best close-ups images. In our experiments we will exclusively use this lens.

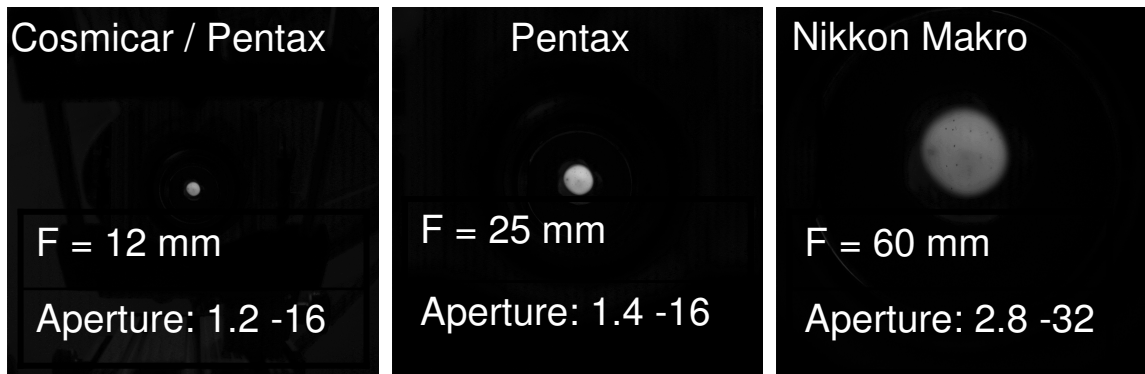


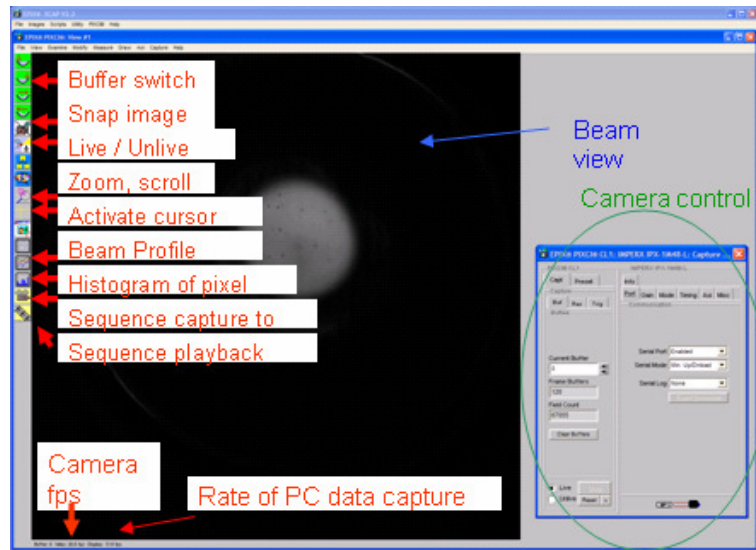
Figure 4.4: Images of the same beam with the same camera but different lenses. The aperture of a lens determines the amount of light that passes through the lens to the sensor. The focal length is noted as F. The macro lens (far right) allows the most close-up images.

### **4.3.2 Video Capture and Camera Control**

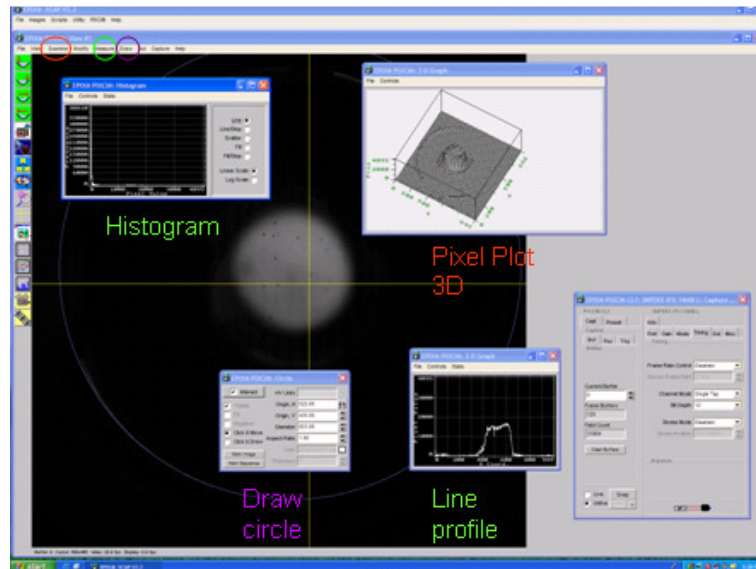
In order to connect the camera to the PCI Bus the PIXCI CL1 Camera Link linux compatible board from EPIX (model EPX-PIXCL1) is employed. The PIXCI CL1 operates in a 32 bit, 33MHz PCI bus slot and is able to transfer video data to the PCI bus up to 100 megabytes per second.

### **4.3.3 Image Acquisition Software**

The camera specifications (such as frame rate, triggering, electronic shutter etc) presented in Sec. 4.3.1 can be fully controlled by using XCAP-STD, from EPIX (model EPX-XCAPSTD-L). In our analysis we combine XCAP with Labview and use it exclusively for image acquisition and processing. Figure 4.5(a) and Fig. 4.5(b) illustrate the main features of XCAP.



(a)



(b)

Figure 4.5: Screen shots of the GUI of the XCAP imaging software; (a) Basic features; (b) Image processing tools

#### 4.3.4 Tomography Automation

As discussed in earlier chapters, in order to successfully reconstruct the phase space we have to take a large number of beam photos (sometimes as high as 200). Therefore, by combining Labview and XCAP we fully automated the tomography process enabling a full scan without human intervention in less than 30 minutes. We will briefly review the automation in this section and provide a more detailed description in Appendix C.

The schematic layout of our computer control system is illustrated in Fig. 4.6. One computer under linux is used to control the magnets by using Labview and a second computer, under windows is used to control the camera. The automation process works as follows: Labview is activated from the linux computer (step 1). Labview sets the desired magnet values (step 2) and then notifies via text message (step 3) the windows computer to activate XCAP (step 4). XCAP acquires a beam image and saves the beam photo (steps 5), then sends an acknowledgement message back to the linux computer (step 3). This process continues until the whole quadrupole scan process is over. Finally, we post-process these photos, using the same MATLAB scripts described in Chap. 2 for simulated photos (see Sec. 2.4.4), recovering thus the phase space distribution (step 6).

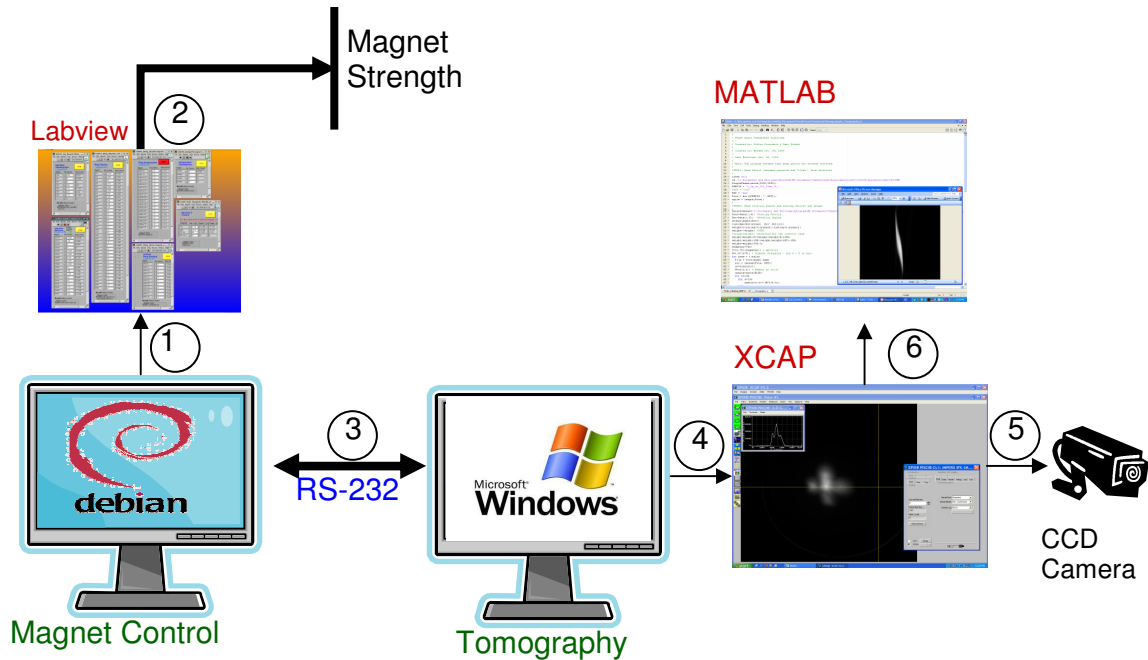


Figure 4.6: Diagram of the UMER Tomography control system structure

## 4.4 Beam Characterization near the UMER source – Tomography

### Verification

In Chap. 3 in order to check the validity of the assumptions made by tomography we simulated the reconstruction process. Our results showed good agreement between the phase spaces from tomography and direct simulation. Now we are interested in comparing the tomography phase spaces reconstructed in the experiment to that generated by using a different diagnostic, known as the *pinhole scan*. In Sec. 4.4.1 we review the principles of the pinhole scan diagnostic and show our results, and in Sec 4.4.2 we compare them with tomography. We do our

measurements on UMER and in all cases the beam energy is set at 10 keV and the pulse length is 100 ns with a repetition rate of 20 Hz.

#### **4.4.1 Pinhole Scan**

Here we will demonstrate an alternative method to obtain phase spaces. One potential advantage of this method is that it can provide us with phase space maps right at the gun exit and therefore we can get information of the beam initial conditions such as the beam emittance, size and slope of the beam envelope. This way we can optimize beam injection.

As discussed in Sec. 4.1 the UMER aperture plate has 6 holes (apertures), where the desired aperture can be selected by using the small rotary feedthrough (knob) next to the gun (see Fig. 4.2). The smallest available aperture, the pinhole (aperture 1 in Fig. 4.2), can be used to make an estimate of the beam emittance and transverse beam phase space. Due to the small radius of the pinhole (0.25 mm), the beam coming out is emittance dominated. Therefore, the particles move along straight lines between the aperture and screen. The principle of the process is schematically shown in Fig. 4.7 and works as follows: By turning the knob for a few degrees we can move the pinhole vertically (same  $x$ , different  $y$ ) and sample different parts of the full beam behind the pinhole. Then, by using the screen (IC1), 28.4 cm downstream, we can record the position of the beamlet each time. The concept is very similar to that of a pepper-pot, however, the advantage of a pinhole scan is that you have only one hole so there is no concern about overlapping beamlets.

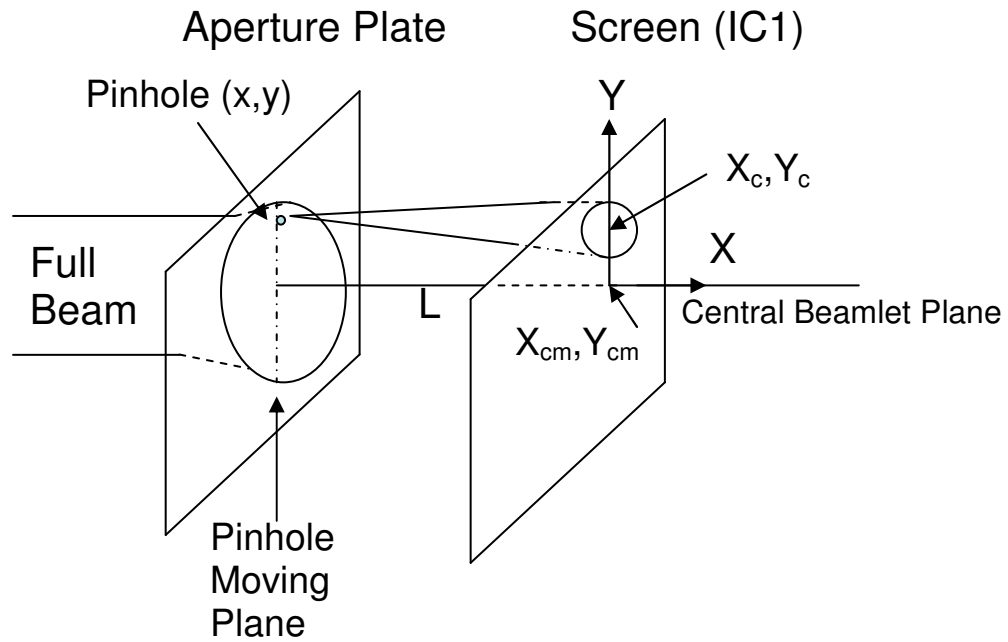


Figure 4.7: Schematic representation of the principle of the pinhole scan.

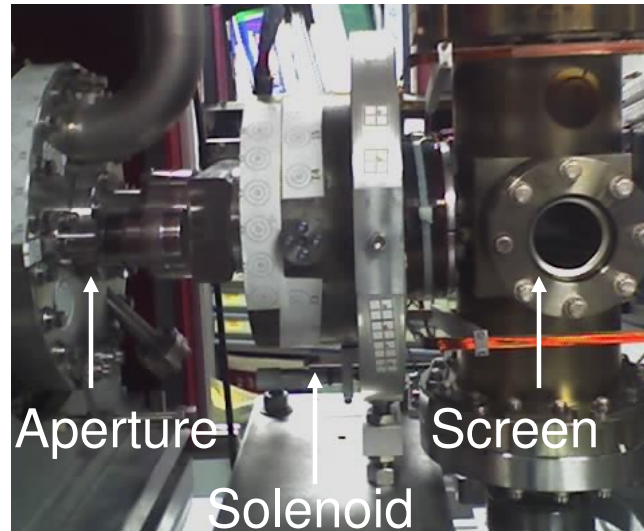


Figure 4.8: Actual photo indicating the aperture and the screen. Note that solenoid was turned off for the pinhole scan.

Figure 4.9 shows several pictures of individual beamlets at IC1 for different positions of the pinhole. The label  $y$  shows the position of the pinhole and the number



at bottom shows the position of the rotary feedthrough in degrees. The beamlets appear to be cut for settings below  $188^\circ$  and higher than  $224^\circ$ . Additionally, the beam completely disappears when the knob is at  $168^\circ$  and  $244^\circ$  for a total scan of  $76^\circ$ . Previous calibration tests show that a rotation of  $1^\circ$  on the knob scale corresponds to a linear transition of the mask center close to 0.1 mm. Thus, the radius of the full beam must be close to 3.8 mm. We assume that the central beamlet falls at the middle of this angular span ( $206^\circ$ ). It is interesting to note that beamlets are hollow, indicating a hollow velocity space. This is in agreement with previous experiments and simulations [44, 46], and as described in Sec. 3.4.2 is caused by the distortion of the potential near the cathode by the (cathode) grid. Another interesting observation is that the pinhole photos show a shadow of the anode grid pattern.

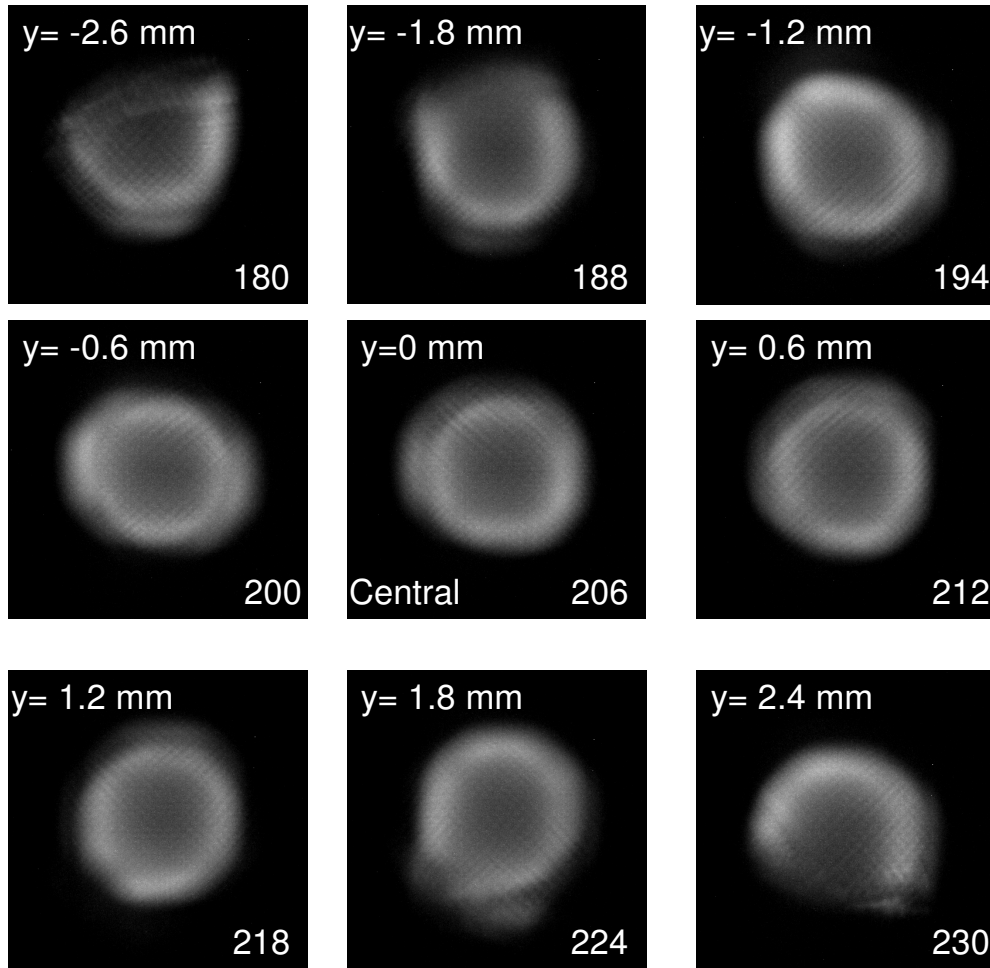


Figure 4.9: Photos of individual beamlets for different positions of the pinhole. The top number shows the position of the pinhole relevant to the central beamlet. The bottom number shows the position of the knob. The bias voltage in the experiment was set at 30 V and typical beam radii of the beamlets on the screen are 6 mm.

Suppose that  $L$  is the distance between the planes of the aperture and the screen and  $X_{cm}, Y_{cm}$  are the  $x, y$  centroids of the central beamlet. Then, an estimate of the beam divergence  $y'$  can be made at the aperture by recording the centroids  $X_c, Y_c$  of each of the individual beamlets at the screen. If the pinhole aperture is set at a

point  $(x, y)$  relative to the central aperture, then the beam divergence  $y'$  with respect to the central axis is given by:

$$y' = \frac{(Y_c - Y_{cm}) - y}{L}. \quad (4.1)$$

Thus, the beamlet centroids are a direct measure of the angular distribution of the beam sampled at  $(x, y)$ . Therefore, applying Eq. (4.1) for each beamlet we can obtain an “averaged” phase space distribution at the location of the aperture.

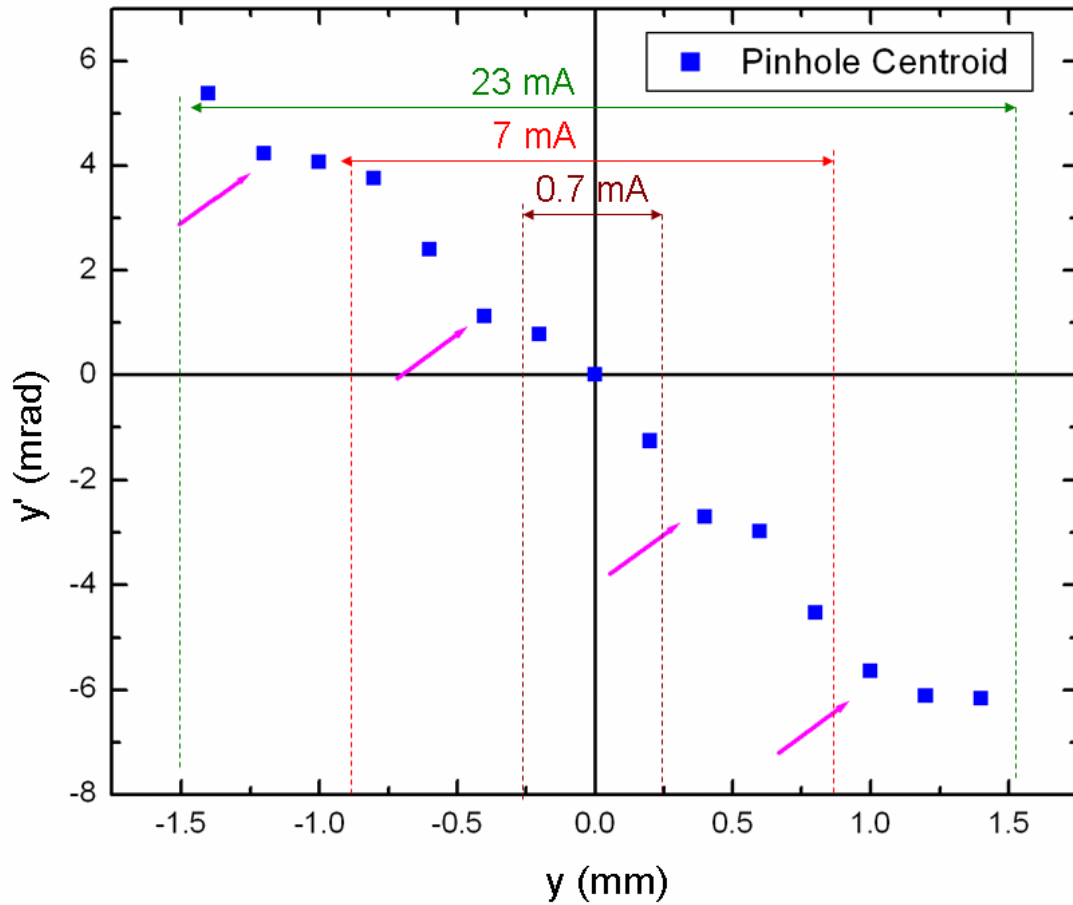


Figure 4.10: Averaged phase space distribution at the beam aperture obtained from the pinhole scan. The vertical lines show the range of three UMER beams: 0.7 mA, 7 mA, and 23 mA.

Care must be taken so that data will be collected for as small vertical movements of the pinhole as possible. However, to sample different parts on phase space this movements cannot be less the pinhole scan radius. In our experiments we selected to move the pinhole at  $2^0$  (=0.2mm) steps and our results are illustrated in Fig. 4.10. It is worth to mention that the points follow a harmonic line. Four major modulations are shown which are indicated by the magenta color arrow. The period of these modulations is very similar to the gun's anode grid wire spacing (0.69mm). Hence, the anode grid modulates some density photos and so is altering the centroid location and this affects the final phase space measurement.

From the pinhole scan measurements we can make an estimate of the beam  $4 \times rms$  emittance by applying the formula (see Sec. 1.1.2)

$$\varepsilon_y = 4\sqrt{\langle y^2 \rangle \langle y'^2 \rangle - \langle yy' \rangle^2}, \quad (4.2)$$

which can be further modified to

$$\varepsilon = \sqrt{(r_0 r'_p)^2 - (r_0^2 \tan \phi)^2} \quad (4.3)$$

where  $r_0 = 2\sqrt{\langle y^2 \rangle}$  is the  $2 \times rms$  size at the aperture (see Table 4.2);

$r'_p = 2\sqrt{\langle y'^2 \rangle}$  is  $2 \times rms$  slope that can be estimated from the size of each beamlet on the screen; and

$$\tan \phi = -\frac{\langle yy' \rangle}{\langle y^2 \rangle} \quad (4.4)$$

is the slope of the phase-space [7], a quantity that can be calculated from the slope of the line that passes through the points in Fig. 4.10. In Table 4.3. we record all values

for  $r_0, r_p'$  and  $\tan \phi$ . Since our pinhole measurements are up to 1.4 mm in the vertical direction (the pinholes are cut after this point), we can make an estimate of the phase space slope,  $\tan \phi$ , only for the first three UMER beams. The range of those beams is illustrated in Fig. 4.10 and the obtained emittances from Eq. 4.3 are listed in Table 4.1.

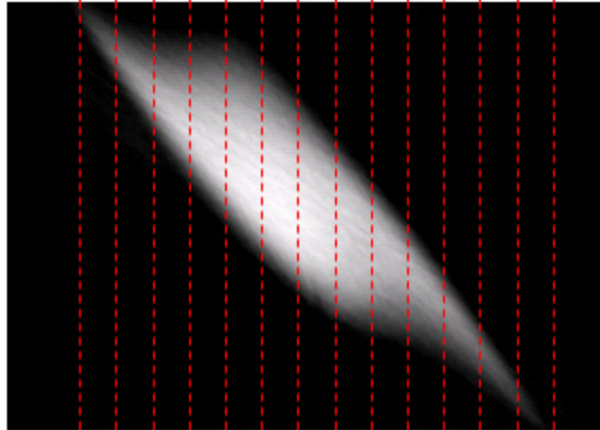
Table 4.3: Beam parameters from the pinhole scan

$I$ (mA)	$\tan \phi$ (mrad / mm)	$r_0$ (mm)	$r_p'$ (mrad)
0.7	-5.1	0.25	-30.6
7	-4.9	0.875	-29.4
23	-4.5	1.5	-26.8

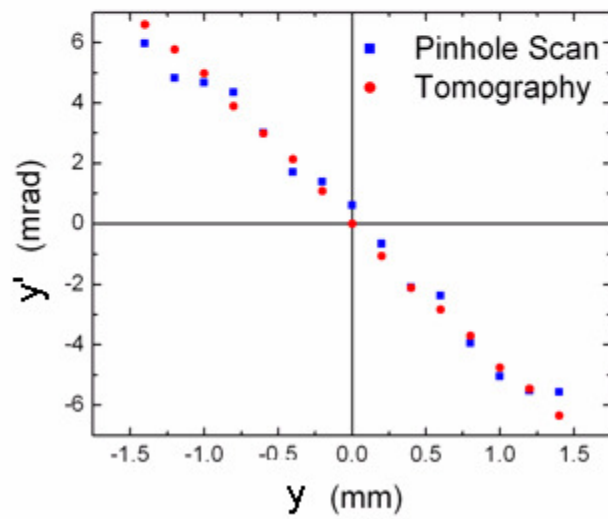
#### 4.4.2 Phase Space at the Aperture by Tomography

In this section we like to compare the pinhole scan phase space to the one we get from tomography. We focus our work on the 23 mA beam current with generalized Perveance,  $K$ , equal to  $3.4 \times 10^{-4}$ . To generate such a beam current we set the aperture hole at position 5 in Fig. 4.2. As Fig. 4.8 illustrates the solenoid magnet between the aperture and the screen was turned off while collecting the pinhole photos. According to the discussion in Chap. 5 scanning the solenoid, can produce phase space maps, similarly to quadrupoles.

For tomography, the solenoid field has incrementally increased from 4.0 A up to 12.2 A resulting to 42 independent projections at the screen that was used to reconstruct the phase space at the aperture plane according the discussion in Chap. 2 and Chap. 5. This phase space is shown in Fig. 4.11(a).



(a)



(b)

Figure 4.11: (a) Phase space for the 23mA beam at the aperture plane generated by: (a) Solenoidal Tomography; (b) Pinhole Scan (blue dots). Red lines are locations where the beam centroid along  $y$  is calculated (red dots).

Once, we have reconstructed the phase space at the aperture we are interested in comparing it to that obtained from the pinhole scan. To do so, we calculate the centroids from the tomography phase space along the same  $y$ 's to that of the pinhole scan. Therefore, we calculate the centroids along the red lines in Fig. 4.11(a) and the resulting values are plotted in Fig. 4.11(b). For comparison, on this plot we include also the centroids calculated from the pinhole scan (blue points) in the previous section.

From Fig. 4.11(b) we can see that the agreement between tomography and pinhole scan is very good. The only difference is the absence of the four modulations that are visible in the pinhole scan case. We believe this is because the tomography

phase space,  $yy'$ , is the result of the integral:  $\mu(y, y') = \int_{-\infty}^{\infty} \int_{-\infty}^{\infty} \mu(x, x', y, y') dx' dx$  (see

also Eq. 2.23) and therefore we have to integrate over all  $x$ . In contrast the plot from the pinhole scan correspond to the case where  $x$  is limited within the pinhole diameter range ( $-0.25 \text{ mm} < x < 0.25 \text{ mm}$ ) (since the pinhole could move only along the  $y$  direction). Therefore, this infinite integration in tomography is averaging out the other transverse direction ( $x$  direction) causing the “wash-out” of those modulations that were clearly seen in the pinhole scan case.

## 4.5 Evolution of intense space-charge beams on UMER

In this section we are interested in describing the phase space evolution of beams with intense space charge along a single turn on UMER. We will address issues related to transverse nonlinear particle dynamics such as emittance growth,

phase-space mixing and halo formation. The following discussion emphasizes on experiments with two beams which have similar intensities but very different beam distributions; one initially uniform in configuration space (see Sec 4.5.2) and one with a highly non-uniform (see Sec. 4.5.3) distribution. Before describing the experiments we briefly review the magnet configuration (see Sec. 4.5.1). It should be noted that experiments conducted within this section were done before replacing the gun's old cathode to the one we used for the pinhole scan in Sec. 4.4. Therefore, the initial beam conditions are not the same with the one shown in Table 4.2.

#### **4.5.1 Tomography Configuration and Phase Space Reconstruction**

As illustrated in Sec. 4.1 UMER has 18 sections that consist of 4 quadrupoles (2 FODO's), 2 dipoles for horizontal steering and one dipole for vertical steering. The tomography configuration employs one of these sections and is illustrated in Fig. 4.12. The four quadrupoles were labeled as Q1, Q2, Q3, and Q4. The reasoning for using four quadrupoles is: (1) to rotate the phase space distribution by  $180^{\circ}$ , while (2) keep the beam size in a reasonable range when it travels through the pipe in order to avoid particle losses or image-charge effects, and (3) to maintain the beam size contained within the fluorescent screen. When the quadrupoles are scanned, the phosphor screen displays the transverse current density (integrated over many pulses). The beam pictures are captured by the CCD camera described in Sec. 4.3.1 and stored. Each distribution is then projected into x and y axes in order to tomographically reconstruct the  $xx'$  and  $yy'$  phase spaces according to the discussion in Chap. 2, respectively. The beam phase space is projected at the screen location



following the discussion in Sec. 2.4.2, so that distributions in both spatial and phase space can be compared at the same plane.

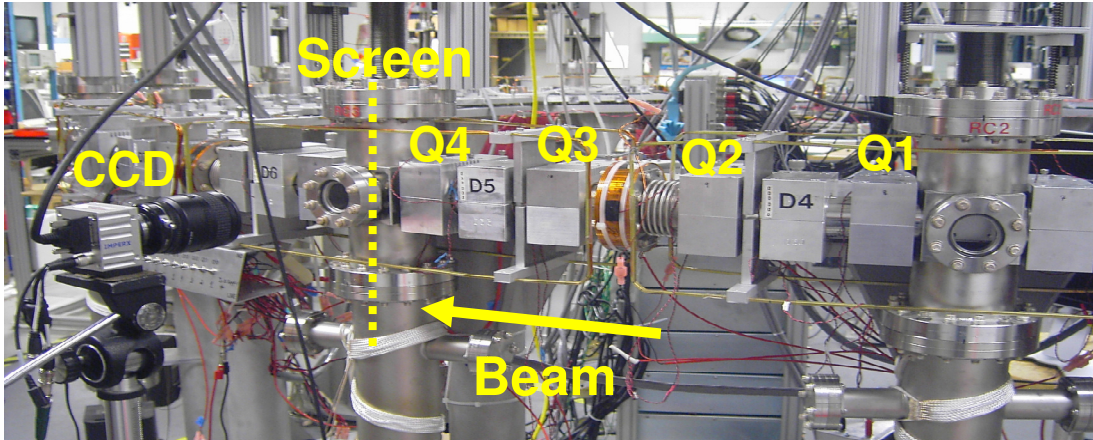


Figure 4.12: Tomography experimental configuration on UMER.

To reveal more details about the phase space distribution, instead of showing  $x'$  versus  $x$  plots, we show  $x' - x \tan \varphi$  versus  $x$ , where  $\tan \varphi$  is the phase-space slope [7] defined by Eq. 4.4. In other words, for each  $x'$  we do the transformation  $x' \rightarrow x' - x \tan \varphi$ . An example of this transformation is illustrated in Fig. 4.13. In the rest of the chapter, we use this format to plot our distributions.

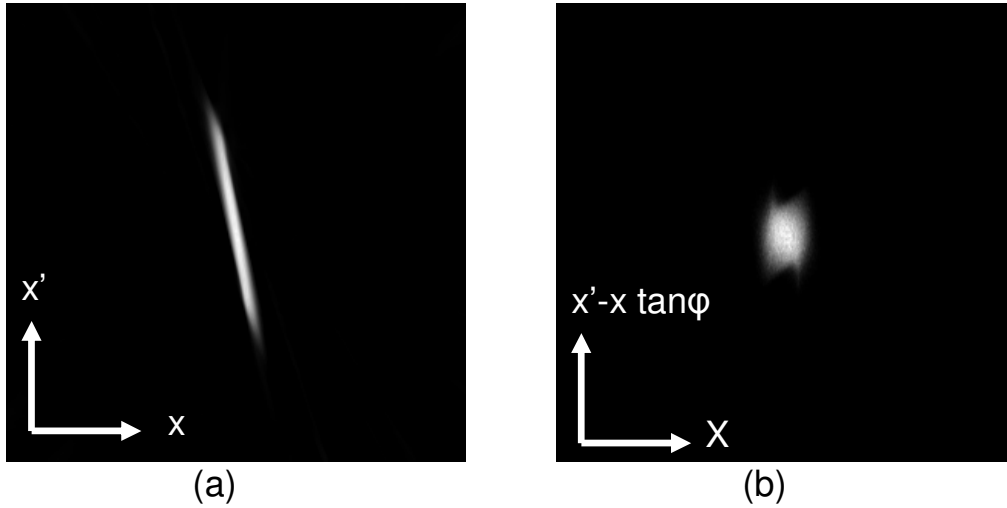


Figure 4.13: Phase space transformation example: (a)  $x'$  vs.  $x$  phase space; (b) same phase space but after the transformation  $x' \rightarrow x' - x \tan \phi$ , where  $\tan \phi$  was  $-5.6$  mrad/mm.

#### 4.5.2 Phase Space Evolution of a Uniform Beam on UMER

By setting the aperture plate at the 1.5 mm radius hole (see Fig. 4.2) we generate an intense beam and observe its evolution for up to a single turn on UMER. The purpose of this experiment is to study the influence of space-charge forces on the phase space evolution. In the experiment, initial beam parameters are 10 keV in energy, 19mA in current resulting to a generalized perveance  $K$  of  $2.8 \times 10^{-4}$ . The pulse length is 100 ns with a repetition rate of 20Hz. The beam is space-charge dominated, and the intensity parameter,  $\chi$ , is equal to 0.85. Using Eq. 2.13 we find that the depressed betatron period is equal to  $\lambda_{\beta} = 4.84$  m and the plasma wavelength is  $\lambda_p = 1.14$  m.

Figure 4.14(a)-top (and Fig. 4.15(a)-top) illustrates a phosphor screen image of the beam distribution in configuration space along the UMER injector line at a distance equal to  $z=0.76$  m from the aperture (at IC2). Figure 4.14(a)-bottom (Fig. 4.15(a)-bottom) shows the tomographically reconstructed  $xx'$  ( $yy'$ ) phase-space at the same location. The measured  $4\times rms$  emittance from this phase space is  $44.5 \mu m$  and  $47.7 \mu m$  for the  $xx'$  and  $yy'$ , respectively [52]. Assuming a uniform configuration space distribution at the aperture plate, we estimate the emittance to be  $28.2\pm 9 \mu m$  by scaling from the full beam (the radius and the emittance are 3.2 mm,  $60\pm 20 \mu m$  for the full beam). The reasoning for the higher emittance measured by tomography could be due the appearance of a halo, clearly visible in Fig. 4.14(a). This argument was justified by running gun simulations which traced back the halo to the cathode [53].

Next, we want to compare our experiment with simulation by running the WARP code. Simulations are initialized at the aperture and the output from each run is processed into an image similar to that a phosphor screen would observe. We use a  $512\times 512$  grid for the Poisson solver, a step size of 2 mm along  $z$ , and 640,000 particles. Running a large number of test simulations with more particles or higher resolution resulted in no perceptible difference in the final result. The beam at the aperture was modeled by a semi-Gaussian distribution (see Sec. 3.4.1). Figure 4.14(b)-top corresponds to the configuration space. Figure 4.14(b)-bottom (Fig. 4.15(b)-bottom) shows the tomographically reconstructed  $xx'$  ( $yy'$ ) phase space at the same location. Interestingly, the simulation is not showing the halo in

configuration space. This result is another indication that the halo is generated directly from the gun.

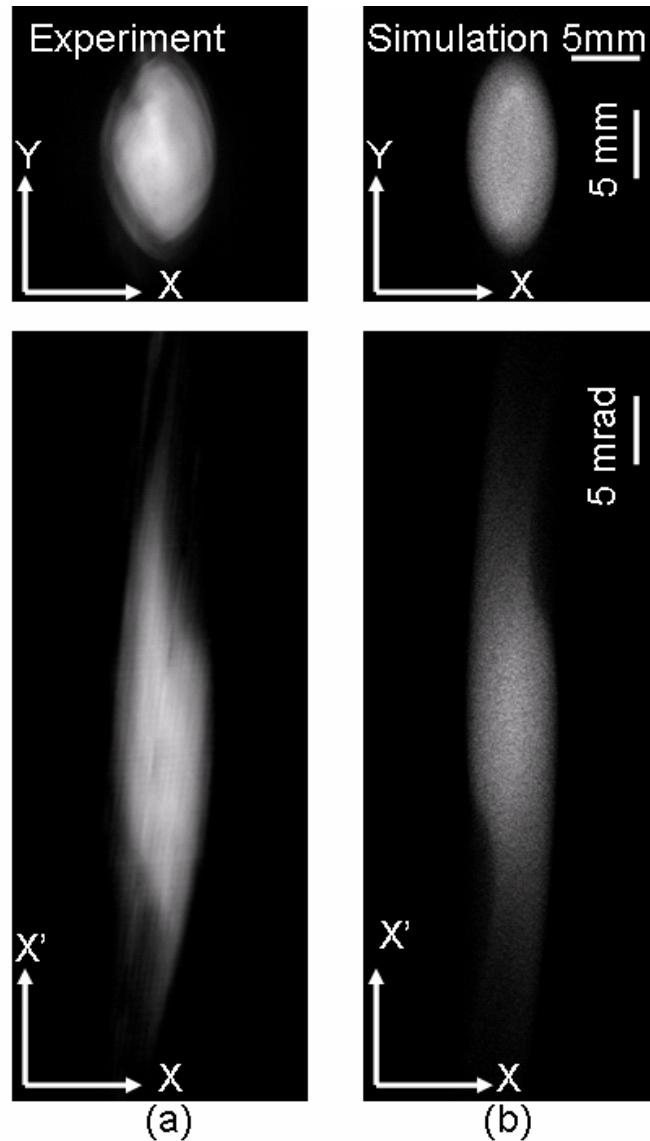


Figure 4.14: Beam distribution in configuration space (top) and  $XX'$  phase-space (bottom) 76 cm from the beam aperture: (a) Experiment; (b) WARP simulation . The subtracted slope (in units of mrad/mm) is 3.03. Clearly, a halo in configuration space is visible in the experiment.

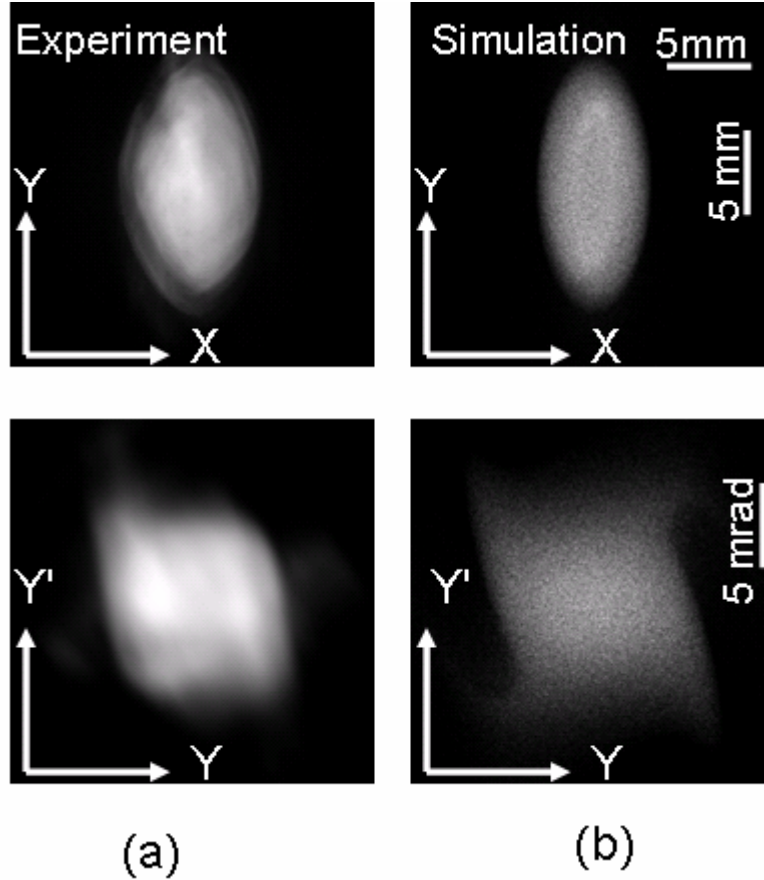


Figure 4.15: Beam distribution in configuration space (top) and  $YY'$  phase-space (bottom) 76 cm from the beam aperture: (a) Experiment; (b) WARP simulation. The subtracted slope (in units of  $\text{mrad}/\text{mm}$ ) is 4.77. Clearly, a halo in configuration space is visible in the experiment.

Figure 4.16 indicates fluorescent screen pictures from the experiment (top) and tomographically reconstructed  $xx'$  phase space distributions (bottom) at various locations along the UMER ring. Figure 4.17 shows the reconstructed by tomography  $yy'$  phase-spaces at the same locations. The label at the top of the photos depicts the

distance from the aperture as well as the corresponding diagnostic chamber on UMER.

The measured distributions indicate the presence of halo in configuration space at all chambers. The halo however, changes orientation in configuration space. For instance in RC3 and RC13 it's visible mostly in the y plane, but in RC6 it appears only in the x plane. In RC7 and RC9 it is visible in both planes. Note that tomography has successfully image the presence of halo particles in phase space. As expected the halo in  $xx'$  phase space is intense when the halo is in the horizontal in configuration space (for instance, RC6) but becomes weak in RC3 (because halo is in the vertical plane only).

The capture of halo is a big success for the diagnostic. Halos are in general difficult to detect since their low intensity. Intercepting diagnostics such as a pepper pot or slit scan can sample only parts of the beam, reducing so the intensity even more and making the detection of halos more harder.

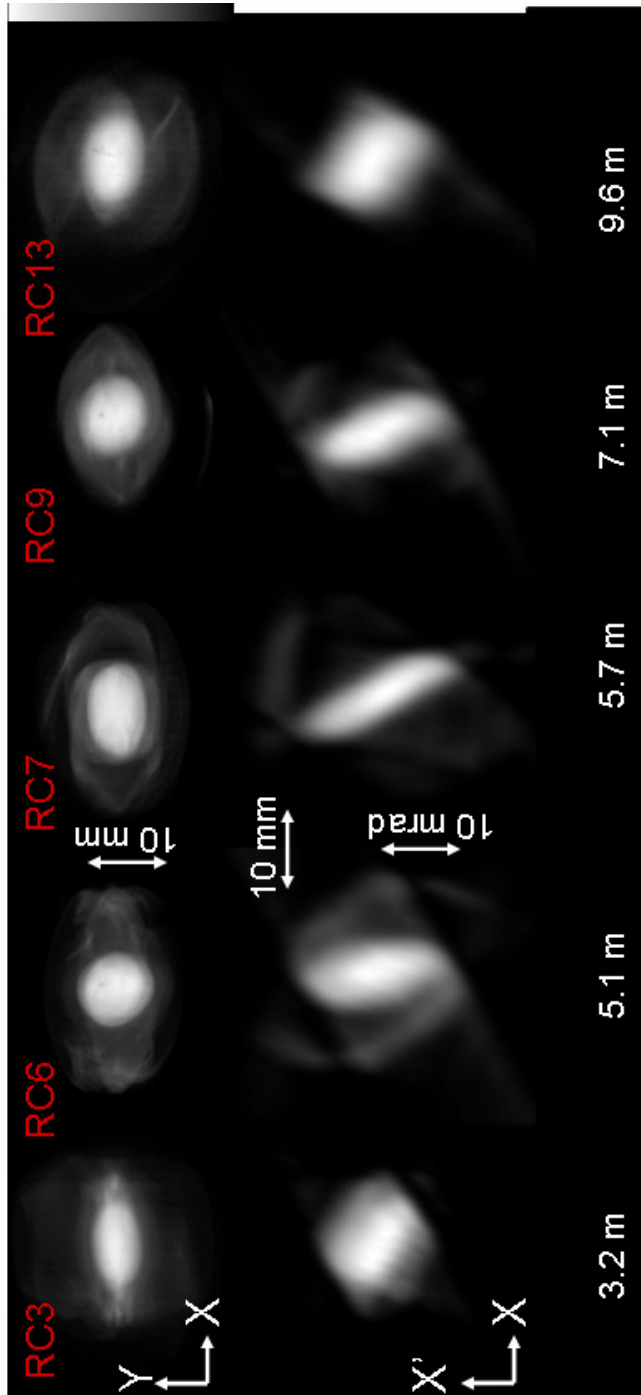


Figure 4.16: Beam evolution along UMER in configuration space (top) and  $XX'$  phase space (bottom). The 4xrms emittances (in  $\mu\text{m}$ ) and subtracted slopes (mrad/mm) are 32.7, 3.22 (RC3); 70.0, 2.96 (RC6); 71.5, 3.36 (RC7); 50.0, 3.07 (RC9); and 42.7, 3.22 (RC13), respectively.

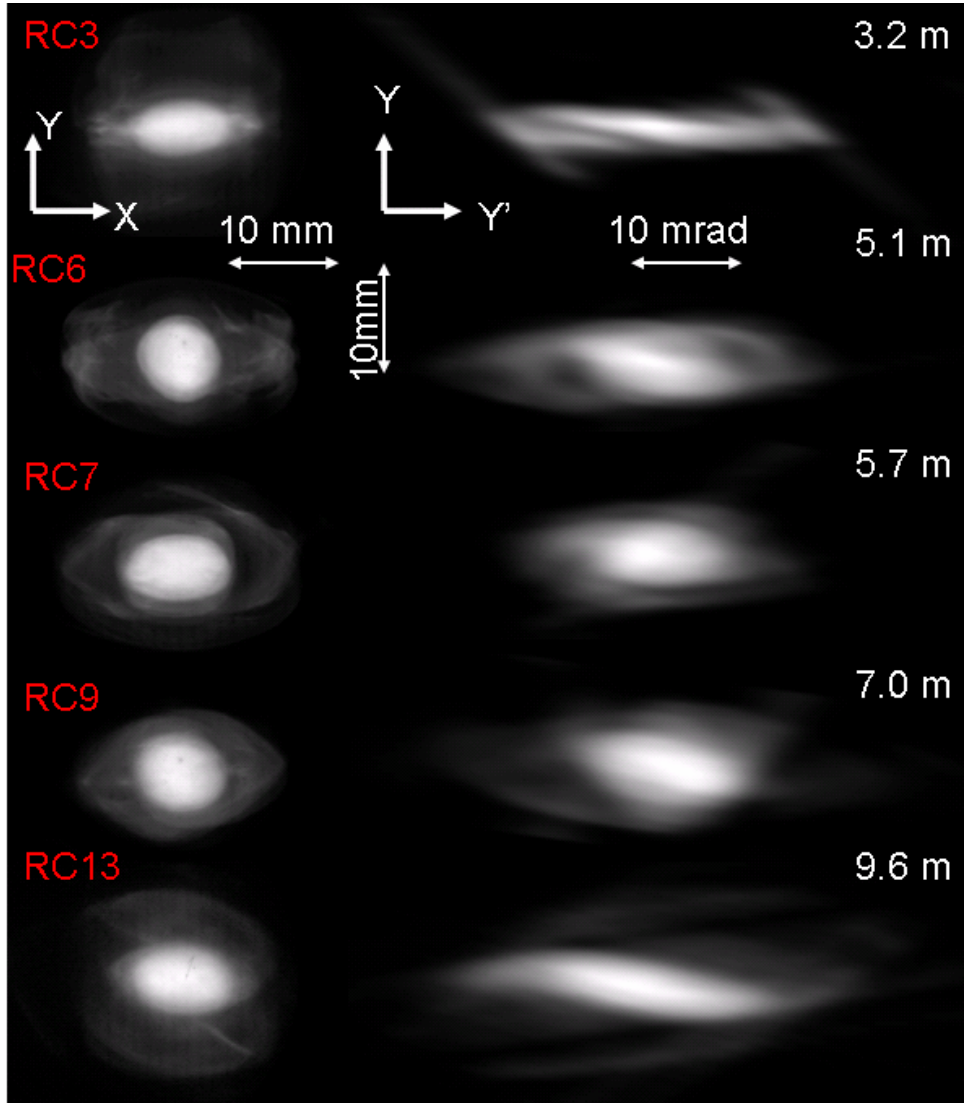


Figure 4.17: Beam evolution at different locations along UMER in configuration space (top) and  $YY'$  phase space (bottom). The 4xrms emittances (in  $\mu\text{m}$ ) and subtracted slopes (in  $\text{mrad}/\text{mm}$ ) are: 42.5, -6.70 (RC3); 52.6, -5.71 (RC6); 43.6, -5.71 (RC7); 54.3, -7.24 (RC9); and 96.8, -7.25 (RC13), respectively.



### 4.5.3 Phase Space Evolution of a Nonuniform Beam on UMER

In this section we examine for the first time both experimentally and numerically phase space mixing of high-current, low energy beams. Taking advantage of the number of available diagnostics and flexible design of UMER we study the beam evolution over a long range of distance. Using an asymmetric aperture we generate a pattern of five merging beamlets and we show that whereas the beamlets appear to be merged in configuration space they remain distinct in velocity space  $\approx 0.76$  m downstream from the source. Numeric simulation confirms this behavior at that location. Tomographic emittance measurements on that location reveal an emittance growth of 1.1 which is in agreement with the theoretically predicted growth due to the conversion of the field energy to thermal kinetic energy [54]. Beyond this point particles in phase space appear to lose memory of their initial conditions and density modulations are visible in phase space for several plasma periods. After about 7 plasma periods a more “uniform-like” beam is seen in both configuration and phase space.

To generate an initial inhomogeneous current distribution consisting of five beamlets we set the aperture wheel in Figure 4.2 at position 6. Figure 4.18 is a schematic illustration of that beam mask showing also the relevant distances (not drawn to scale). In the experiment, initial beam parameters are 10 keV in energy, 28 mA in current resulting in a generalized Perveance,  $K$ , of  $4.2 \times 10^{-4}$  and an  $4 \times rms$  unnormalized emittance of  $\epsilon_i = 80 \mu m$ . The equivalent in rms sense uniform beam radius at the aperture can be found from Eq. (3.3) and is

$$r_u = \sqrt{r_{let}^2 + 1.6\delta^2} = 3.41 \text{ mm.} \quad (4.5)$$

The emittances and currents of each beamlet according to Eq. 3.4 and Eq. 3.5 are  $20.4 \mu\text{m}$  and  $5.6 \text{ mA}$ , respectively. The pulse length is  $100 \text{ ns}$  with a repetition rate of  $20 \text{ Hz}$ . The intensity parameter  $\chi$  is equal to  $0.70$ , so the beam is space charge dominated, resulting to a depressed betatron period of  $\lambda_\beta = 2.75 \text{ m}$  and plasma wavelength equal to  $\lambda_p = 1.3 \text{ m}$ .

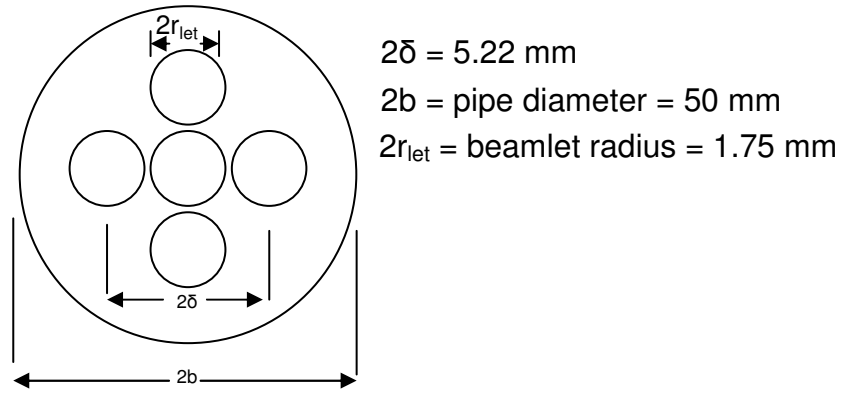


Figure 4.18: Schematic layout of the UMER five beamlet mask. Note that  $r_{let}$  and  $b$  are the beamlet and UMER pipe radius, respectively. Distances are not drawn to scale.

Figure 4.19(a) (top) illustrates a phosphor screen image of the beam distribution in configuration space along the UMER injector line at a distance equal to  $z \approx 0.76 \text{ m}$  from the aperture (IC2). Figure 4.19(a) (bottom) shows the tomographically reconstructed  $xx'$  phase space at the same location. An interesting experimental observation is that even though the structure of the original beamlet configuration is faintly visible in configuration space, the beamlets are well separated in phase space. Such a result indicates that the beam retains some coherence since a

large group of particles maintain information about their origin. This explains the reappearance of the initial distribution in configuration space that was observed in previous experiments [7, 54, 55] several plasma periods downstream.

Measuring the beam emittance from the reconstructed phase space reveals an emittance growth of 1.1 in IC2 (relevant to the aperture). According to the free energy theory [7], emittance growth can occur by the conversion of the excess field energy of a nonuniform beam into transverse thermal energy. According to that model the emittance growth can be written as [7]:

$$\frac{\epsilon_f}{\epsilon_i} = \left(1 + \frac{KR^2}{2\epsilon_i^2} \frac{U}{w_0}\right)^{1/2}, \quad (4.6)$$

where  $K$  is the generalized Perveance defined in Eq. 2.9;  $R$  is the effective matched beam radius;  $\epsilon_i$  and  $\epsilon_f$  are the initial and final four-time rms emittances and  $U/w_0$  is a dimensionless quantity that depends on the shape of initial nonuniform distribution and for our case is equal to -0.2659. Using the smooth approximation [7] the effective radius can be written as

$$R = (\epsilon_i S / \sigma_0)^{1/2} [u + (1 + u^2)^{1/2}]^{1/2}, \quad (4.7)$$

where  $u = KS / 2\sigma_0\epsilon_i$ . For our experimental parameters the matched beam radius is 5.98 mm. Therefore, Eq (4.6) predicts an emittance increase by a factor of 1.1, which is in excellent agreement with the growth predicted by tomography in IC2.

Figure 4.19(b) corresponds to the configuration space (top) and phase space (bottom) obtained directly by the WARP simulation. Simulations were initialized at the aperture. The simulation shows beamlets that are partial merged in real space and

still distinct in phase space a result that is consistent with the experiment. Additionally, in agreement with the experiment, WARP also predicts an emittance growth of 1.1 relevant to the aperture.

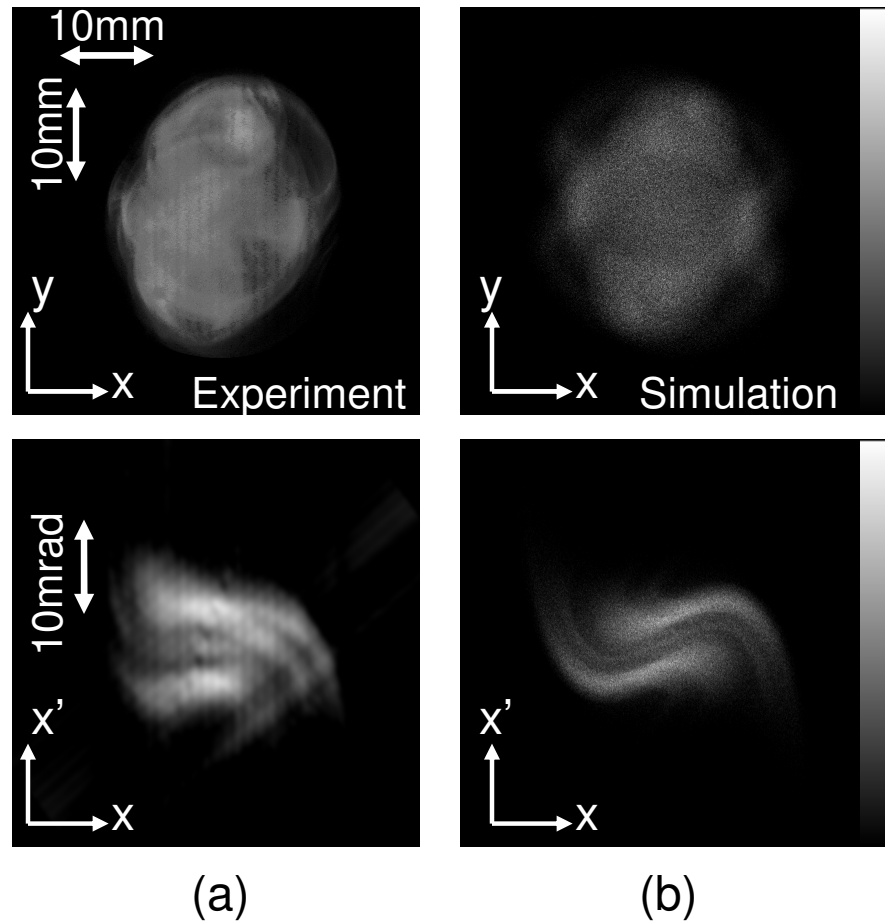


Figure 4.19: Merger of the 5 beamlets at IC2. Configuration space (top) and  $xx'$  phase space (bottom) from: (a) experiment; (b) WARP simulation. The subtracted slope (in units of mrad/mm) is -1.40.

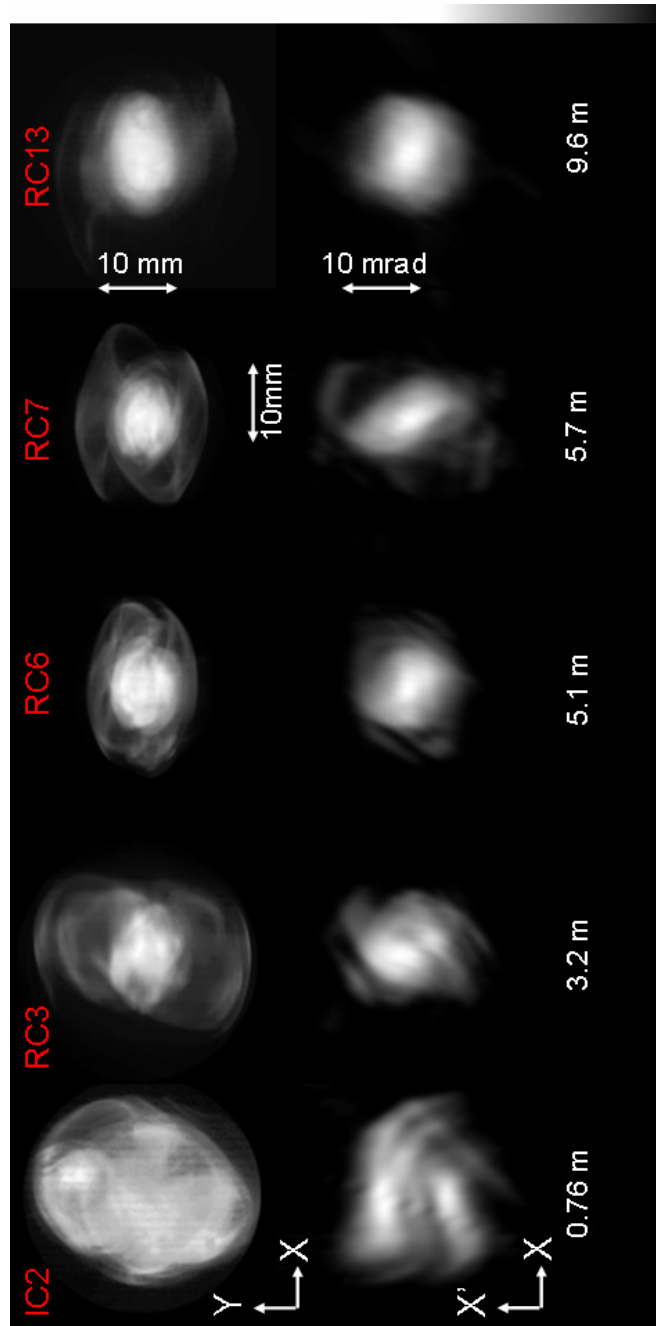


Figure 4.20: Five-beamlet evolution at different locations along the UMER ring in configuration space (top) and  $XX'$  phase space (bottom). The subtracted slope (in units of  $\text{mrad}/\text{mm}$ ) are 3.08 (RC3), 3.00 (RC6), 3.53 (RC7), and 3.84 (RC13).

Figure 4.20 shows fluorescent screen pictures taken in the experiment (top) and tomographically reconstructed  $xx'$  phase spaces (bottom) at various locations along the UMER ring. Figure 4.21 shows the reconstructed  $yy'$  phase spaces at the same locations. The labels on each photo depict the distance from the aperture as well as the corresponding diagnostic chamber on UMER. The images indicate that the beam core retains an intricate dynamical structure over the first five plasma periods. However at a distance of about seven plasma periods the beamlets completely lose memory of the initial conditions and the core becomes more uniform-like in both configuration space and phase space. Given that the characteristic time scale for interparticle collisions in UMER corresponds to 1,000 plasma periods [33] this fast relaxation to equilibrium cannot be associated with interparticle collisions but is rather generated by the influence of the non-linear space charge forces.

Of particular interest is the appearance of halo at RC3, approximately 2.4 plasma periods that persists for the remaining length of the focusing channel. The final state of the beam at RC13 consists of a homogenized core and a halo apparent in both configuration space and phase space.

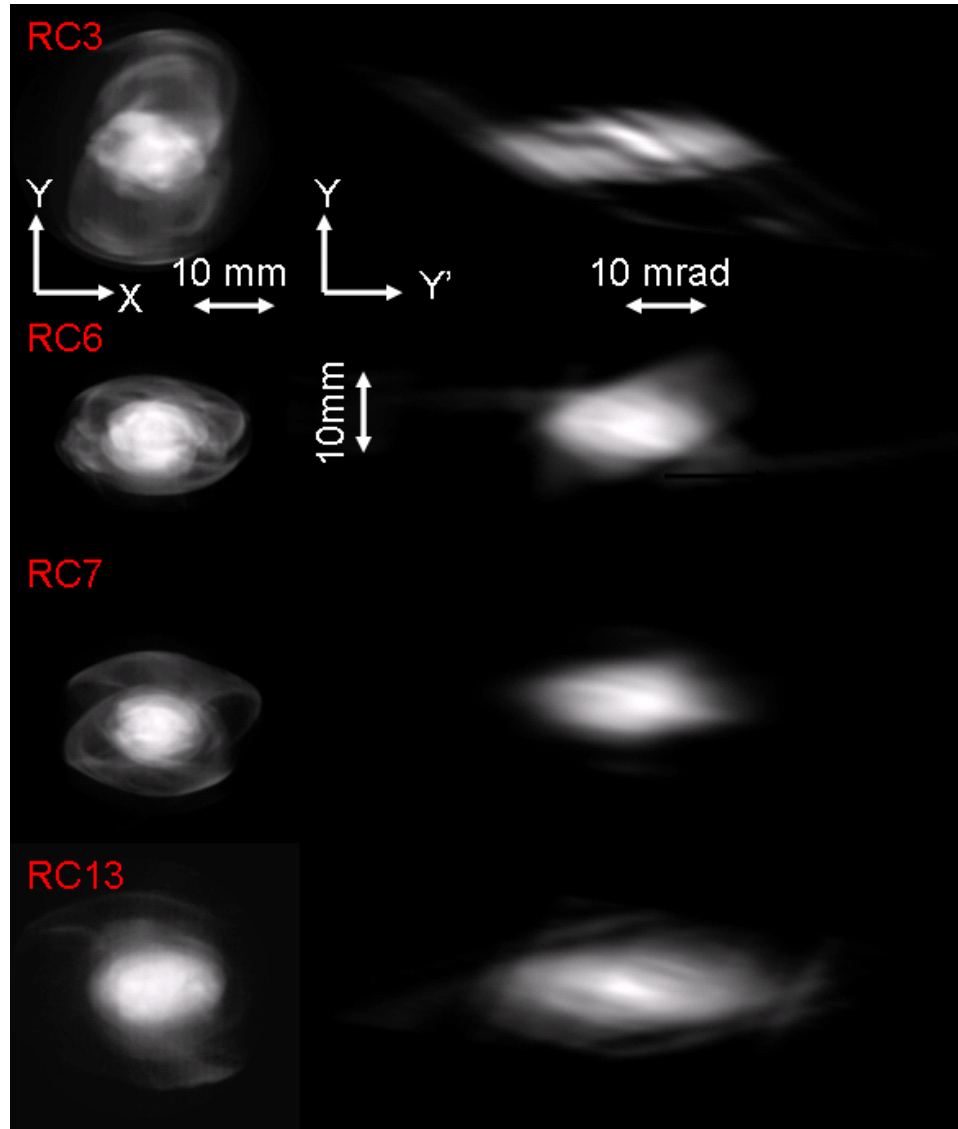


Figure 4.21: Five-beamlet evolution at different locations along the UMER ring in configuration space (top) and  $YY'$  phase space (bottom). The subtracted slope (in units of mrad/mm) is -4.51 (RC3), -1.36 (RC6), -6.46 (RC7), and -5.90 (RC13).

As discussed in Sec. 4.5.2 a potential source of halo in our experiments is due the imperfection of the gun geometry. Furthermore, previous experiments with five-beamlet distributions showed that a small mismatch of the beam can create a

substantial amount of halo, downstream. We have evidence of such mismatch was occurring in our experiment, caused primarily due to the no proper function of some UMER quadrupoles. This was later revealed by carefully testing the UMER quadrupoles [56]. Therefore, we conclude that the appearance of halo in our experiment is partly due to the gun imperfections and partly due mismatches.

## **4.6 Summary**

In this chapter, we presented the imaging hardware, acquisition and processing system for UMER. Using this configuration we studied the transport of beams with initial uniform distributions and examined the influence of space-charge force on their phase-space evolution. Beam halo was visible on the fluorescent screen images. Tomography revealed the appearance of halo particles in phase space as well and provided an understanding of the dynamics of halo evolution in phase-space. Next, using an asymmetric aperture we have generated a nonuniform pattern of five merging beamlets and examined their evolution in a periodic quadrupole channel. Close to the aperture the beamlets were observed to merge in configuration space, however were well distinct in phase space. The emittance growth at that location agrees well with the theoretical prediction and is associated with the thermalization of free energy. Further downstream, the beam was losing coherence and significant phase space mixing occurred.



## Chapter 5 Solenoidal Tomography

In the previous chapters we showed that tomographic techniques using quadrupole lenses can be useful for reconstructing phase space distributions. We achieved this by using multiple configuration space images of the beam at different phase space rotation angles through  $180^0$ . One drawback of using quadrupoles is that they defocus the beam in one direction and hence, the desire to achieve the  $180^0$  phase space rotation inevitably leads to large asymmetric beams and nonlinearities that can compromise the results. Therefore, because solenoids provide symmetric focusing, they have the potential to be superior to quadrupoles for tomography. In this chapter, we extend the technique to use solenoids and show that accurate reconstruction of phase space can be accomplished with fewer solenoids and fewer projections than is the case with tomography based on quadrupole focusing. This diagnostic can therefore be very useful for electron photoinjectors [26] which use solenoids near the gun but also for low-energy machines [28] that use solenoids to transport high space-charge beams. Solenoidal Tomography [57] can measure the phase space in the machines referred to above, providing crucial information that can be used to optimize the injection, transport and acceleration of higher-quality beams downstream.

The outline of this chapter is as follows. In Sec 5.1 we review the physics regarding the particle motion in solenoidal systems, define the transport matrix and relate it to tomography. In Sec. 5.2 we simulate the technique using the particle-in-cell code, WARP to ascertain the accuracy of the reconstruction. In Sec. 5.3 we describe the experimental apparatus. In Sec 5.4 we show our experimental results and

compare them with simulations. Finally, in Sec 5.5 we summarize our results and derive our conclusions.

## 5.1 Principles of Solenoidal Tomography

In this section we review the equations of motion of particles within solenoids and show how solenoids can be used to do tomography. First, we limit our discussion by assuming no space charge (Sec. 5.1.1), and then we generalize for cases with space-charge (Sec. 5.1.2).

### 5.1.1 Particle motion in Solenoidal Systems

The longitudinal magnetic field produced by a solenoid has long been used for ion and electron beam focusing. Compared with a quadrupole doublet of the same performance, the power dissipation and peak fields needed in a solenoid is much higher so that the use of solenoids is restricted to low momentum beams. It is used extensively in image intensifiers, electron microscopes, and electron accelerators. In this section we briefly review the equations of motion for a particle undergoing solenoidal focusing and show how they can be implemented to our tomography diagnostic in order to reconstruct the beam phase space.

Assuming a magnetic solenoid and an axisymmetric system, the field components  $B_r$  and  $B_z$  off axis are obtained from  $B(z)$  and its derivatives by [7]

$$B_z(r, z) = B(z) - \frac{r^2}{4} \frac{\partial^2 B(z)}{\partial z^2} + \dots, \quad (5.1)$$

$$B_r(r, z) = -\frac{r}{2} \frac{\partial B(z)}{\partial z} + \frac{r^3}{16} \frac{\partial^3 B(z)}{\partial z^3} - \dots. \quad (5.2)$$

In the paraxial limit, where the particles have small transverse velocity  $v_r, v_\theta \ll v_z$  we can consider only the first-order terms in the above expansions of the fields and therefore the off-axis field components become:

$$B_z(r, z) \cong B(z), \quad (5.3)$$

$$B_r(r, z) \cong -\frac{r}{2} \frac{\partial B(z)}{\partial z}. \quad (5.4)$$

Particles enter the lens through a region of radial magnetic fields resulting in an azimuthal Lorentz force ( $ev_z \times B_r$ ). Therefore they gain angular velocity which is given by:

$$\dot{\theta} = -\frac{qB}{2m\gamma} + \frac{p_\theta}{\gamma mr^2}. \quad (5.5)$$

Equation (5.5) describes the change in azimuthal position of the particles as a function of distance  $z$  and implies that the particle distribution is rotated as the beam passes through the solenoid. For systems with cylindrical symmetry, the canonical angular momentum is a constant of particle motion:

$$p_\theta = \gamma mr^2 \dot{\theta} + qrA_\theta \quad (5.6)$$

a fact known as Busch's theorem [7,16]. It implies that particles gain no net azimuthal velocity if they pass completely through the lens. This is because they must cross negatively directed radial magnetic field lines at the exit that cancel out the azimuthal velocity gained at the entrance. Following a number of mathematical steps [7], it is possible to show that the axial variation of the envelope of a cylindrical beam is given by:

$$r'' + \frac{\gamma'}{\gamma\beta^2} r' + \frac{\gamma''}{2\gamma\beta^2} r + \left( \frac{qB}{2mc\beta\gamma} \right)^2 r - \frac{p_\theta^2}{m^2 c^2 \gamma^2 \beta^2 r^3} = 0. \quad (5.7)$$

This equation describes the radial motion of the particles near z-axis where the nonlinear force terms and space-charge terms can be neglected. The second and third terms are due acceleration and electric field focusing or defocusing, respectively. Assuming that we have a magnetic solenoid and there is no acceleration, Eq. (5.7) can be reduced to:

$$r'' + \left( \frac{qB}{2mc\beta\gamma} \right)^2 r - \frac{p_\theta^2}{m^2 c^2 \gamma^2 \beta^2 r^3} = 0. \quad (5.8)$$

It is often convenient to study the particle trajectories in a frame that rotates at the Larmor frequency  $\omega_L$  and is therefore known as the *Larmor frame*. The angle between this rotating frame and the stationary laboratory system is given by [7]:

$$\theta_r = -\int_{z_0}^z \frac{qB}{2\beta\gamma mc} dz = \mp \int \frac{\omega_L}{\beta c} dz. \quad (5.9)$$

The angle of the particle in the Larmor frame is given by the difference between the angle  $\theta$  in the laboratory frame and  $\theta_r$ :

$$\theta_L = \int_{z_0}^z \frac{p_\theta dz}{\beta\gamma m c r^2} + \theta_0. \quad (5.10)$$

Of particular interest is the situation when the particles are launched with zero angular velocity in a region with no magnetic fields, in which case, according to Eq. 5.6 the canonical angular momentum is zero. Then, the nonlinear term in Eq. 5.8 drops to zero and becomes now

$$r'' + \kappa_0(z)r = 0, \quad (5.11)$$

where

$$\kappa_0(z) = \omega_L^2 / \beta^2 c^2 = \left( qB / 2m\beta\gamma c \right)^2 \quad (5.12)$$

and is known as the focusing function of the solenoid magnet. Therefore, when the particles are launched with zero angular velocity in a region with no magnetic fields we can see from Eq. 5.11 that the transverse particle motion in the Larmor frame becomes harmonic in a plane through the axis. Solutions of Eq. 5.11 may be represented in the following form

$$\begin{pmatrix} r \\ r' \end{pmatrix} = \begin{pmatrix} \cos[\sqrt{\kappa_0(z)}\delta] & \frac{1}{\sqrt{\kappa_0(z)}} \sin[\sqrt{\kappa_0(z)}\delta] \\ -\sqrt{\kappa_0(z)} \sin[\sqrt{\kappa_0(z)}\delta] & \cos[\sqrt{\kappa_0(z)}\delta] \end{pmatrix} \begin{pmatrix} r_0 \\ r'_0 \end{pmatrix} = T \begin{pmatrix} r_0 \\ r'_0 \end{pmatrix}, \quad (5.13)$$

where  $\delta$  is the length of the solenoid and T is the beam solenoidal transport matrix. A comparison of Eq. 5.13 to Eqs. 2.4 and 2.5 suggests that the solenoid transport matrix in the Larmor frame is like that of a magnetic quadrupole, except for the difference in the expression for  $\kappa_0$ . Therefore, when  $p_\theta = 0$ , solenoids like quadrupoles can be used to rotate the phase space distribution. Hence, the procedure for phase space reconstruction is identical to the case with quadrupoles (see Sec. 2.2.2). For beams with non-zero initial angular momentum the presence of the nonlinear term in the particle motion equation makes the analysis more complicated and is beyond the scope of this dissertation.

### 5.1.2 Solenoidal Tomography for Beams with Space-Charge

Tomography for space charge dominated beams has been extensively studied in Chap 2 (see Sec. 2.3). We showed that a linear space charge approximation can successfully reconstruct the beam phase space even for beams with very high intensity. Since particles traveling within solenoids (in the Larmor frame) obey the same equations of motion like quadrupoles, the analysis for space-charge dominated beams in solenoids is identical to the one described in Sec. 2.3. Hence, by assuming linear forces in the solenoid case, using Eqs. 2.38 and 2.39 the net focusing functions become

$$\kappa_x(z) = \kappa_{x0}(z) - \frac{2K}{X(z)(X(z)+Y(z))}, \quad (5.14)$$

$$\kappa_y(z) = \kappa_{y0}(z) - \frac{2K}{Y(z)(X(z)+Y(z))}. \quad (5.15)$$

Solenoids provide symmetric focusing ( $B_x = B_y$ ), therefore  $\kappa_{x0}(z) = \kappa_{y0}(z) = \kappa_0(z)$  (given by Eq. 5.12) and the beam stays round ( $X(z) = Y(z) = R(z)$ ). Therefore, the net focusing function becomes

$$\kappa(z) = \kappa_0(z) - \frac{K}{R(z)^2}, \quad (5.16)$$

and the solenoid transport matrix of Eq. 5.13 becomes now

$$T = \begin{pmatrix} \cos \left[ \sqrt{\kappa_0(z) - \frac{K}{R(z)^2}} \delta \right] & \frac{1}{\sqrt{\kappa_0(z) - \frac{K}{R(z)^2}}} \sin \left[ \sqrt{\kappa_0(z) - \frac{K}{R(z)^2}} \delta \right] \\ -\sqrt{\kappa_0(z) - \frac{K}{R(z)^2}} \sin \left[ \sqrt{\kappa_0(z) - \frac{K}{R(z)^2}} \delta \right] & \cos \left[ \sqrt{\kappa_0(z) - \frac{K}{R(z)^2}} \delta \right] \end{pmatrix} \quad (5.17)$$

The beam radius,  $R(z)$ , will be calculated from the beam envelope Eqs 2.40 and 2.41, which by assuming symmetric focusing and  $\varepsilon_x = \varepsilon_y$ , become

$$R(z)'' + \kappa_0(z)R(z) - \frac{K}{R(z)} - \frac{\varepsilon^2}{R(z)^3} = 0. \quad (5.18)$$

In order to solve Eq. 5.18 some assumptions about the beam initial conditions and beam distribution at the starting point  $z_0$  is required. Similarly to quadrupoles, we check the accuracy of the initial conditions by comparing the actual beam sizes at a downstream location,  $z_1$ , to the predicted from Eq. 5.18. If they do not agree well we adjust the initial conditions until a good agreement is achieved. Once  $R(z)$  is known we can calculate the transport matrix and do the tomography as in the quadrupole case. Analytically the process is as follows:

1. Estimate the initial conditions at the starting location  $z_0$
2. Identify the correct initial conditions at  $z_0$  : For each magnet setting, solve Eq. 5.18 and compare the calculated beam size to that from the measurement. If the two values are not within 10%, estimate new initial conditions and repeat the process until good agreement is achieved.
3. For each setting solve numerically the envelope equation, and get  $R(z)$  along the beam line at 0.4 mm minimum steps.
4. Use Eq. 5.16 to obtain the focusing strengths and then use Eq. 5.17 to calculate the transport matrix for each step. Finally, obtain the total transport matrix by multiplying those matrices. Now follow the steps 2-5 as described in Sec. 2.2.2

5. Change the magnet focusing and repeat steps 3-4.

At the end of the scan integrate the filtered projections,  $Q$ , over the rotation angle by using Eq. 2.19.

## 5.2 Simulation and Validation of Solenoidal Tomography

In order to validate the reconstruction approach, we have simulated the tomography process using the 2 ½ D version of WARP, which advances particles in a transverse slice under the impact of external forces and self-consistent self-fields. Two solenoids, S1 and S2, have been employed for the reconstruction and the layout is demonstrated in Fig. 5.1. The center of S1 relative to  $z_0$  is  $L_1=13.0$  cm, center to center distance of the solenoids is  $L_2=16.5$  cm and the screen is placed at  $L_3=13.5$  cm relative to the center of solenoid S2. The magnet geometry, solenoidal field profiles and beam parameters used in the simulation are those from the Long Solenoid Experiment (LSE) [57].

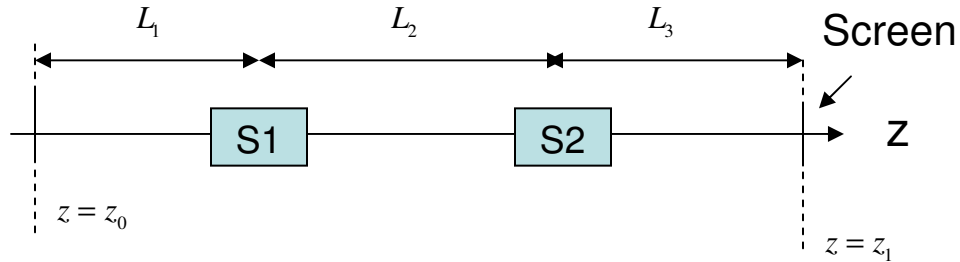


Figure 5.1: Schematic layout of the solenoidal tomography configuration. S1 and S2 are the two solenoids that we scan to get the projections. Simulation is initialized at  $z_0$  and the phase space is reconstructed at  $z_1$ . The geometry of the configuration is similar to the LSE.



We run 48 WARP simulations corresponding to the solenoid setting used later in the experiment and collect the beam photos at  $z_1$  with similar procedure to that described in Chap 3 for the case of quadrupoles. WARP models the solenoids as a grid of magnetic field data obtained by fitting an analytical formula to experimental measurements of the field on axis and then calculating the off-axis fields using a 5<sup>th</sup> order Taylor expansion. Magnet nonlinearities, including those arising from fringe fields are fully incorporated. Nonlinear space charge forces as well as image forces are included. Simulations are initialized at the aperture.

The output from each run is processed into an image similar to that a phosphor screen would observe. In a similar fashion with that described in Chap. 3 we apply the tomography algorithm to these photos and compare the reconstructed phase space to the phase space obtained directly from the WARP simulation. This process allows us to verify the fidelity of the solenoidal tomographic technique since our tomography algorithm does not include nonlinear effects from magnets or space charge. Therefore, the WARP simulations can be used to check the effect of these nonlinearities in given situations.

In Sec. 5.2.1 we will simulate the tomography process for uniform beam distributions and in Sec. 5.2.2 we will generalize our simulation for non-axisymmetric (non-uniform) distributions.

### 5.2.1 Axisymmetric Distributions

Figure 5.2 compares phase space recovered by tomography (first column) to the one generated directly by WARP (second column). Two beams are shown with the same energy (5 keV) but different intensity. Detailed parameters of these beams are listed in Table 5.1. Only  $xx'$  phase spaces are depicted since axisymmetry is assumed. The third column shows the corresponding beam distribution in configuration space. For the low current beam (Beam 1 in Fig. 5.2) due the low intensity parameter ( $\chi = 0.25$ ), space charge effects are neglected in the analysis and as seen in Fig. 5.2 good agreement between Tomography and direct WARP phase space is obtained. To quantify the degree of agreement of the phase spaces we have calculated the emittances in both cases and found the direct WARP and reconstructed phase space to agree within 5%. For the higher current beam (Beam 2 in Fig. 5.2) significant space charge forces are expected ( $\chi = 0.92$ ). Therefore, the linear space charge force term is included in our tomography algorithm as previously described. A comparison between the tomographic reconstructed and direct WARP generated phase space shows relatively good agreement even though there is small difference in size. Still, however, emittance calculated for these distributions fall within 10%.

Table 5.1: Beam parameters used in the simulation

	Beam 1	Beam 2
Energy, (keV)	5	5
Current, (mA)	1	10
Emittance, 4xrms, ( $\mu\text{m}$ )	6.0	16.0
Beam radius at aperture (mm)	0.4	1.44
Beam radius at screen (mm)	0.54	2.72
Generalized Perveance	$4.2 \cdot 10^{-5}$	$4.2 \cdot 10^{-4}$
Intensity Parameter, $\chi$	0.25	0.92

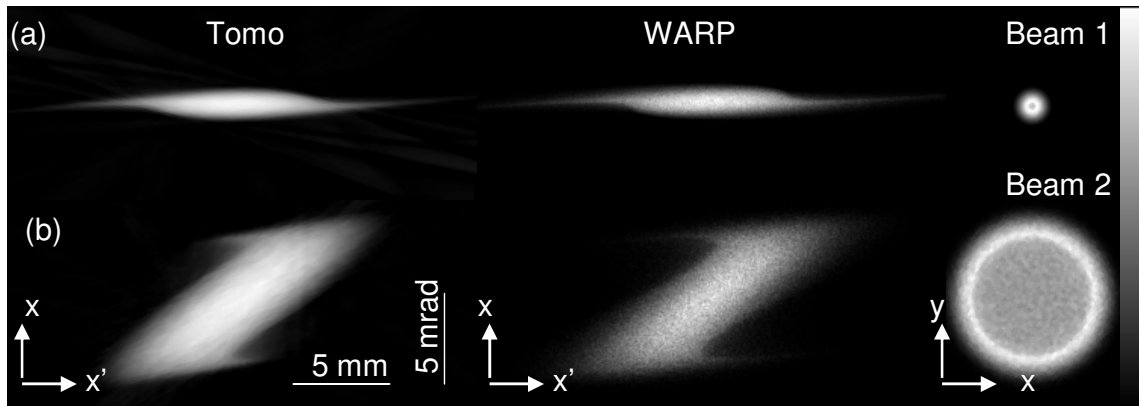


Figure 5.2: Tomographically reconstructed phase space at the plane of the screen (first column) compared with simulated (middle column) for two beams with different 4xrms emittance  $\epsilon_{\text{rms}}$  and current ( $I$ ): (a)  $\epsilon_{\text{rms}} = 6 \mu\text{m}$  and  $I=1 \text{ mA}$ ; (b)  $\epsilon_{\text{rms}} = 16 \mu\text{m}$  and  $I=10 \text{ mA}$ . Far right column corresponds to the beam distribution in configuration space at the same location.

### 5.2.2 Non-symmetric Distributions

For the two previous cases, the beam distribution is assumed to be uniform and axisymmetric. In such cases it is not necessary to account for the variation in the beam rotation in configuration space as the solenoid is scanned. To account for the rotation when the beam is non-axisymmetric each beam photo has to be rotated by  $\theta_r$  before applying the tomography algorithm. Another way to understand this is the following: The captured beam photos are taken in the laboratory frame. However, the matrix analysis for tomography is performed in the Larmor frame, which according to Eq. 5.9, is at an angle  $\theta_r$  relative to the lab frame. Hence, before doing tomography, each screen photo has to be transferred into the Larmor frame and so has to be rotated by  $\theta_r$ .

The procedure for tomography for non-symmetric distributions is as follows:

1. Capture a beam photo.
2. Calculate the angle difference,  $\theta_r$ , between Larmor frame and lab frame by using Eq. 5.9.
3. Bring the photo in the Larmor frame  $(x_L, y_L)$  by doing the transformations:  $x_L = x \cos \theta_r - y \sin \theta_r$  and  $y_L = x \sin \theta_r + y \cos \theta_r$ .
4. Do tomography with those photos by following the procedure described in Sec. 5.1

To illustrate the importance of this, we generate a space charge dominated beam using the parameters of Beam 2 with a highly nonuniform initial distribution as

shown in Figure 5.3(a). After the beam passes the two solenoids, the new distribution is shown in Figure 5.3(b) and the corresponding direct WARP generated phase space at that location is depicted in Fig. 5.4 (second column). No evidence of the initial beam nonuniformity is shown in configuration space, however it is visible in  $xx'$  phase space. Applying tomography to recover the phase space and including the rotation  $\theta_r$  leads to a distribution (Fig. 5.4, third column) that is in agreement with what we get with WARP. Exact agreement, however, is not expected since the initial non uniform distribution is a source of nonlinear space charge forces that are not included in our tomography reconstruction. Note that, if the beam configuration space rotation were not accounted for, tomography would result in increased discrepancy (Fig. 5.4, first column).

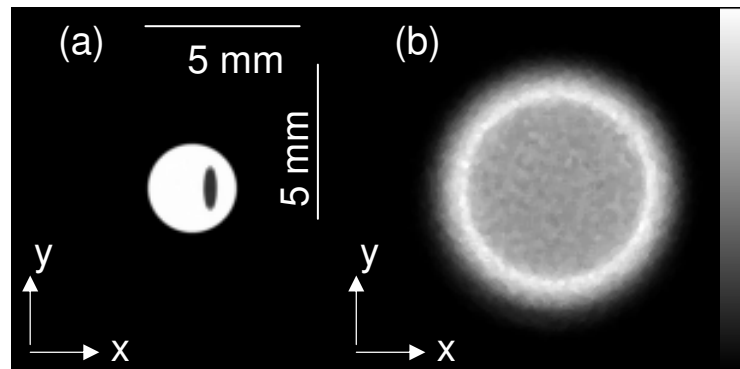


Figure 5.3: Distribution of the same beam at two different locations: (a) at the start ( $z=0$  cm); (b) at the screen ( $z=43.0$  cm).

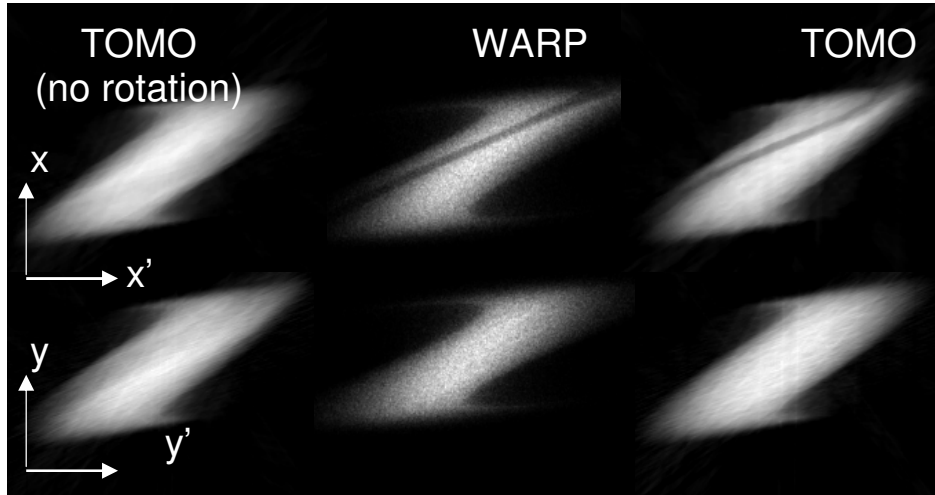


Figure 5.4: Phase space at the screen location generated by WARP directly (middle column) in comparison to tomography before rotating the photos by  $\theta_r$  (first column) and after (third column).

### 5.3 Long Solenoid Experiment (LSE)

After validating the tomography algorithm with WARP simulations, we are interested to apply it experimentally to perform phase space measurements. Our experiment was carried out on the Long Solenoid Experiment (LSE) [57, 58] illustrated in Fig. 5.5. Our transport line consists of a thermionic gun, two short solenoids, S1, and S2 and a phosphor screen downstream. The electron gun is a variable-perveance gridded gun developed and constructed at the University of Maryland. The gun can produce a wide range of beam parameters and its energy varies from 1-5keV. The cathode has a Pierce-geometry and a planar configuration consisting of the heater, cathode and grid. The radius of the cathode is 4 mm and the heating area is  $0.5 \text{ cm}^2$ . The distance between the anode and cathode is adjustable by

means of micrometers and can be set from 9.3 mm to 23 mm, and therefore allowing changing the beam perveance. Similar adjustments in the beam intensity can be performed with an aperture plate which is located downstream of the anode. Downstream of the electron gun there are two short solenoids located 13.0 cm and 29.5 cm from the aperture and have effective lengths equal to 4.34 cm and 4.24 cm, respectively. Beam distributions are collected with the aid of a fluorescent screen that was placed 43.0 cm from the aperture. Figure 5.5(a) presents a simplified diagram showing a schematic layout of the LSE, and Fig. 5.5(b) shows the actual photo of the LSE.

The current in each solenoid can be adjusted individually by different DC power supplies. The solenoidal magnetic fields were measured by a Bell gaussmeter with a longitudinal Hall probe. The analytical expression of the on-axis magnetic field for each of the solenoid, which is a fit to the measured field data, is given by the formula [59]

$$B_z(0, z) = B_0 \exp\left(-\frac{(z-z_0)^2}{d^2}\right) \left[ \operatorname{sech}\left(\frac{(z-z_0)}{b}\right) + c \sinh^2\left(\frac{(z-z_0)}{b}\right) \right], \quad (5.19)$$

where  $B_0$  is the maximum axial magnetic field;  $z_0$  is the solenoid center position; and  $b$ ,  $c$  and  $d$  are fitting parameters different for each solenoid. Table 5.2 shows the fitting parameters of the two solenoids obtained elsewhere [58]. Fig. 5.5(c) represents the fitted axial magnetic field profile along the  $z$ -axis.

Table 5.2: Fitting parameters of the two short solenoids on the LSE

	S1	S2
b (cm)	3.443	3.936
c	0.032	0.084
d (cm)	4.415	3.887



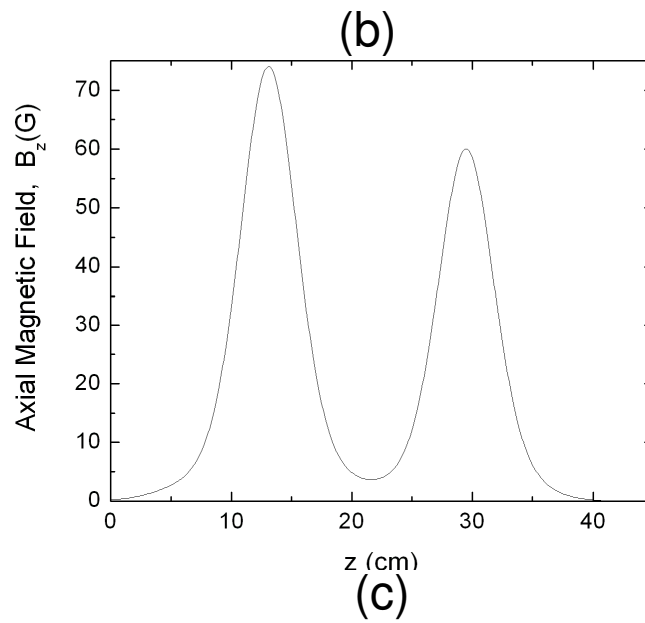
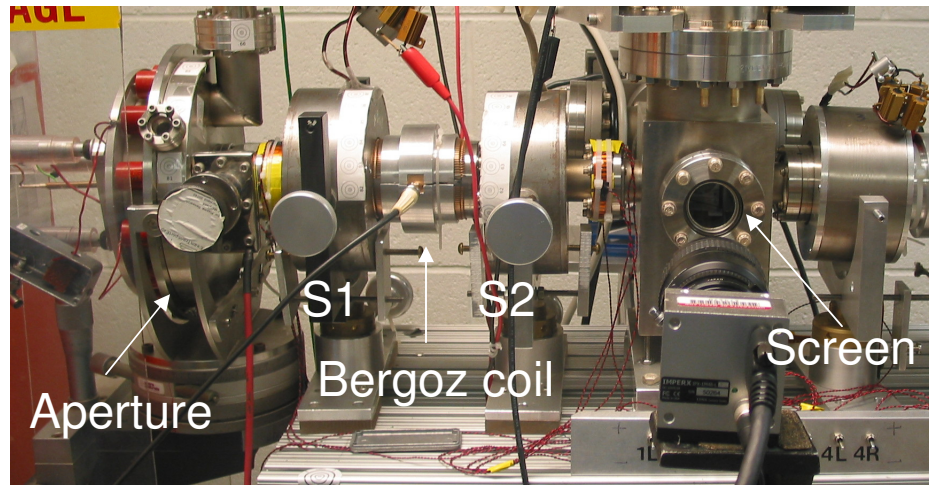
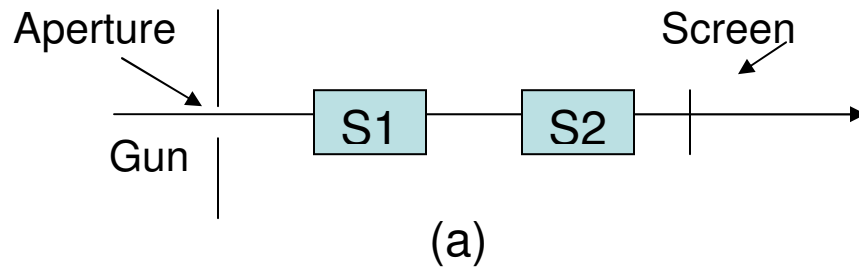


Figure 5.5: Experimental configuration of the LSE. : (a) schematic layout; (b) actual configuration; (c) Axial field on the axis of symmetry for solenoid currents 4.15A (S1 ) and 3.2 A (S2).

## 5.4 Experimental Results

We present now experimental results of phase space tomography on the LSE. In Sec. 5.4.1 we focus on beams that are passing through a uniform aperture once they exit the gun. In Sec. 5.4.2 we discuss the relation between magnet strength and emittance and show that depending on the focusing strength significant emittance growth can occur as the beam passes through the solenoids. In Sec. 5.4.3 we reconstruct phase spaces for beams passing through a highly non-uniform aperture after they exit the gun and report some interesting physical insights.

### 5.4.1 “Uniform” Aperture

In this section we generate phase space maps on the screen by tomography for beams that are passing through a uniform aperture. Then, we compare our results with simulation. For our experiment the beam energy is set at 4 keV and the beam pulse is 100 ns at a frequency of 20 Hz. The anode-cathode gap is adjusted at 22 mm from the cathode. The aperture passes roughly 1/8 of the full beam current resulting in a 12 mA beam with generalized perveance  $7.1 \times 10^{-4}$  and unnormalized  $4 \times$  rms emittance of 30  $\mu\text{m}$ . One Bergoz fast current transformer between them is used to measure the beam current. When S1 and S2 are scanned, the phosphor screen displays the transverse current density (integrated over many pulses). In our experiments we varied the number of scans and found that 48 scans are sufficient to reduce the phase space background noise to less than 5% of the peak intensity. The solenoid strengths have been chosen to: (1) reduce effects from the solenoid’s nonlinearities (2) rotate the phase space distribution by  $180^\circ$  (3) keep the beam size within the fluorescent

screen limits (4) assure zero magnetic field at the beam aperture and screen location. The beam intensity pictures are captured by the programmable digital charge coupled device (CCD) camera (IMPERX-1M48) described in Chap. 4 (see Sec 4.3.1). Each scanned beam distribution is then projected into  $x$  and  $y$  axes in order to obtain projections of the  $xx'$  and  $yy'$  phase spaces, respectively (see Sec. 2.2.2). Following the procedure in Sec. 2.4.2, the reconstruction was advanced to the screen location so that distributions in both spatial and phase space can be compared at the same plane.

To illustrate the experimental results, we select to reconstruct the phase space for three different magnet pairs that correspond to typical operating parameters and illustrate interesting physical properties of space charge modes [47, 60]. Figure 5.6 and Fig. 5.7 show experimental results in the  $x$  and  $y$  planes, respectively. The magnet strength values as well as the measured beam emittances are listed in Table 5.3 (for  $x$ -axis) and Table 5.4 (for  $y$ -axis). In Fig. 5.6 (and Fig. 5.7) the first column corresponds to beam in configuration space. These distributions show the presence of ring shaped modulations at the beam edge [Fig. 5.6(c)], that travel further toward the beam core as the external focusing is increased [Fig. 5.6(a)]. The corresponding phase space plots (second column) show particles with high inward velocities at the locations where these modulations appear. This result is in agreement with previous experiments and simulations [47] and is attributed to the initial nonequilibrium at the edge of the beam. Particularly, the presence of beam edge particles with nonzero velocities at the source results in a force imbalance that leads to these particles initially moving outside the main body of the beam and following different orbits than the bulk of the beam. This phenomenon is identical to that causing the transverse

density modulations (waves) in phase space that we have studied in detail in the simulation in Sec 3.5.

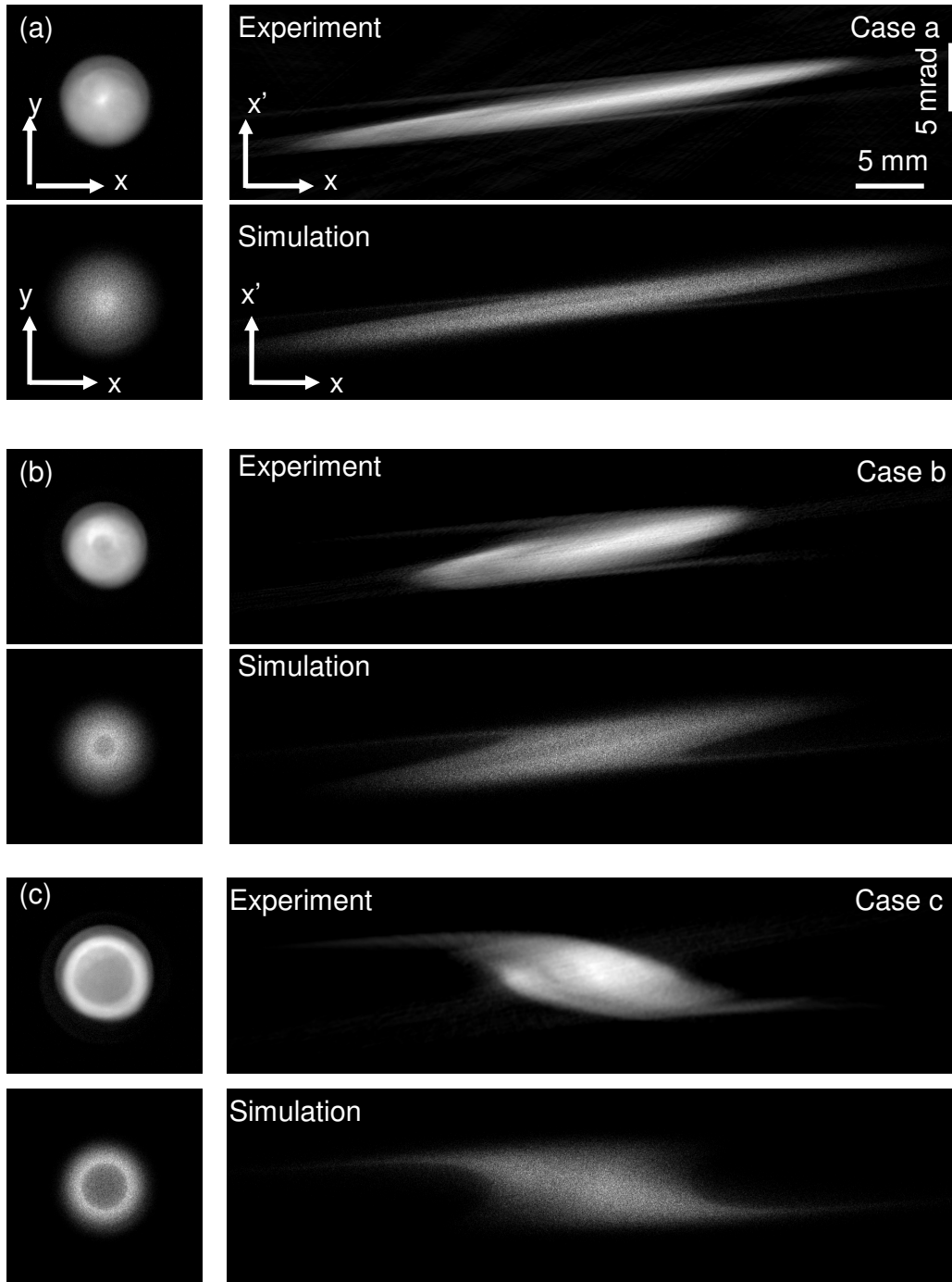


Figure 5.6: Configuration space (left column),  $xx'$  phase space (right column) comparison between experiment (top) and simulation (bottom) for three different magnet pair settings: (a) case a; (b) case b; and (c) case c.

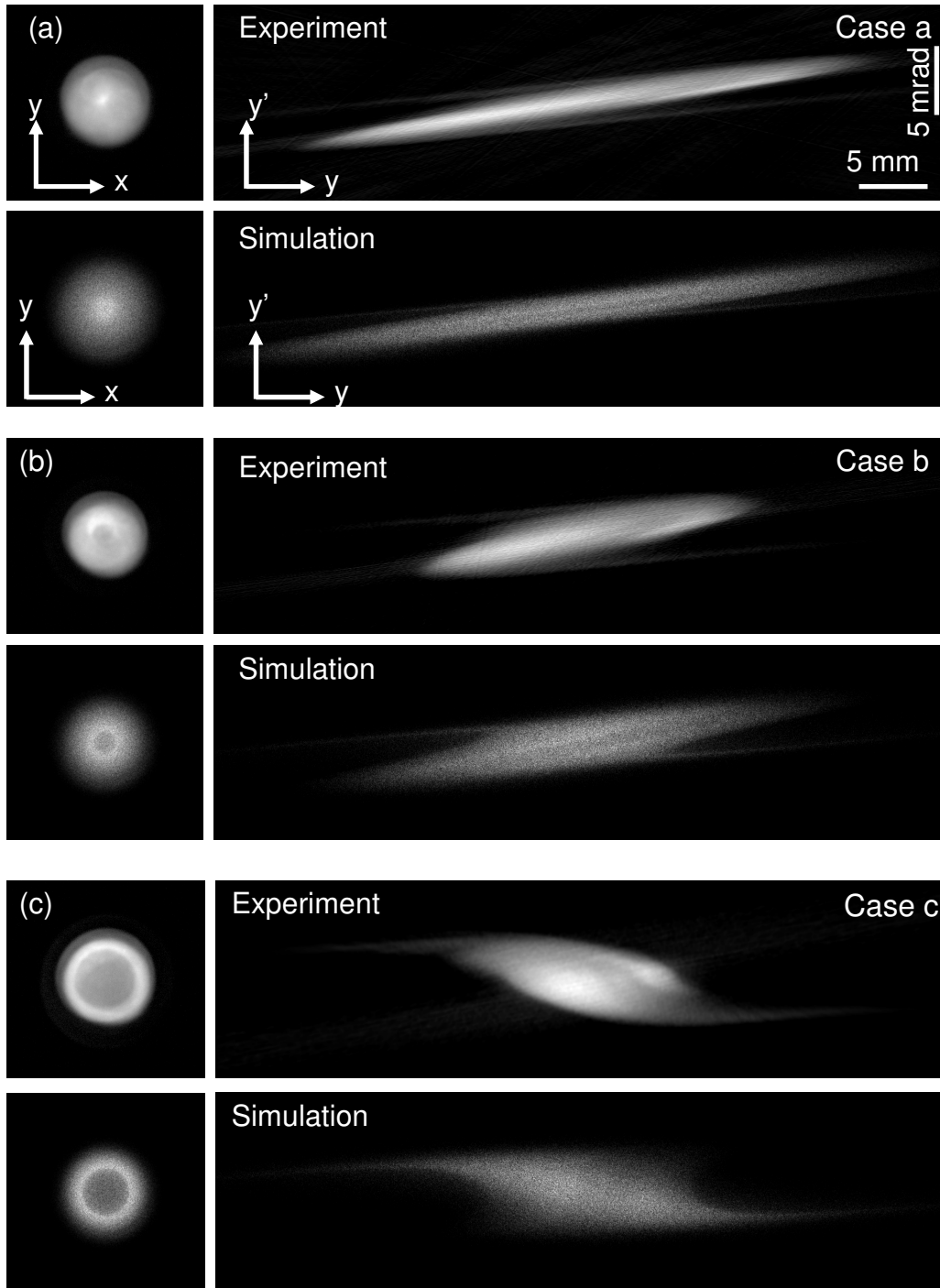


Figure 5.7: Configuration space (left column),  $yy'$  phase space (right column) comparison between experiment (top) and simulation (bottom) for three different magnet pair settings: (a) case a; (b) case b; and (c) case c.

Table 5.3: Solenoid strengths and corresponding emittance measurements along the x axis from tomography and simulation.

	Peak on-axis field 1 (G)	Peak on-axis field 2 (G)	$\epsilon_x$ , (Tomo) ( $\mu\text{m}$ )	$\epsilon_x$ , (WARP) ( $\mu\text{m}$ )	Error (%)
Case a	74.00	60.0	28.4	33.0	13.9
Case b	71.38	60.0	30.1	33.9	11.2
Case c	57.28	60.0	35.0	37.6	6.9

Table 5.4: Solenoid strengths and corresponding emittance measurements along the y axis from tomography and simulation.

	Peak on-axis field 1 (G)	Peak on-axis field 2 (G)	$\epsilon_y$ , (Tomo) ( $\mu\text{m}$ )	$\epsilon_y$ , (WARP) ( $\mu\text{m}$ )	Error (%)
Case a	74.00	60.0	29.0	33.4	13.1
Case b	71.38	60.0	30.7	34.2	10.2
Case c	57.28	60.0	35.1	37.5	6.4

Phase space plots show an unusual perturbation within the distribution that is sensitive to external focusing. To aid in understanding of the origin of such a perturbation, we have conducted simulations using WARP. In the simulation we

assumed that the beam emerges through the gun aperture with a distribution that is uniform (but with a hole inside) in configuration space, similar to the one shown in Fig. 5.3(a), and Gaussian in velocity space. Then, the resulting simulated phase spaces at the location of screen are shown in Fig. 5.6 and Fig. 5.7 (bottom). Clearly, those phase spaces show a perturbation within the distribution similar to the one we see in the experiment. Next, we repeat the simulation again but this time we assume that the beam emerges through the gun aperture with a uniform distribution (no hole inside). The simulated phase space at the screen for case b is shown in Fig. 5.8. Clearly, the beam shows no sign of the previous observed perturbation in either phase space or configuration space. Therefore, we conclude that the observed hollowness in phase space is caused primarily by the initial nonuniform distribution.

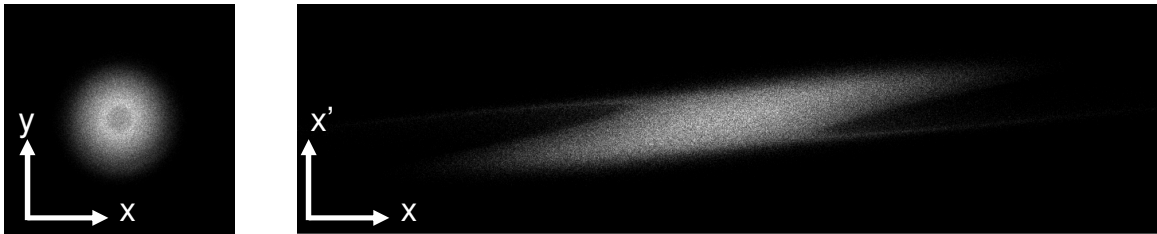


Figure 5.8: Beam distribution at the screen for case b when a uniform beam (no hole) is assumed initially.

The hollowness in phase space is most likely associated with the nonuniform emission from the gun cathode. To verify this, the solenoid magnets in the experiment were adjusted to image the cathode at the fluorescent screen location. Assuming linear optics, and using the thin lens equation, it is estimated that the cathode plane would be focused at the screen when the peak on-axis fields are 74.0 G and 98.0 G



for the first and second solenoid, respectively. Using the above settings in our experiment, we obtain a beam distribution as shown on Fig. 5.9(a). Figure 5.9(b) corresponds to the simulation photo while using the above magnet settings in WARP.

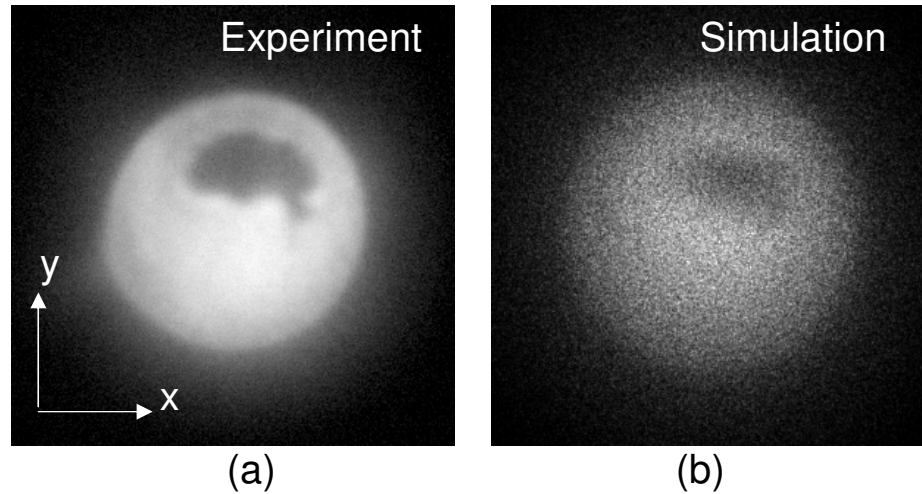


Figure 5.9: Cathode imaging at the screen location: (a) in experiment; (b) in simulation. To simulate the hole effect in WARP we assume that beam emerges through the gun aperture with a uniform distribution (but with a hole inside) similar to that shown in Fig. 5.3(a).

As is evident from the phase spaces in Fig. 5.6 and Fig. 5.7, the agreement between simulation and experiment is good, except for a difference in the phase of perturbation, especially in the third case [Fig. 5.6(c)]. The phase of the perturbation is sensitive to the initial conditions assumed in the simulation. These are difficult to determine, since in this experimental configuration the initial conditions at the gun aperture are not directly measurable. Therefore, we believe that a detailed simulation

of the electron gun would improve the agreement between experiment and simulation; however, this is beyond the scope of the current dissertation.

### **5.4.2 Emittance Growth**

The difference in the emittances between the three cases suggests an emittance growth that depends on the solenoidal magnet strength. Furthermore, the pattern of the emittance increase is the same for both simulation and experiment. For instance case c has the highest emittance and case a has the lowest emittance for both simulation and experiment. In order to gain an understanding of this growth we plotted the beam envelopes for the three cases as predicted by WARP (see Fig. 5.10). The dashed line indicates the positions of the two solenoids.

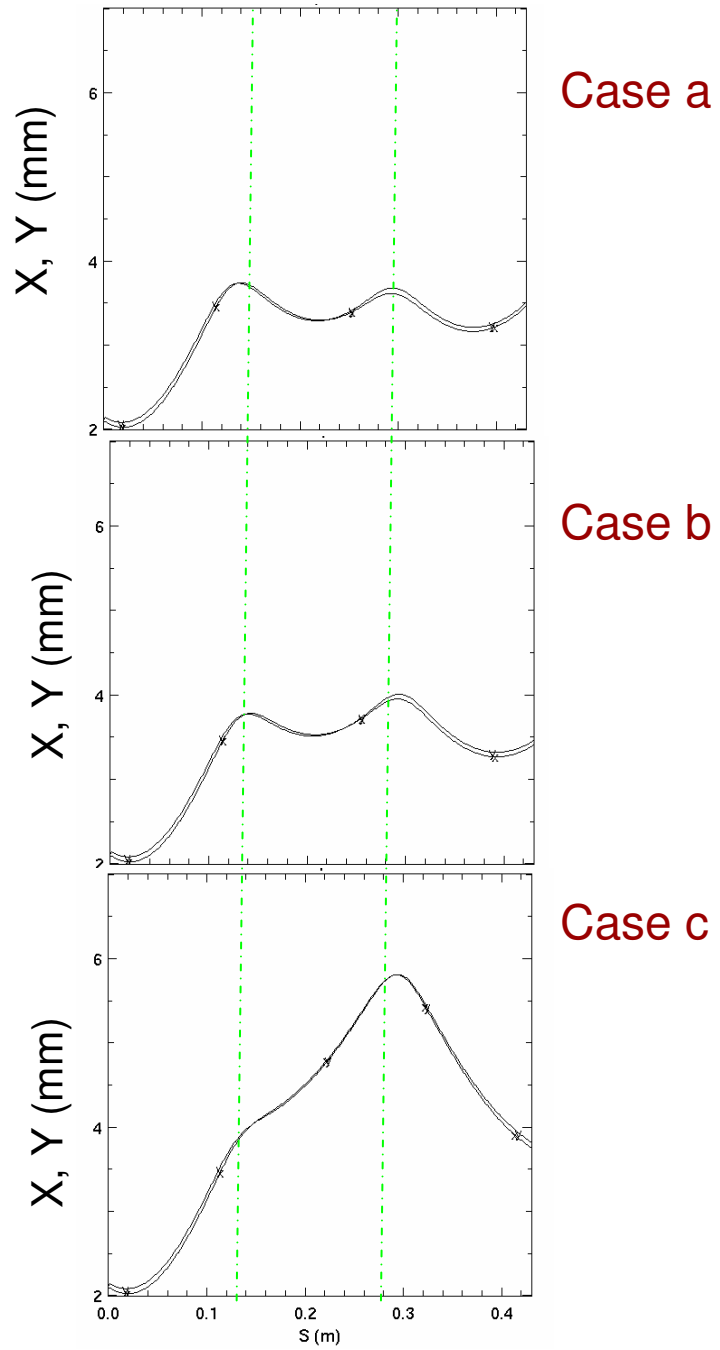


Figure 5.10: Evolution of the beam envelope,  $X$ , and  $Y$ , for the three different magnet pairs as obtained from WARP simulation. The dashed lines show the central position of the solenoids.

Looking at Fig. 5.10 we can do the following observations: The beam size on the second solenoid, S2, depends on the magnet strength of the first solenoid, S1. For case c, where the solenoid strength of S1 is at its weakest (relevant to the other cases) we have the largest beam entering S2. That's the case where the emittance growth is also the highest, suggesting that the large beam samples more nonlinear terms of the magnetic field. Therefore, extra care has to be taken in experiments with solenoids so that the beam size remains as small as possible.

### 5.4.3 “Exotic” Beam Distributions

Very similarly to UMER, in the LSE at the exit of the gun we have an aperture wheel that we can rotate in vacuum and select a number of different apertures. Of particular interest is the aperture that generates 5 distinct but interacting beamlets. This aperture is very similar to the one we used for the five beamlet experiment on UMER (see Chap. 4) with the only difference being here that not all beamlets have the same size. Figure 5.11(a) shows a schematic representation of that aperture including the sizes (distances not drawn to scale) and Fig. 5.11(b) shows an image of that aperture as seen in the experiment at the screen, downstream. Notice that the size of central beamlet is about 7% the size of the other four.

In the experiment we are interested in reconstructing the phase space at the location of the screen. From the geometry of the aperture, and Eq. 3.3 we can calculate an effective, or twice rms initial radius of the 5 beamlet distribution by using the formula

$$r_u = \sqrt{\frac{4}{5}r^2 + \frac{r_s^2 + 8\delta^2}{5}} = 5.22 \text{ mm} \quad (5.20)$$

where  $r$  is the radius of the large beamlet and  $r_s$  is the radius of the small beamlet .  
 The anode-cathode distance is set at 22 mm allowing a beam current equal to 31.2 A  
 in the Bergoz. The beam energy was 4 keV and the beam pulse was 100 ns at a  
 frequency of 20 Hz.

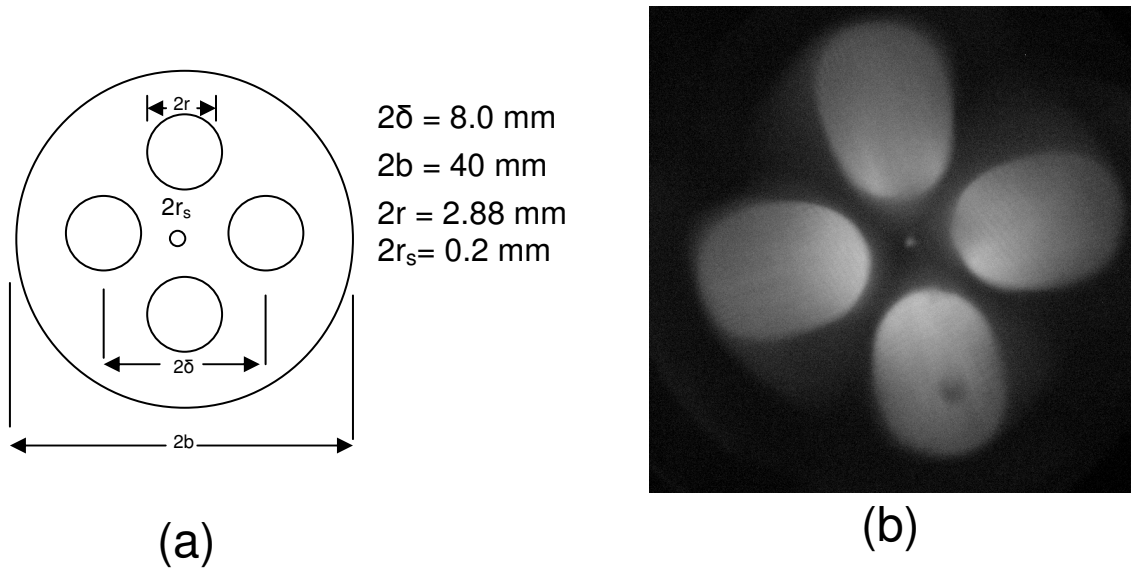


Figure 5.11: Five beamlet distribution in the LSE; (a) Aperture, (b) Actual photo at the screen that shows an image of the aperture. Note that  $2b$  is the diameter of the beam pipe in LSE.

Figure 5.12 illustrates phase spaces reconstructed by tomography at the screen for four different magnet pairs which are listed in Table 5.5. The measured emittances along the x-axis from the phase spaces are also reported on that table. For Case 3 and Case 4 we measure the highest emittance which are believed to be caused by the weak focusing of the first solenoid, as discussed earlier in Sec. 5.5.2. Both distributions (phase space and configuration space) show a highly asymmetric structure due to the initial complex distribution. Very similarly to five beamlet

experiment in Chap. 4 the beamlets merge in configuration space but are still distinct in phase space. However, in contrast to the five beamlet experiment on UMER the beam in configuration space shows a 4-fold symmetry caused primarily because of the geometry of the aperture.

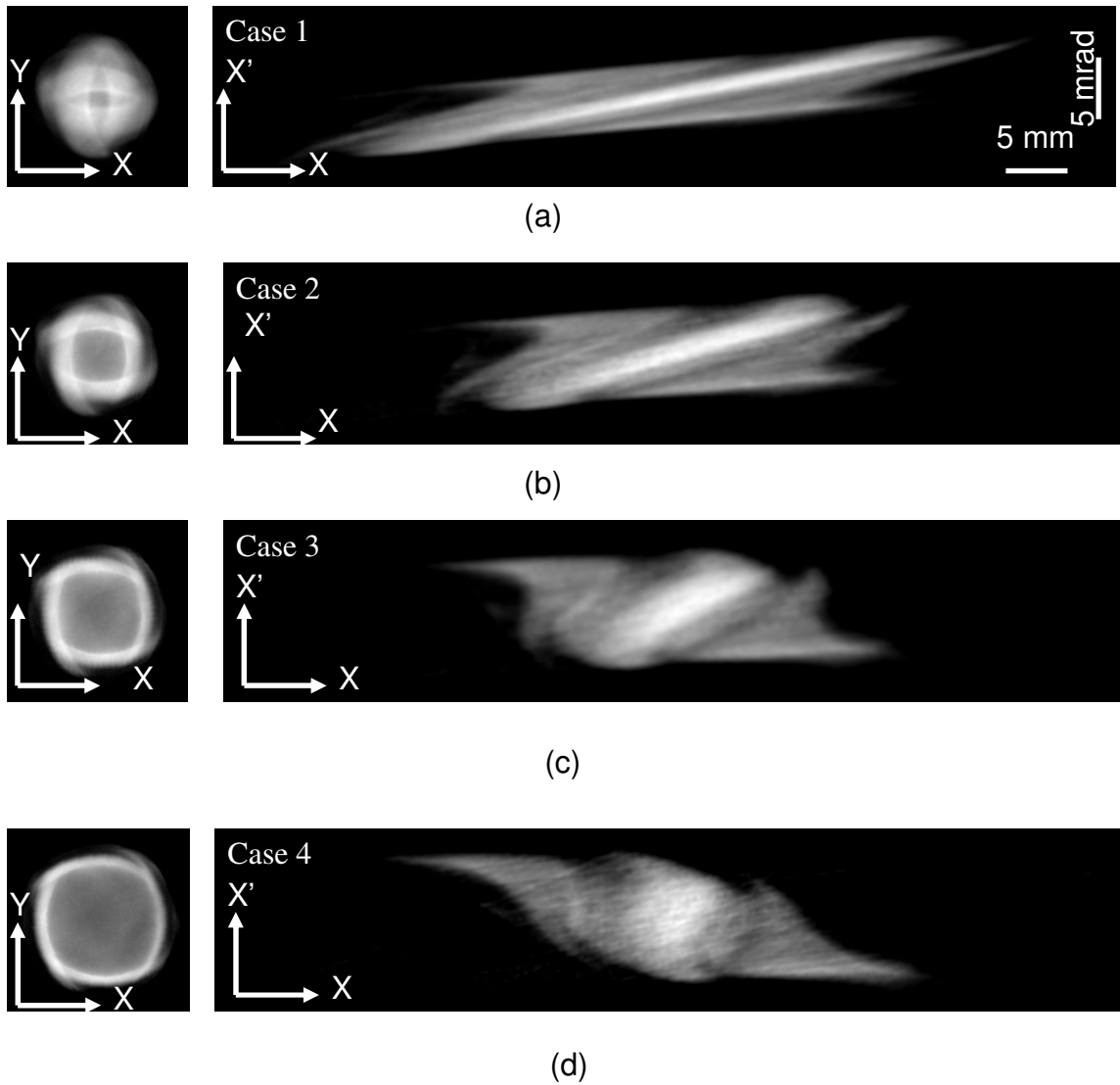


Figure 5.12: Configuration space (left column),  $XX'$  phase space (right column) from the experiment for four different magnet pair settings (Table 5.5): (a) case 1; (b) case 2; (c) case 3; and (d) case 4.

Table 5.5: Solenoid strengths and corresponding emittance measurements along x-axis from tomography for the multi-beamlet experiment.

	Peak on-axis field 1 (G)	Peak on-axis field 2 (G)	Emittance (Tomo) ( $\mu\text{m}$ )
Case 1	64.3	60.0	87.0
Case 2	57.2	60.0	94.0
Case 3	50.2	60.0	94.3
Case 4	43.1	60.0	100.0

## 5.5 Summary

To summarize, tomographic techniques using solenoid magnets have been employed for the first time to reconstruct the beam phase distribution. We have demonstrated that the configuration space rotation from the magnetic field cannot be neglected when the axisymmetry is broken by an initial density perturbation. Additionally, we address the importance of accurate specification of the initial distribution, to the downstream evolution, in both phase and configuration space. Specifically, we show that depending on the external focusing, an initial non-uniform distribution may result to density perturbations either in phase space or configuration space. Furthermore, we show that solenoids can induce an emittance growth. The growth depends on the beam size while it passes through the solenoid. Finally, experiments and simulations confirmed the presence of a ring of particles that initially

move outside the beam edge and are subsequently reflected into the beam with excess inward velocities.



## Chapter 6 Time-Resolved Tomography for Intense Particle

### Beams

A high brightness and low emittance beam is *a priori* requirement for X-ray Free Electron Lasers and Spallation Neutron Sources. For such applications knowledge of the time-sliced parameters of beam current, energy spread and transverse emittance is an important requirement to understand their evolution. For instance characterization of the transverse phase space of the beam at the injector exit is necessary, as it allows the tuning and verification of the photoinjector properties. Such an example is emittance compensation [34], a process which is used to correct for the correlation between the phase space angle and the longitudinal position of slices. Even though a number of studies have been conducted so far to do time-resolved phase space maps and slice emittance measurements [35-37] the analysis was restricted to beams with little space-charge and therefore its influence was not included in the analysis. In this chapter for the first time we study the evolution of transverse phase space slices within a space-charge dominated beam. By introducing longitudinal perturbations we study the correlation between longitudinal and transverse dynamics. We report high resolution phase-space maps within a 3 ns window over several locations along a 60 ns beam pulse. We show that longitudinal perturbations can have an impact on the transverse phase space and can cause emittance growth.

The outline of this chapter is as follows: In Sec 6.1 we review the experimental details: screens, camera used and the implemented experimental

configuration. In Sec. 6.2 we study the impact on the transverse phase space of a perturbation over a rectangular beam pulse. In Sec. 6.3 we study the correlation between longitudinal and transverse dynamics by measuring transverse phase spaces within several beam slices for a parabolic beam pulse. Finally, in Sec. 6.4 we provide a summary and conclusion.

## **6.1 Experiment Details**

We conducted our experiments at the LSE system (see Sec. 5.3) and involved the first two short solenoids and the screen (LC1). Details about this system can be found in Chap. 5. The electron gun, produced 5 keV, pulses at a rate of 60 Hz. A 3.2 mm diameter aperture was set 22 mm from the cathode. The fast phosphor screen was placed at LC1 (43 cm from the aperture) and the light emitted from the screen was directed onto the ICCD camera. The camera gate was controlled from 100 ns up to 3 ns to obtain time-integrated and time-resolved images of the beam.

In this section we review the experimental details such as the screens we use (see Sec. 6.1.1), and the imaging control system and configuration we implement (see Sec. 6.1.2). In Sec. 6.1.3 we discuss the method we use to produce longitudinal perturbations.

### **6.1.1 Fast Screens**

Optical Transition Radiation (OTR) is a well known diagnostic tool to measure the beam distribution [61] and was initially implemented in our experiments for time-resolved measurements. OTR is generated when a charge particle crosses the interfaces from vacuum into a conductor and is widely used to diagnose relativistic

beams. The low light yield due to the low-energy of our beam required long integration times and therefore increased the time of the measurement [62]. Hence, in our experiments we finally decided to employ fast phosphor screens which reduced the measurement time significantly.

The screens consist of a ZnO:Ga formula on a quartz plate and were produced by Lexel Imaging Systems, Inc.. The doping material is Ga that is present in very small quantities. The grain sizes are in range of 5-8  $\mu\text{m}$ . The phosphor is inorganic and emits in the near UV with peak close to 390 nm (equivalent to 3.2 eV). The efficiency is  $< 1\%$  and for a 10 keV electron beam we get about 30 photons. The decay time is 2.4 ns. The phosphor is very sensitive to the heat and the current load. Therefore, to protect the phosphor and extend its lifetime we cover the material with a thick layer (about  $1000 \text{ \AA}$ ) of conductive material that for our case is Aluminum. Care must be taken on the applied field strength since the screens are rated to 4 kV/mm field strength. Above this point the Al on the surface may peel off from the phosphor.

### **6.1.2 Imaging**

An intensified charged-coupled device (ICCD) camera (PIMAX2 from Princeton instruments) has been employed in our experiments. The CCD uses an image intensifier that is fiber optically coupled to the CCD chip to increase the sensitivity to a single photon level. The image intensifier's bandwidth is broad covering wavelengths from the UV up to NIR, and is therefore suitable for the emission width of our fast phosphor screen. Furthermore, it offers nanosecond gating

capability and a pulse generator allows setting the delay and gating signal. The dynamic range of the PI-MAX2 camera is 16-bit and so provides a very wide intensity range for detecting even weak signals and halos. The lens type used was an AF Micro-NIKKOR 60mm f/2.8D (see Sec. 4.3). Image acquisition and camera control was done by using Winview32 software (Roper Scientific) and the beam photo resolution was 512x512.

### **6.1.3 Generation of Longitudinal Perturbations**

There are a number of different ways to produce longitudinal perturbations to the beam current. These can be done by using a laser [63], using an induction module [64] or by using an electrical method [62]. For our experiment we employ the electrical method where we generate a pure current modulation at the electron gun by modifying the gun electronics: The cathode is biased positively relative to the grid to impede current flow from the cathode. A negative pulse is applied to the cathode making it negative with respect of the grid, thus allowing electrons to be emitted. The pulse is generated by a cathode pulse system and is transported through a transmission line [66]. The longitudinal perturbation is created by connecting a cable at the middle of the pulse generation transmission line through a “T” connector. Depending on the bias voltage the current modulation can be positive (more current) or negative (less current). Furthermore, by manipulating the pulse generation circuit of the electron gun with a low pass filter [62] we can create beams with parabolic beam shapes.

## 6.2 Longitudinal Perturbation Study

In this section we are interested to study the effect of longitudinal perturbations in the transverse phase space. We show that if we introduce a small perturbation on a rectangular beam pulse this can result in significant modifications of the transverse phase-space. In Sec. 6.2.1 we use the ICCD camera and do time-resolved phase space maps with the perturbation on and off. In Sec.6.2.2 we do time integrated measurements over the same beam pulse.

For our experiment the bias voltage was set at 55 V leading to a negative perturbation. The current profiles, measured at the Bergoz coil, with and without perturbation are illustrated in Fig. 6.1. Note that the perturbation was generated at the center of the flat top region. The measured beam current without perturbation was 25 mA and the width of the perturbation was about 7 ns and it corresponds to about 80% of the total beam current.

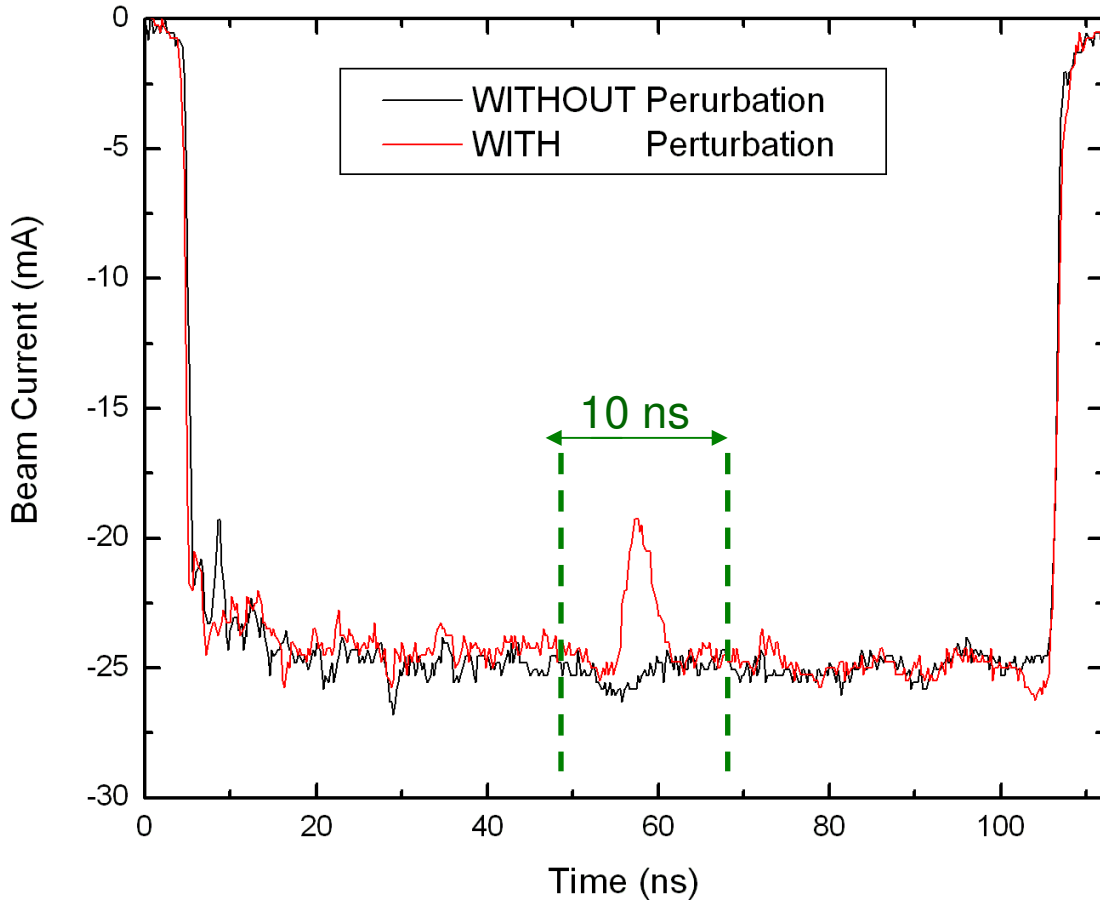


Figure 6.1: Beam signal at the Bergoz. The red profile shows the current profile with perturbation on. The black curve shows the profile with the perturbation turned off. The main beam current was 25 mA. The perturbation amplitude is roughly 25% of that of the main beam. The camera gate was set at 10 ns (green dashed line).

### 6.2.1 Time resolved (slice) tomography

A 10 ns gate is applied to the ICCD camera to obtain time-resolved images of the charge particle beam on the screen. The gate is applied along the negative perturbation part of the beam (green line in Fig. 6.1) and then compared to that with the beam without perturbation. In a similar fashion to that described in Chap. 5 the

solenoids were scanned resulting in 48 beam photos (see Sec. 5.4.1) on the screen which then were analyzed to obtain the beam projection and finally the beam phase space (see also Chap. 2).

Figure 6.2 shows the reconstructed phase space at the aperture. To reveal more details about the beam distribution the phase space slope was subtracted following the procedure described in Sec. 4.5.1. Table 6.1 summarizes the estimated beam parameters from the reconstructed phase-space at the beam aperture for the two cases. Clearly a change of the phase space is seen when the perturbation is turned on (Fig. 6.2(b)). As is evident, the beam parameters are not the same for those cases. For instance, the emittance with perturbation on is measured to be higher.

An interesting observation is that the slope of the beam envelope we measure from tomography when the perturbation is on is higher relevant to the case when the perturbation is off (see Table. 6.1). A possible reason for that could be due the fact that when the perturbation is on the space-charge intensity of the beam is higher [62]. Due to this higher space-charge intensity the beam expands transversely in the gun resulting to a larger beam slope. This is also why we get lower beam current after the beam is passing the aperture. Furthermore, these space-charge effects may explain the higher emittance we measure when the perturbation is on. However, since the 10 ns gate is wide enough and the perturbation is varying fast within this range, what we measure could be also integrated smear of many phase spaces resulting to a higher emittance. Future experiments with lower gate should be performed to investigate this argument.

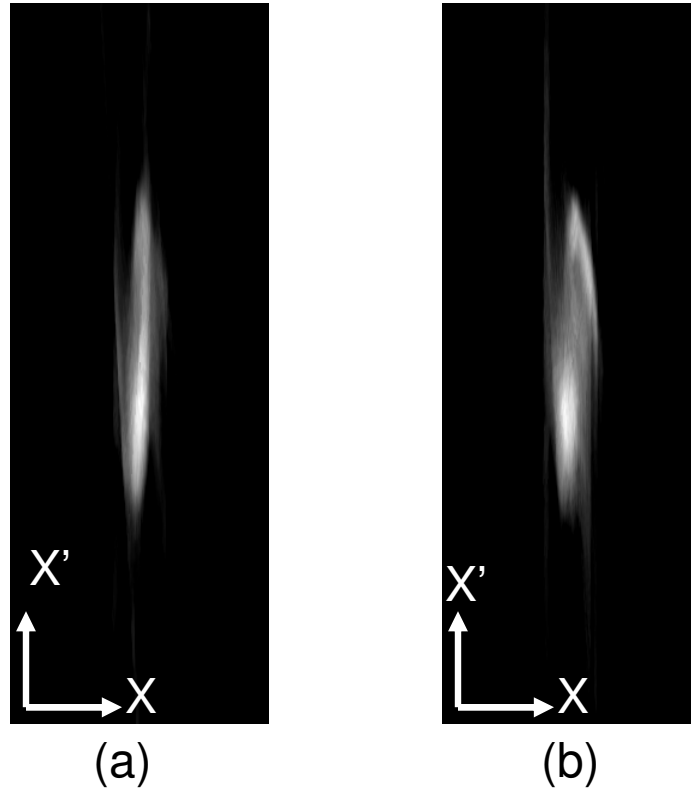


Figure 6.2: Beam phase space distribution recovered by Tomography at the gun aperture ( $z = 0$  cm). (a) Without perturbation; (b) with perturbation turned on. The subtracted slope was  $-6.5$  mrad/mm (no perturbation) and  $-9.7$  mrad/mm (with perturbation). Note that both phase-spaces are at the same scale.

Table 6.1: Beam parameters measured at the aperture from tomography.

Parameter	Perturbation Off	Perturbation On
$2x_{rms}$	1.6 mm	1.6 mm
$2x'_{rms}$	17 mrad	21.0 mrad
$\epsilon_{x,4rms}$	26 $\mu\text{m}$	30 $\mu\text{m}$



Figure 6.3 shows the corresponding beam image on the screen (LC1) as well the Tomographic reconstructed phase spaces at that location. Interestingly, the distributions look very different. First, in configuration space the beam sizes are not equal and the beam with perturbation looks smaller, possibly due to the different focusing it experiences relevant to the main beam. Another interesting observation is the difference in the emittances. The measured emittance was  $28.0 \mu\text{m}$  and  $37.0 \mu\text{m}$  when the perturbation was tuned off and on, respectively. The possible reason for that can be due the fact that the two beams start with different emittances at the aperture. However, for both cases there is an emittance growth relative to the aperture (23% when the perturbation is on and 7% when the perturbation is off).

In Sec. 5.4.1 we show evidence that the solenoids can cause emittance growth; however, here the growth is larger for the case when the perturbation was on. One reason for that could be the higher space-charge of this beam [62] that can cause transverse mismatch. A second reason could be due to the rapidly varying longitudinal field because of the perturbation. A third reason, as discussed before, could be the large window size (10 ns) that can cause integration over many different slices.

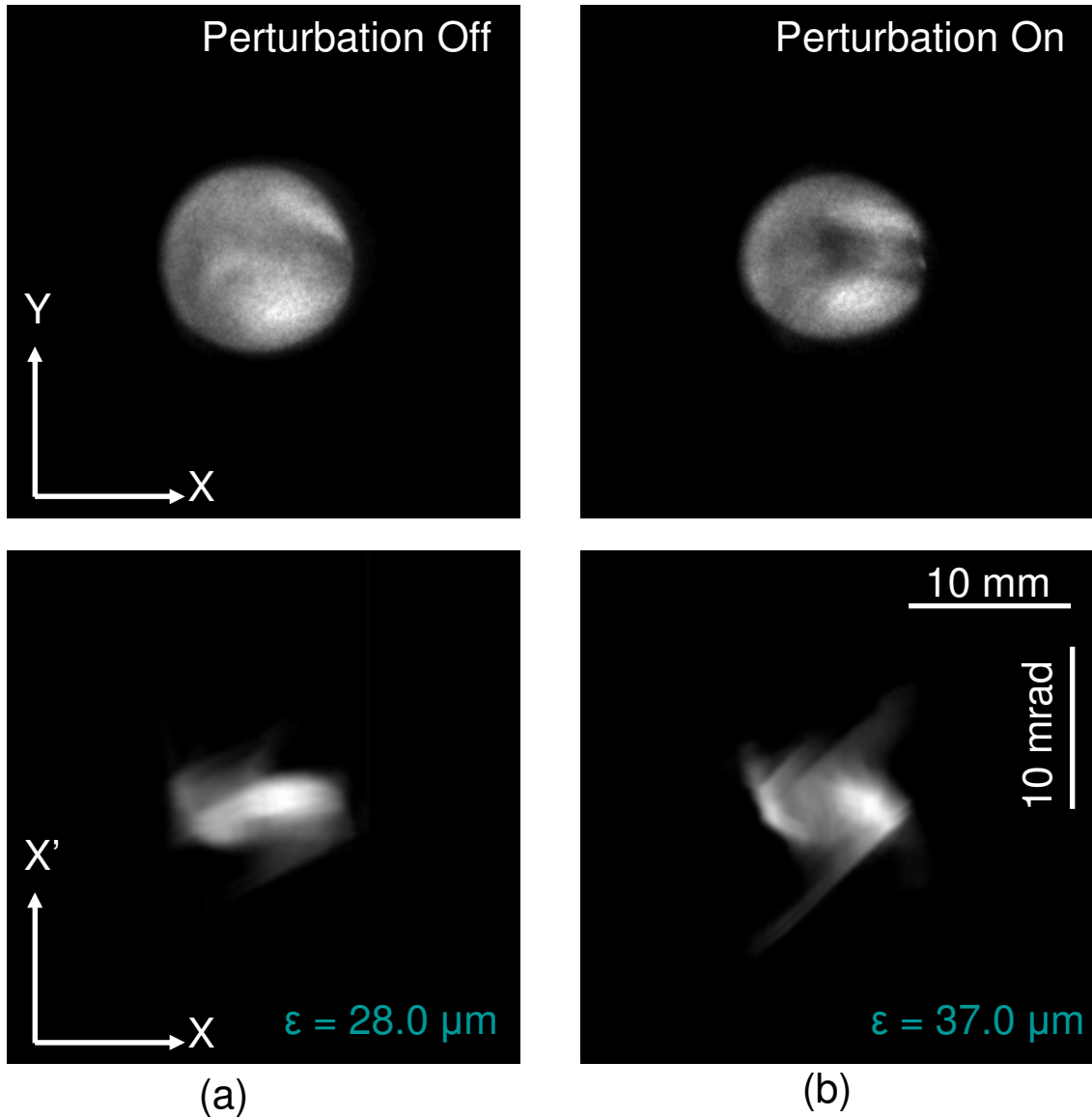


Figure 6.3: Beam configuration space (top) and measured phase space by tomography (bottom) at the screen location: (a) Perturbation off; (b) Perturbation on. Notice that the beam with perturbation has higher emittance. Images are obtained with a 10 ns gate. The subtracted slope was  $-7.4 \text{ mrad/mm}$  (perturbation off) and  $-6.7 \text{ mrad/mm}$  (perturbation on).

### 6.2.2 Time integrated tomography

In the previous section we reported time resolved measurements of the phase space distribution for a rectangular pulse with a perturbation on it and compared our results with the case without the perturbation. Now, we do the same experiment but this time we integrate over the whole beam pulse. For this experiment, the gate of camera is set along the dotted green lines in Fig. 6.4.

Figure 6.5 illustrates the beam distribution in configuration space and phase space without perturbation (Fig. 6.5(a)) and with perturbation (Fig. 6.5(b)) at LC1. We cannot detect any significant differences between the two cases; either in configuration space or in phase space. To quantify this, we calculated the beam emittances and found that they are almost equal (see label inside Fig. 6.5).

In summary, in contrast to time-resolved measurements, time integrated measurements didn't reveal any difference in the transverse beam distribution when a beam was propagating with and without longitudinal perturbation. This observation indicates the usefulness of using fast diagnostics for studying in detail beam properties.

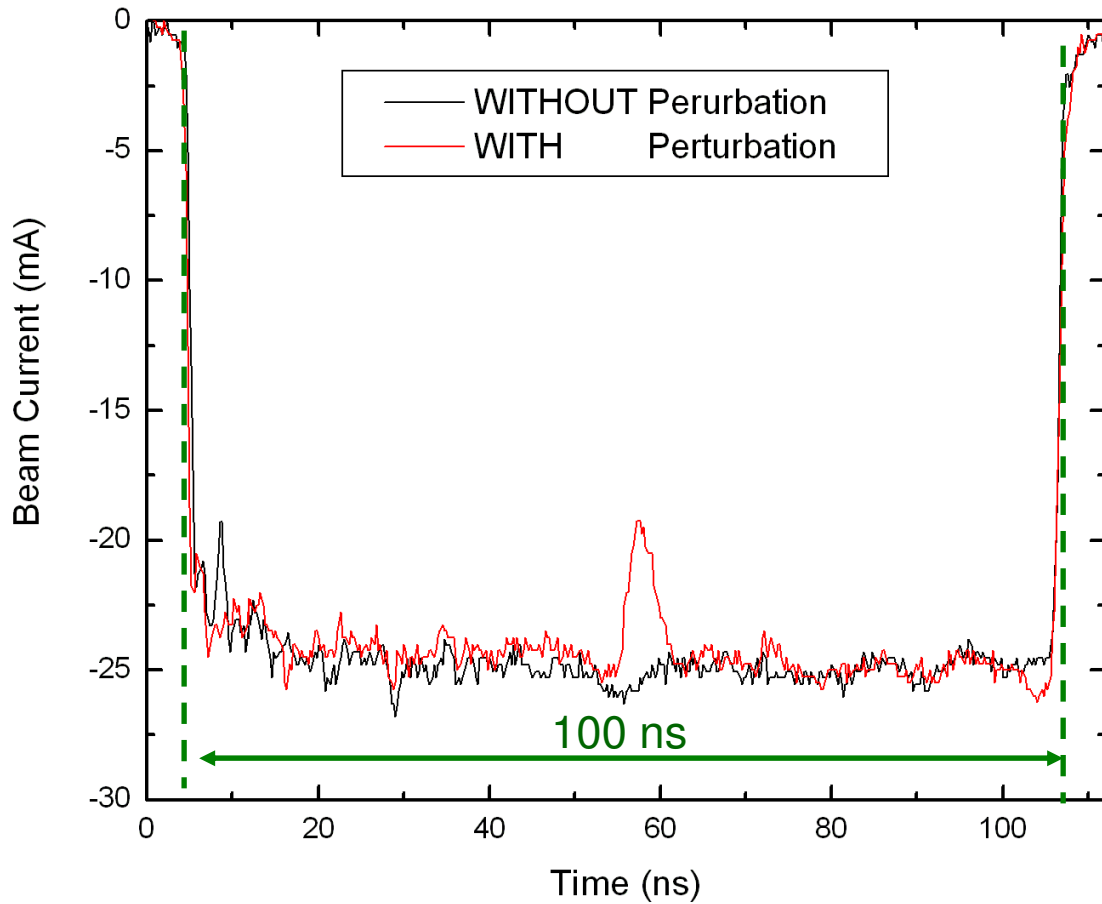


Figure 6.4: Beam signal at the Bergoz. The red profile shows the current profile with perturbation on. The black curve shows the profile with the perturbation turned off. The beam current was 25 mA. The perturbation is roughly 25% of the main current. The camera gate was set at 100 ns and was integrating over the whole beam pulse (green dashed line).

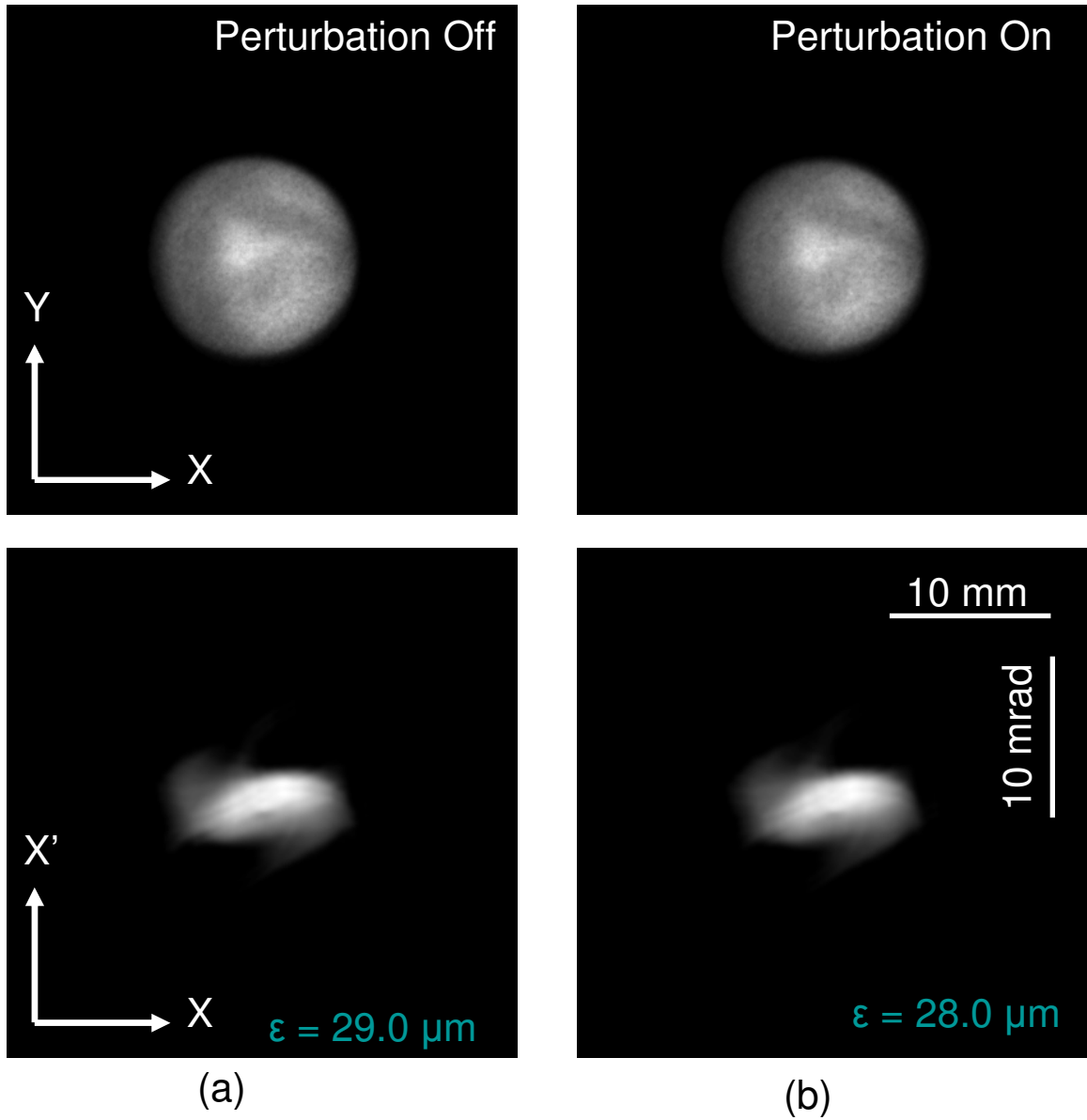


Figure 6.5: Beam configuration space (top) and measured phase space by tomography (bottom). (a) Perturbation off; (b) Perturbation on. Images are time-integrated over the whole beam pulse. The subtracted slope was  $-7.4 \text{ mrad/mm}$  for both cases.

### **6.3 Parabolic Beam Pulse**

The longitudinal dynamics of a parabolic beam bunch has experimental importance to beam acceleration and transport, especially to the beam compression in an induction module because it produces a linear longitudinal electric field [67]. Even more so, laser bunches tend to be Gaussian, so most photo emitted beams are very close to parabolic. Following the discussion in Sec. 6.1.3 we modified the beam current profile and produced a parabolic beam profile. Our aim is to perform transverse phase space measurements along several slices within this pulse and study the correlations between longitudinal and transverse dynamics.

The longitudinal charge distribution of the electron beam bunch from the signal at the Bergoz is demonstrated in Fig. 6.6. The position of the slices used in our phase-space measurement is also illustrated in Fig. 6.6. The width of each slice was 3 ns and Table 6.2 shows the average current of each one.

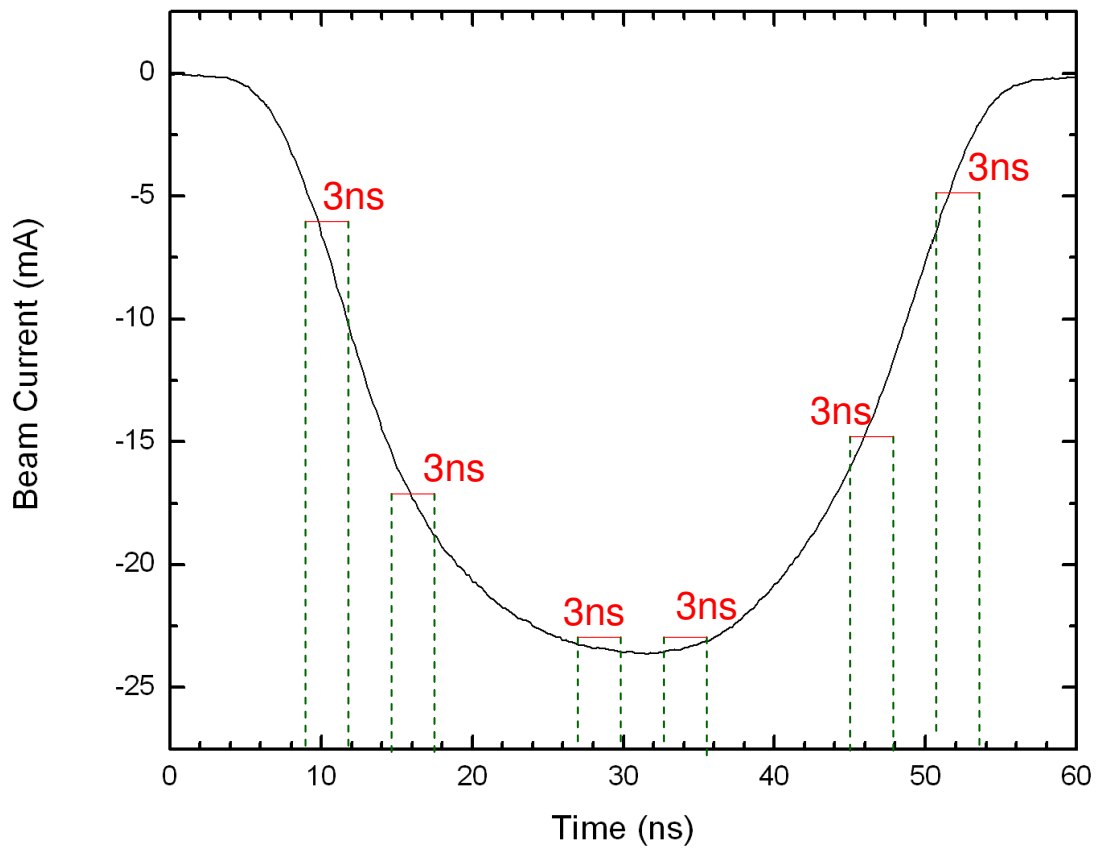


Figure 6.6: Signal collected at the Bergoz coil showing the longitudinal current profile.

Table 6.2: Beam currents and parameters measured at the aperture from tomography.

	<b>Time Window</b>	<b>Current</b>	<b>Emittance</b>	<b>Slope of Envelope</b>
	<b>(ns)</b>	<b>(mA)</b>	<b>(<math>\mu\text{m}</math>)</b>	<b>(mrad)</b>
Slice a	9-12	4.8	29.8	-7.8
Slice b	15-18	15.0	27.0	-11.75
Slice c	27-30	23.1	24.0	-11.0
Slice d	33-36	23.5	24.0	-11.15
Slice e	45-48	16.3	26.3	-11.93
Slice f	51-54	6.6	29.6	-7.9

By setting the ICCD camera gate window at 3 ns, and moving it progressively from the beam head toward the tail we can collect a number of beam photos at the screen (LC1), each corresponding to 3 ns beam slice. Some of those photos are shown in Figure 6.7 and correspond to the case where the solenoids S1 and S2 are set at 97.8 G (current=5.5 A) and 60 G (current=3.2 A), respectively. Carefully examining those photos we can see that they have structure that differs from slice to slice. Such structure has been observed in previous experiment also [57, 62] and is believed to be caused by the nonuniform emission from the aperture [57]. The structure appearance is a function of the beam intensity; therefore since those slices correspond to different beam currents their structure will be also different.



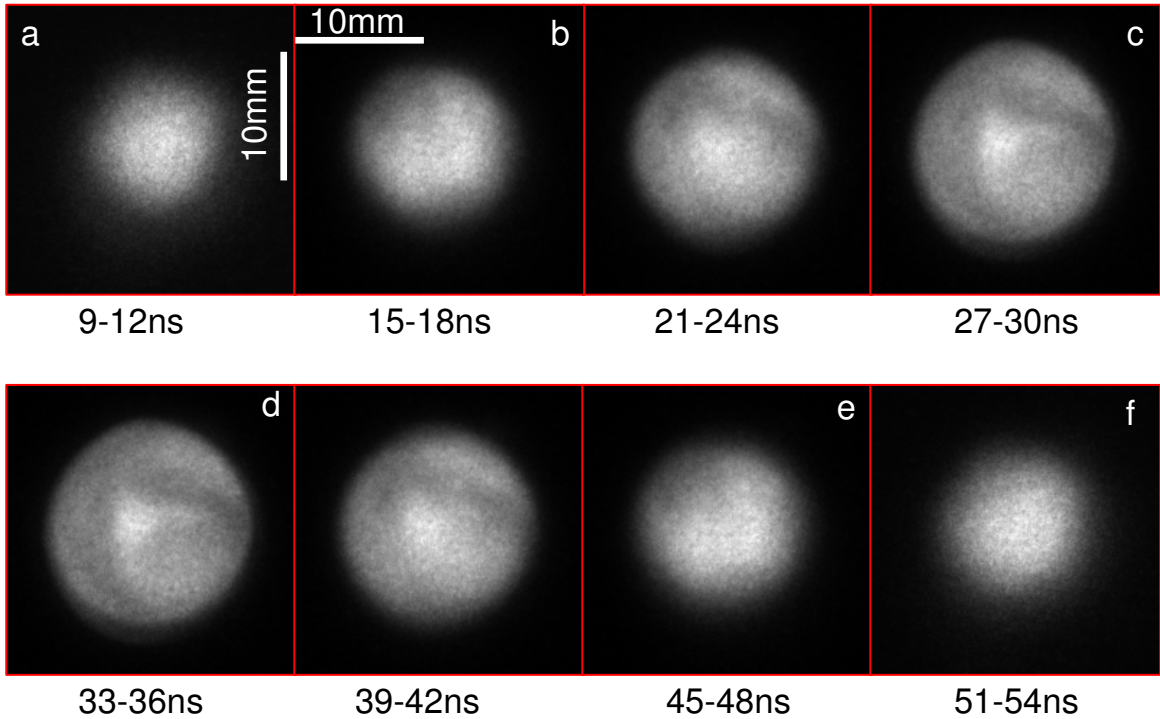


Figure 6.7: Beam slices on the screen obtained by progressively moving the camera 3 ns gate window from the head to the tail of the beam pulse. Each photo is the result of 55 frame integrations.

Now, we are interested to reconstruct the phase space distribution and measure the emittance for the slices a, b, c, d, e, and f. Following the procedure discussed in Sec. 6.1 (see also Chap. 5) we scan the solenoids collect 48 beam photos from the screen and reconstruct the phase space. We reconstruct the phase space at the aperture and get so an estimate of the initial beam emittance and slope of the beam envelope ( $x' = 4 \langle xx' \rangle / x$ , where  $x$  is the beam size). Our results are listed in Table 6.2. We show only data along the  $x$  transverse plane but similar results apply to the other transverse direction also. Those numbers are useful especially because they

provide the initial conditions for our matrix analysis for the downstream phase space reconstruction (see Sec. 2.3). As we can see, the emittances appear to be higher along the beam edge and smaller at the beam center where the current was at its highest. Future gun simulations could prove useful to explain the cause of such emittance difference between the initial slices.

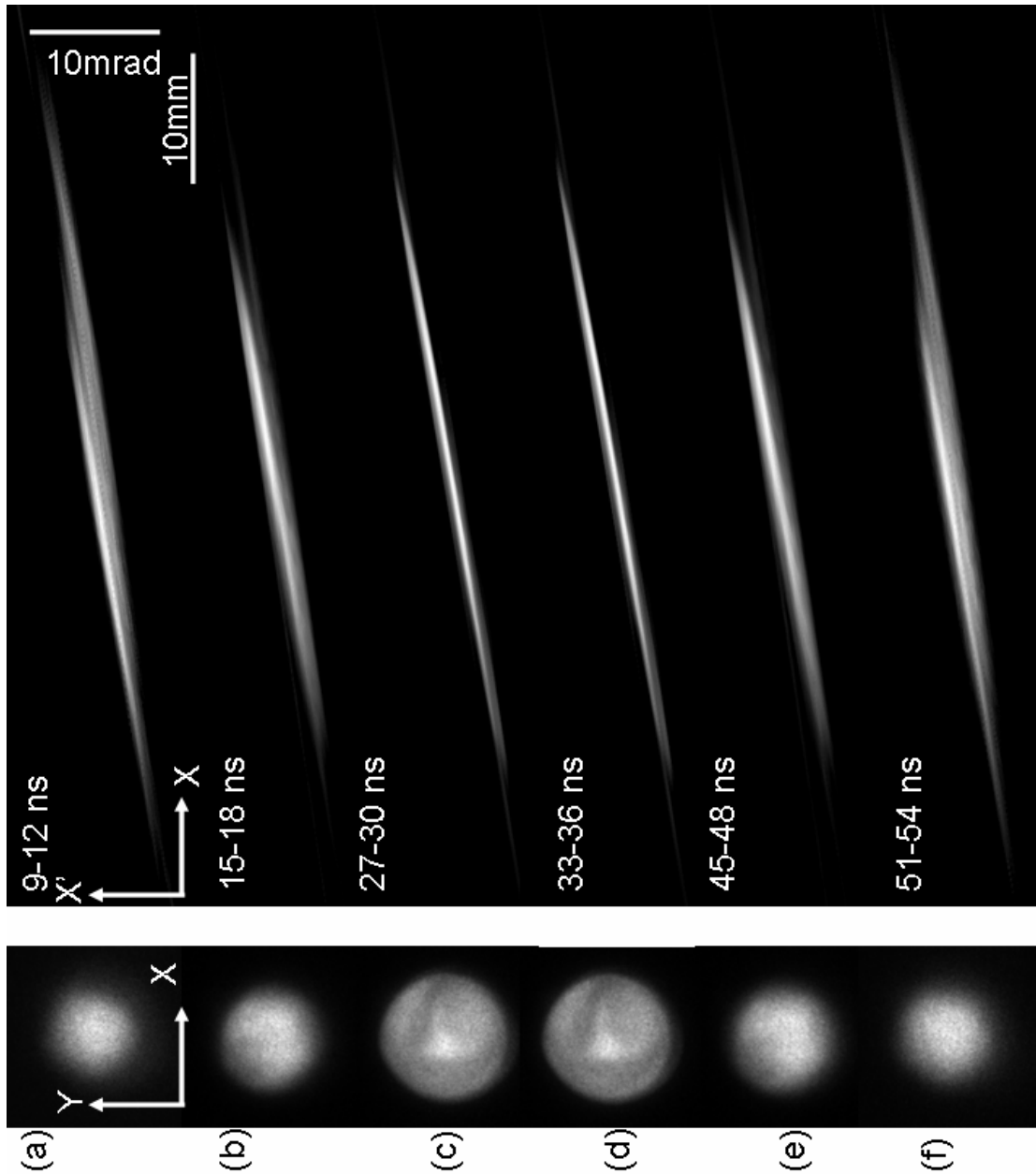


Figure 6.8: Beam in configuration space and in phase space for slices a, b, c, d, e, and f. Phase spaces are generated using the initial conditions shown in Table 6.2. Note that the slope of the phase space is not subtracted.

Figure 6.8 shows the beam distribution in configuration space for the six different slices. Clearly there is a difference in beam size and to illustrate this point in Fig. 6.9(a) we plot the measured beam size versus time. The right column of Fig. 6.8 shows the measured phase space by tomography. As in configuration space, the phase spaces do not look the same; however, they appear to be symmetric. Figure 6.9(b) shows the measured beam emittance. Comparing to Table 6.2 we see that all emittances at the screen are higher compared the one measured at the aperture. Furthermore, the emittances are higher at the edges relevant to the center. A similar trend was observed by measuring the transverse phase space and emittance at the exit of the SPARC photo-injector [36]. Another interesting observation is that not all the slices have the same orientation. To illustrate this point by using Eq. 4.4 we calculated the slope of the phase space distribution relevant to the spatial axis and plotted our results in Fig. 6.9 (c). We can see that the slices close to the edge are at higher slope. A possible reasoning for that could be the rapid variation of the beam current within this slice. Hence, the assumption of a constant, “average”, current within this slice by our tomography analysis may introduce some uncertainties in the measurement. Unfortunately, the camera gate cannot be reduced below 3 ns. However, future, simulation may prove useful to understand the causing of this effect better.

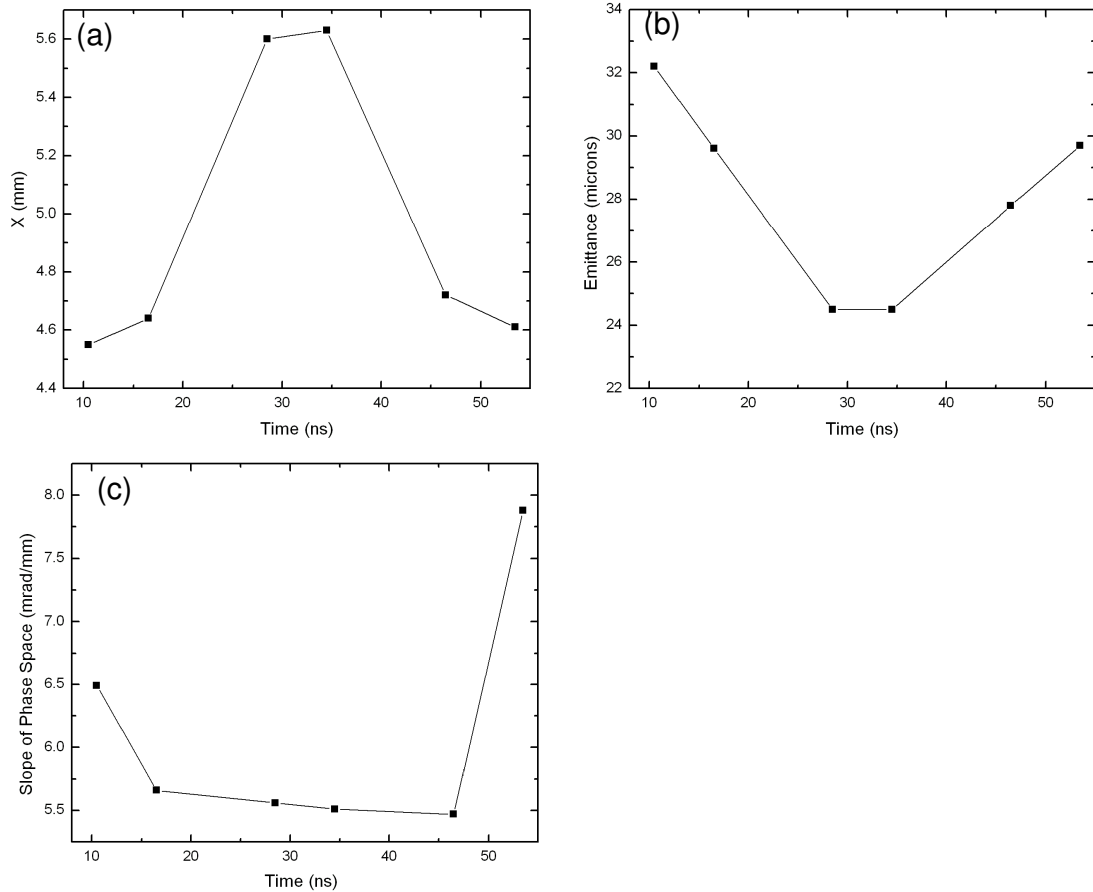


Figure 6.9: Beam parameters measured in the experiment: (a) Beam size; (b) Emittance; (c) Slope of phase space (from Eq. 4.4).

## 6.4 Conclusion

In this chapter we studied the coupling between longitudinal and transverse dynamics and were able for the first time to report slice tomography measurements for a beam with intense space-charge. Application of perturbations over the longitudinal flat top pulse lead to modifications on the beam transverse phase space distribution. Furthermore, using a parabolic pulse we showed that the emittance is

higher along the edges of the parabola. Future simulations may be useful to further understand this effect.

## Chapter 7 Summary and Conclusion

We reported in this dissertation the use of tomographic imaging algorithms to reconstruct the beam phase space for beams with intense space-charge.

In Chap. 2 we provided the theory of tomography and showed that it can be applied to beams by simply combining it with a quadruple scan. Tomography is making *no a priori* assumption about the beam distribution when the beam is emittance dominated. By assuming a uniform beam distribution and using a linear space-charge approximation we extended the diagnostic for beams with space-charge. Since the magnet focusing for beams with space-charge depends on the beam envelope  $X$  and  $Y$  (see Eq. 2.39 and 2.40), before doing our tomography analysis we first solved the beam envelope equations and get the exact dependence of  $X$  and  $Y$  with  $z$ . In our analysis we assumed that all particles move within the beam ellipse i.e.

$$\left(\frac{x}{X}\right)^2 + \left(\frac{y}{Y}\right)^2 < 1. \quad (7.1)$$

Of course this is not the case when halos are present and the analysis would be more accurate by allowing particles to evolve inside and outside this ellipse. One future model that can be implemented to account for this effect, is to introduce on the particle equations (see Eqs. 2.8, 2.39 and 2.40)

$$x'' + \kappa_{x0}x = \frac{2K}{X(X+Y)} F_x x, \quad (7.2)$$

$$y'' + \kappa_{y0}y = \frac{2K}{Y(X+Y)} F_y y, \quad (7.3)$$

the terms  $F_x F_y$  (which were assumed to be one in this dissertation) and are defined elsewhere [68]. Furthermore, the diagnostic is providing the 2D phase space  $(x, x')$  or  $(y, y')$ . Future work to reconstruct the 4D distribution  $(x, x', y, y')$ , for example with the use of skew quadrupoles, may reveal more details about the beam distribution.

In Chap. 3 we verified the accuracy of our tomography diagnostic by simulating the tomography diagnostic by using the particle-in-cell code WARP. We tested the diagnostic by using three beams with different intensity ( $\chi = 0.3, 0.72$  and  $0.9$ ). We showed that in all these cases tomography accurately maps the beam phase-space, with error less than 5% for the first two cases and error less than 8% for the third case. Furthermore, we tested our diagnostic by using more complex initial distributions in the code, for example by using a 5 beamlet initial distribution. We showed that by treating beams with non uniform distributions as equivalent (in rms sense) to uniform beams we can obtain very accurate phase space maps. This was true also when we used the five beamlet distribution. Even though such distribution will introduce non linear space-charge forces our linear model proves to be effective in the reconstruction process with an error less than 7%. Finally, we tested the effect of various errors (angular step, total phase space rotation, errors in the magnet current) in the reconstruction process. Our results showed that a close to  $180^\circ$  total rotation and a minimum angular step of  $14^\circ$  is necessary to accurately reconstruct the phase space. This error analysis was restricted to emittance dominated beams; however, future similar analysis for a space-charge dominated beam would be important.



In Chap. 4 we applied the diagnostic to experimentally study the phase-space evolution of beams with space-charge. Taking advantage of the intense beams and flexible design of UMER, in this chapter we applied our tomography diagnostic to a series of experiments to examine emittance growth, halo formation, phase mixing and charge homogenization. We use beams with different intensities and different transverse initial density distributions and compared our results with predictions from theory and simulations. Tomography accurately detects halo particles and this is a big success for the diagnostic since halos are in general difficult to detect (by aperturing diagnostics such as a pepper pot or slit scan) since their low intensity. Using an asymmetric aperture we generated a pattern of five merging beamlets and showed that whereas the beamlets appear to be merged in configuration space they remained distinct in velocity space  $\approx 0.76$  m downstream from the source. Tomographic emittance measurements on that location reveal an emittance growth of 1.1 which is in agreement with the theoretically predicted growth due to the conversion of the field energy to thermal kinetic energy. For the five beamlet experiment the beam had a lot of halo mostly arising from the gun cathode which was replaced, recently. Repeating this experiment, in the future, with the new cathode (without halo) and extracting data over longer distances (for instance RC 15, RC 16) may reveal more information about the beam evolution and relaxation. For example, recent simulation work predicts a different emittance growth process in a lattice with quadrupoles than solenoids. Hence, an interesting problem is to repeat the experiment and compare the emittance growth on UMER to that reported on a periodic focusing solenoidal channel [7]. Furthermore, study of the relaxation to equilibrium of beams with anisotropy is

another interesting problem. Anisotropy can be introduced by asymmetric focusing and the relaxation to equilibrium can be investigated by using tomography and measuring the beam emittance downstream. Repeating this experiment for beams with different intensity may reveal information about the relation between space-charge and equipartitioning. Furthermore, it can be used as a benchmark to relevant predictions from simulation [48].

In Chap. 5 we showed that tomography can equally well be applied to the case of solenoids. Comparing our reconstructed phase-spaces to that we got from simulations we found excellent agreement. Furthermore, we showed that care must be taken in the analysis for beams without axisymmetry and provided a step by step procedure to account for this effect. Finally, we showed that solenoids can cause emittance growth if the beam is large in size. Future, work extending the diagnostic to the case where acceleration is present will make the technique more suitable for ion injectors. Furthermore, our analysis was assuming that the beam was launched with zero angular velocity in a region with no magnetic fields. Future work generalizing the diagnostic to nonzero canonical angular momentum will make solenoidal tomography more efficient to the cases where a beam is born in regions with magnetic fields. Furthermore, since the LSE is occupied with a pepper-pot a direct comparison between tomography and pepper pot data would be another cross-check of the process.

Finally, in Chap. 6 we implemented fast imaging techniques to perform time resolved images (3ns) of the beam phase space distributions. Mainly, we studied two effects: (1) by introducing longitudinal density perturbations we investigated the

correlation between the transverse and longitudinal dynamics in configuration and phase space; (2) Applying a parabolic beam pulse and modeling so the beam profile of typical outputs of RF photocathode guns we tomographically mapped the beam phase-space along several slices and studied the orientation and emittances of those slices. We found significant differences between the slice emittance profiles as the beam propagates downstream. In the experiment the magnet scan and camera control was performed manually. Future automation of the process will facilitate more detailed study since it will allow more data within different slices or experimentation with different gate widths.

## Appendix A: MATLAB Tomography Codes

This appendix contains the MATLAB codes used in this dissertation to perform phase space tomography. Those were shortly described in Sec. 2.4. The codes are well-commented and so are listed below without detailed explanation. It should be pointed out that the analysis is only for the transverse axis  $x$  but the case is identical for the  $y$  axis, too.

### A1: Code for calculation of scaling factors and rotation angles

The main code `x_ScalF_RotA_Calc.m` is calculating the scaling factors and rotation angles by using Eq. 2.31 and Eq. 2.32. To do so it has to solve the beam envelope equations (Eq. 2.41 and Eq. 2.42) and for this reason calls the function 'EnvelopeSolver'. Furthermore, the code, in order to calculate the beam generalized Perveance, Focusing function and the total strength of the four magnets it calls the functions: 'Perveance', 'Quad\_Focusing', and 'MagnetsStrength', respectively.

Below are the details:

```
% Program x_ScalF_RotA_Calc.m
% SCALING FACTOR AND ROTATION ANGLE CALCULATOR
% Created by: Diktys Stratakis
%
% STEP 1 - Define Initial Beam Characteristics
%
clear all;
Ib=23.0/10^3; % Beam Current (A)
emit_x=30.0/10^6; % Beam Emittance in X (m)
emit_y=30.0/10^6; % Beam emittance in Y (m)
%
% STEP2 - Simulation Step Size
%
```

```

step_quad= 100; %steps inside each quad
step_drift=400; %steps between quads (drift regions)
%
% STEP 3a: Quadrupoles Characteristics & Locations (m)
%
Q1pos=0.08;
Q2pos=0.24;
Q3pos=0.40;
Q4pos=0.56;
leff=0.0372; % effective quadrupole length (m)
g=3.61*10^-2; % peak on axis gradient (G/(mA))
Zend=0.613;
L1=0.16-leff;
L2=0.16-leff;
L3=0.16-leff;
L4=Zend-Q4pos-leff/2;
%
% STEP 3b: Quadrupoles Currents (for reconstructed phase space)
%
Iquad=[-2.21,2.21,-2.21, 2.21];
%
% STEP 4: Initial Conditions on Beam Envelopes
X0=0.001375; % size in X (m)
XP0=-0.007270;% slope of envelope (rad)
Y0=0.001365; % size in Y (m)
YP0=0.007107; % slope of envelope (rad)
%
% STEP 5: Solution of Beam Envelope Equations
%
parameters=[emit_x,emit_y,Ib,Iquad,leff,g,Q1pos,Q2pos,Q3pos,Q4pos];
[t,y]=ode23(@KV_EnvelopeSolver,[0,Zend],[X0,XP0,Y0,YP0],[],parameters);
all_data=[t,y];
all_z=all_data(:,1);
all_x=all_data(:,2);
all_xp=all_data(:,3);
all_y=all_data(:,4);
all_yp=all_data(:,5);
%
%STEP 6: Matrix Analysis
%Quad 1
%
clear ii
for ii=1:step_quad
l=leff/step_quad;
z_q1=Q1pos-leff/2+(ii-1)*l;

```

```

x_q1=interp1(all_z,all_x,z_q1,'spline');
y_q1=interp1(all_z,all_y,z_q1,'spline');
kappa_q1=Quad_Focusing(Iquad(1),g)-(2*Perveance(Ib))/(x_q1*(x_q1+y_q1));
%Focusing function (Eq. 2.39)
if Iquad(1) > 0
    M_q1{ii}=[cos(sqrt(kappa_q1)*l) (1/sqrt(kappa_q1))*(sin(sqrt(kappa_q1)*l)); -
sqrt(kappa_q1)*(sin(sqrt(kappa_q1)*l)) cos(sqrt(kappa_q1)*l)];
elseif Iquad(1) < 0
    M_q1{ii}=[cos(sqrt(kappa_q1)*l) (1/sqrt(kappa_q1))*(sin(sqrt(kappa_q1)*l)); -
sqrt(kappa_q1)*(sin(sqrt(kappa_q1)*l)) cos(sqrt(kappa_q1)*l)];
else
    M_q1{ii}=[1 l;0 1];
end
end
clear jj
M_q1_com=eye(2);
for jj=step_quad:-1:1
    M_q1_com=M_q1_com*M_q1{jj};
end
%
%Drift between Quad1 and Quad2
for iii=1:step_drift
ld=L1/step_drift;
z_dr12=Q1pos+leff/2+(iii-1)*ld;
x_dr12=interp1(all_z,all_x,z_dr12,'spline');
y_dr12=interp1(all_z,all_y,z_dr12,'spline');
kappa_dr12=(-2*Perveance(Ib))/(x_dr12*(x_dr12+y_dr12));
M_dr12{iii}=[cos(sqrt(kappa_dr12)*ld)
(1/sqrt(kappa_dr12))*(sin(sqrt(kappa_dr12)*ld)); -
sqrt(kappa_dr12)*(sin(sqrt(kappa_dr12)*ld)) cos(sqrt(kappa_dr12)*ld)];
end
M_dr12_com=eye(2);
for jjj=step_drift:-1:1
    M_dr12_com=M_dr12_com*M_dr12{jjj};
end
%
% Quad 2
%
clear ii
for ii=1:step_quad
l=leff/step_quad;
z_q2=Q2pos-leff/2+(ii-1)*l;
x_q2=interp1(all_z,all_x,z_q2,'spline');
y_q2=interp1(all_z,all_y,z_q2,'spline');
kappa_q2=Quad_Focusing(Iquad(2),g)-(2*Perveance(Ib))/(x_q2*(x_q2+y_q2));

```

```

if Iquad(2) > 0
    M_q2{ii}=[cos(sqrt(kappa_q2)*l) (1/sqrt(kappa_q2))*(sin(sqrt(kappa_q2)*l)); -
sqrt(kappa_q2)*(sin(sqrt(kappa_q2)*l)) cos(sqrt(kappa_q2)*l)];
elseif Iquad(2) < 0
    M_q2{ii}=[cos(sqrt(kappa_q2)*l) (1/sqrt(kappa_q2))*(sin(sqrt(kappa_q2)*l)); -
sqrt(kappa_q2)*(sin(sqrt(kappa_q2)*l)) cos(sqrt(kappa_q2)*l)];
else
    M_q2{ii}=[1 l;0 l];
end
end
clear jj
M_q2_com=eye(2);
for jj=step_quad:-1:1
    M_q2_com=M_q2_com*M_q2{jj};
end
%
% Drift between Quad2 and Quad3
%
for iii=1:step_drift
ld=L1/step_drift;
z_dr23=Q2pos+leff/2+(iii-1)*ld;
x_dr23=interp1(all_z,all_x,z_dr23,'spline');
y_dr23=interp1(all_z,all_y,z_dr23,'spline');
kappa_dr23=-(2*Perveance(Ib))/(x_dr23*(x_dr23+y_dr23));
M_dr23{iii}=[cos(sqrt(kappa_dr23)*ld)
(1/sqrt(kappa_dr23))*(sin(sqrt(kappa_dr23)*ld)); -
sqrt(kappa_dr23)*(sin(sqrt(kappa_dr23)*ld)) cos(sqrt(kappa_dr23)*ld)];
end
M_dr23_com=eye(2);
for jjj=step_drift:-1:1
    M_dr23_com=M_dr23_com*M_dr23{jjj};
end
%
% Quad 3
%
clear ii
for ii=1:step_quad
l=leff/step_quad;
z_q3=Q3pos-leff/2+(ii-1)*l;
x_q3=interp1(all_z,all_x,z_q3,'spline');
y_q3=interp1(all_z,all_y,z_q3,'spline');
kappa_q3=Quad_Focusing(Iquad(3),g)-(2*Perveance(Ib))/(x_q3*(x_q3+y_q3));
if Iquad(3) > 0
    M_q3{ii}=[cos(sqrt(kappa_q3)*l) (1/sqrt(kappa_q3))*(sin(sqrt(kappa_q3)*l)); -
sqrt(kappa_q3)*(sin(sqrt(kappa_q3)*l)) cos(sqrt(kappa_q3)*l)];

```

```

elseif Iquad(3) < 0
    M_q3{ii}=[cos(sqrt(kappa_q3)*l) (1/sqrt(kappa_q3))*(sin(sqrt(kappa_q3)*l)); -
sqrt(kappa_q3)*(sin(sqrt(kappa_q3)*l)) cos(sqrt(kappa_q3)*l)];
else
    M_q3{ii}=[1 l;0 l];
end
end
clear jj
M_q3_com=eye(2);
for jj=step_quad:-1:1
    M_q3_com=M_q3_com*M_q3{jj};
end
%
% Drift between Quad3 and Quad4
%
for iii=1:step_drift
ld=L1/step_drift;
z_dr34=Q3pos+leff/2+(iii-1)*ld;
x_dr34=interp1(all_z,all_x,z_dr34,'spline');
y_dr34=interp1(all_z,all_y,z_dr34,'spline');
kappa_dr34=-(2*Perveance(Ib))/(x_dr34*(x_dr34+y_dr34));
M_dr34{iii}=[cos(sqrt(kappa_dr34)*ld)
(1/sqrt(kappa_dr34))*(sin(sqrt(kappa_dr34)*ld)); -
sqrt(kappa_dr34)*(sin(sqrt(kappa_dr34)*ld)) cos(sqrt(kappa_dr34)*ld)];
end
M_dr34_com=eye(2);
for jjj=step_drift:-1:1
    M_dr34_com=M_dr34_com*M_dr34{jjj};
end
%
% Quad 4
%
clear ii
for ii=1:step_quad
l=leff/step_quad;
z_q4=Q4pos-leff/2+(ii-1)*l;
x_q4=interp1(all_z,all_x,z_q4,'spline');
y_q4=interp1(all_z,all_y,z_q4,'spline');
kappa_q4=Quad_Focusing(Iquad(4),g)-(2*Perveance(Ib))/(x_q4*(x_q4+y_q4));
if Iquad(4) > 0
    M_q4{ii}=[cos(sqrt(kappa_q4)*l) (1/sqrt(kappa_q4))*(sin(sqrt(kappa_q4)*l)); -
sqrt(kappa_q4)*(sin(sqrt(kappa_q4)*l)) cos(sqrt(kappa_q4)*l)];
elseif Iquad(4) < 0
    M_q4{ii}=[cos(sqrt(kappa_q4)*l) (1/sqrt(kappa_q4))*(sin(sqrt(kappa_q4)*l)); -
sqrt(kappa_q4)*(sin(sqrt(kappa_q4)*l)) cos(sqrt(kappa_q4)*l)];

```



```

else
    M_q4{ii}=[1 1;0 1];
end
end
clear jj
M_q4_com=eye(2);
for jj=step_quad:-1:1
    M_q4_com=M_q4_com*M_q4{jj};
end
%
% Drift between Quad4 and Screen
%
for iii=1:step_drift
    ld4=L4/step_drift;
    z_dr4=Q4pos+leff/2+(iii-1)*ld4;
    x_dr4=interp1(all_z,all_x,z_dr4,'spline');
    y_dr4=interp1(all_z,all_y,z_dr4,'spline');
    kappa_dr4=-(2*Perveance(Ib))/(x_dr4*(x_dr4+y_dr4));
    M_dr4{iii}=[cos(sqrt(kappa_dr4)*ld4)
    (1/sqrt(kappa_dr4))*(sin(sqrt(kappa_dr4)*ld4)); -
    sqrt(kappa_dr4)*(sin(sqrt(kappa_dr4)*ld4)) cos(sqrt(kappa_dr4)*ld4)];
end
M_dr4_com=eye(2);
for jjj=step_drift:-1:1
    M_dr4_com=M_dr4_com*M_dr4{jjj};
end
%
%STEP 7 Trasport Matrix for Default Phase Space
%
M=M_dr4_com*M_q4_com*M_dr34_com*M_q3_com*M_dr23_com*M_q2_com*
M_dr12_com*M_q1_com;
%
%STEP 8 - Gives me the sizes of the "matched" beam on the phosphor screen
%as predicted by the envelopes
z_end=Zend;
x0_end=interp1(all_z,all_x,z_end,'spline')
y0_end=interp1(all_z,all_y,z_end,'spline')
xp0_end=interp1(all_z,all_xp,z_end,'spline')
yp0_end=interp1(all_z,all_yp,z_end,'spline')
%STEP 8 Read current values from quadrupole scans (should be a txt file)
%
Data=dlmread('C:\Documents and
Settings\ldstratak\Desktop\x_ScF_RtA_Pencil_Matched.txt');
Iquad1=Data(:,1);
Iquad2=Data(:,2);

```

```

Iquad3=Data(:,3);
Iquad4=Data(:,4);
%
%STEP 9 Repeat same procedure again...
%
npoints=length(Iquad1); % Number of total scans
for h=1:npoints
Iquad_new=[Iquad1(h),Iquad2(h),Iquad3(h),Iquad4(h)]; %Read the currents of the
magnets that we scanned for Tomography
parameters=[emit_x,emit_y,Ib,Iquad_new,leff,g,Q1pos,Q2pos,Q3pos,Q4pos];
[t,y]=ode23(@KV_EnvelopeSolver,[0,Zend],[X0,XP0,Y0,YP0],[],parameters);
all_data=[t,y];
all_z=all_data(:,1);
all_x=all_data(:,2);
all_y=all_data(:,4);
%
%Quad 1
%
for ii=1:step_quad
l=leff/step_quad;
z_q1=Q1pos-leff/2+(ii-1)*l;
x_q1=interp1(all_z,all_x,z_q1,'spline');
y_q1=interp1(all_z,all_y,z_q1,'spline');
kappa_q1=Quad_Focusing(Iquad_new(1),g)-(2*Perveance(Ib))/(x_q1*(x_q1+y_q1));
if Iquad_new(1) > 0
M_q1{ii}=[cos(sqrt(kappa_q1)*l) (1/sqrt(kappa_q1))*(sin(sqrt(kappa_q1)*l)); -
sqrt(kappa_q1)*(sin(sqrt(kappa_q1)*l)) cos(sqrt(kappa_q1)*l)];
elseif Iquad_new(1) < 0
M_q1{ii}=[cos(sqrt(kappa_q1)*l) (1/sqrt(kappa_q1))*(sin(sqrt(kappa_q1)*l)); -
sqrt(kappa_q1)*(sin(sqrt(kappa_q1)*l)) cos(sqrt(kappa_q1)*l)];
else
M_q1{ii}=[1 l;0 1];
end
end
M_q1_com=eye(2);
for jj=step_quad:-1:1
M_q1_com=M_q1_com*M_q1{jj};
end
M_q1_com2{h}=M_q1_com;
%
%Drift between Quad1 and Quad2
for iii=1:step_drift
ld=L1/step_drift;
z_dr12=Q1pos+leff/2+(iii-1)*ld;
x_dr12=interp1(all_z,all_x,z_dr12,'spline');

```

```

y_dr12=interp1(all_z,all_y,z_dr12,'spline');
kappa_dr12=-(2*Perveance(Ib))/(x_dr12*(x_dr12+y_dr12));
M_dr12{iii}=[cos(sqrt(kappa_dr12)*ld)
(1/sqrt(kappa_dr12))*(sin(sqrt(kappa_dr12)*ld)); -
sqrt(kappa_dr12)*(sin(sqrt(kappa_dr12)*ld) cos(sqrt(kappa_dr12)*ld)];
end
M_dr12_com=eye(2);
for jjj=step_drift:-1:1
    M_dr12_com=M_dr12_com*M_dr12{jjj};
end
M_dr12_com2{h}=M_dr12_com;
%
% Quad 2
%
for ii=1:step_quad
l=leff/step_quad;
z_q2=Q2pos-leff/2+(ii-1)*l;
x_q2=interp1(all_z,all_x,z_q2,'spline');
y_q2=interp1(all_z,all_y,z_q2,'spline');
kappa_q2=Quad_Focusing(Iquad_new(2),g)-(2*Perveance(Ib))/(x_q2*(x_q2+y_q2));
    if Iquad_new(2) > 0
        M_q2{ii}=[cos(sqrt(kappa_q2)*l) (1/sqrt(kappa_q2))*(sin(sqrt(kappa_q2)*l)); -
sqrt(kappa_q2)*(sin(sqrt(kappa_q2)*l) cos(sqrt(kappa_q2)*l)];
    elseif Iquad_new(2) < 0
        M_q2{ii}=[cos(sqrt(kappa_q2)*l) (1/sqrt(kappa_q2))*(sin(sqrt(kappa_q2)*l)); -
sqrt(kappa_q2)*(sin(sqrt(kappa_q2)*l) cos(sqrt(kappa_q2)*l)];
    else
        M_q2{ii}=[1 l;0 1];
    end
end
M_q2_com=eye(2);
for jj=step_quad:-1:1
    M_q2_com=M_q2_com*M_q2{jj};
end
M_q2_com2{h}=M_q2_com;
%
% Drift between Quad2 and Quad3
%
for iii=1:step_drift
ld=L1/step_drift;
z_dr23=Q2pos+leff/2+(iii-1)*ld;
x_dr23=interp1(all_z,all_x,z_dr23,'spline');
y_dr23=interp1(all_z,all_y,z_dr23,'spline');
kappa_dr23=-(2*Perveance(Ib))/(x_dr23*(x_dr23+y_dr23));

```

```

M_dr23{iii}=[cos(sqrt(kappa_dr23)*ld)
(1/sqrt(kappa_dr23))*(sin(sqrt(kappa_dr23)*ld)); -
sqrt(kappa_dr23)*(sin(sqrt(kappa_dr23)*ld)) cos(sqrt(kappa_dr23)*ld)];
end
M_dr23_com=eye(2);
for jjj=step_drift:-1:1
    M_dr23_com=M_dr23_com*M_dr23{jjj};
end
M_dr23_com2{h}=M_dr23_com;
%
% Quad 3
%
for ii=1:step_quad
l=leff/step_quad;
z_q3=Q3pos-leff/2+(ii-1)*l;
x_q3=interp1(all_z,all_x,z_q3,'spline');
y_q3=interp1(all_z,all_y,z_q3,'spline');
kappa_q3=Quad_Focusing(Iquad_new(3),g)-(2*Perveance(Ib))/(x_q3*(x_q3+y_q3));
if Iquad_new(3) > 0
    M_q3{ii}=[cos(sqrt(kappa_q3)*l) (1/sqrt(kappa_q3))*(sin(sqrt(kappa_q3)*l)); -
sqrt(kappa_q3)*(sin(sqrt(kappa_q3)*l)) cos(sqrt(kappa_q3)*l)];
elseif Iquad_new(3) < 0
    M_q3{ii}=[cos(sqrt(kappa_q3)*l) (1/sqrt(kappa_q3))*(sin(sqrt(kappa_q3)*l)); -
sqrt(kappa_q3)*(sin(sqrt(kappa_q3)*l)) cos(sqrt(kappa_q3)*l)];
else
    M_q3{ii}=[1 l;0 l];
end
end
M_q3_com=eye(2);
for jj=step_quad:-1:1
    M_q3_com=M_q3_com*M_q3{jj};
end
M_q3_com2{h}=M_q3_com;
%
% Drift between Quad3 and Quad4
%
for iii=1:step_drift
ld=L1/step_drift;
z_dr34=Q3pos+leff/2+(iii-1)*ld;
x_dr34=interp1(all_z,all_x,z_dr34,'spline');
y_dr34=interp1(all_z,all_y,z_dr34,'spline');
kappa_dr34=-(2*Perveance(Ib))/(x_dr34*(x_dr34+y_dr34));
M_dr34{iii}=[cos(sqrt(kappa_dr34)*ld)
(1/sqrt(kappa_dr34))*(sin(sqrt(kappa_dr34)*ld)); -
sqrt(kappa_dr34)*(sin(sqrt(kappa_dr34)*ld)) cos(sqrt(kappa_dr34)*ld)];

```

```

end
M_dr34_com=eye(2);
for jjj=step_drift:-1:1
    M_dr34_com=M_dr34_com*M_dr34{jjj};
end
M_dr34_com2{h}=M_dr34_com;
%
% Quad 4
%
for ii=1:step_quad
    l=leff/step_quad;
    z_q4=Q4pos-leff/2+(ii-1)*l;
    x_q4=interp1(all_z,all_x,z_q4,'spline');
    y_q4=interp1(all_z,all_y,z_q4,'spline');
    kappa_q4=Quad_Focusing(Iquad_new(4),g)-(2*Perveance(Ib))/(x_q4*(x_q4+y_q4));
    if Iquad_new(4) > 0
        M_q4{ii}=[cos(sqrt(kappa_q4)*l) (1/sqrt(kappa_q4))*(sin(sqrt(kappa_q4)*l)); -
sqrt(kappa_q4)*(sin(sqrt(kappa_q4)*l)) cos(sqrt(kappa_q4)*l)];
    elseif Iquad_new(4) < 0
        M_q4{ii}=[cos(sqrt(kappa_q4)*l) (1/sqrt(kappa_q4))*(sin(sqrt(kappa_q4)*l)); -
sqrt(kappa_q4)*(sin(sqrt(kappa_q4)*l)) cos(sqrt(kappa_q4)*l)];
    else
        M_q4{ii}=[1 l;0 1];
    end
end
M_q4_com=eye(2);
for jj=step_quad:-1:1
    M_q4_com=M_q4_com*M_q4{jj};
end
M_q4_com2{h}=M_q4_com;
%
% Drift between Quad4 and Screen
%
for iii=1:step_drift
    ld4=L4/step_drift;
    z_dr4=Q4pos+leff/2+(iii-1)*ld4;
    x_dr4=interp1(all_z,all_x,z_dr4,'spline');
    y_dr4=interp1(all_z,all_y,z_dr4,'spline');
    kappa_dr4=-(2*Perveance(Ib))/(x_dr4*(x_dr4+y_dr4));
    M_dr4{iii}=[cos(sqrt(kappa_dr4)*ld4)
(1/sqrt(kappa_dr4))*(sin(sqrt(kappa_dr4)*ld4)); -
sqrt(kappa_dr4)*(sin(sqrt(kappa_dr4)*ld4)) cos(sqrt(kappa_dr4)*ld4)];
end
M_dr4_com=eye(2);
for jjj=step_drift:-1:1

```

```

    M_dr4_com=M_dr4_com*M_dr4{jjj};
end
M_dr4_com2{h}=M_dr4_com;
%
%STEP 10 Calculate scaling factors & rotation angles for each scan
%
M1=M_dr4_com2{h}*M_q4_com2{h}*M_dr34_com2{h}*M_q3_com2{h}*M_dr2
3_com2{h}*M_q2_com2{h}*M_dr12_com2{h}*M_q1_com2{h}*inv(M); %Net
Transport matrix
%It's basically Eq. 2.46
scaling_factor{h}=sqrt(M1(1,1)*M1(1,1)+M1(1,2)*M1(1,2)); %This is Eq. 2.31
rotation_angle{h}=atan(M1(1,2)/M1(1,1))*(180/pi); %This is Eq. 2.32
end
%
%STEP 11: Finally Save Data into a .txt file
%
clear d
fid = fopen('x_ScRt_Pencil.txt','w');
for i=1:length(scaling_factor)
fprintf(fid,'%f
',Iquad1(i),Iquad2(i),Iquad3(i),Iquad4(i),scaling_factor{i},rotation_angle{i});
fprintf(fid,'\n');
end
fclose(fid);
type x_ScRt_Pencil.txt;

```

\*\*\*\*\*

```

function dy=EnvelopeSolver(t,y,parameters)
%This program solves the KV Beam Envelope Equations from Eq. 2.41 and Eq. 2.42
emit_x=parameters(1);
emit_y=parameters(2);
Ib=parameters(3);
Iquad=parameters(4:7);
leff=parameters(8);
g=parameters(9);
Q1pos=parameters(10);
Q2pos=parameters(11);
Q3pos=parameters(12);
Q4pos=parameters(13);
kappa=Quad_Focusing(Iquad,g);
K=Perveance(Ib);
dy(1)=y(2);

```

```

dy(2)=-
MagnetsStrength(t,leff,Iquad,kappa,Q1pos,Q2pos,Q3pos,Q4pos)*y(1)+(emit_x^2)/y(
1)^3+2*K/(y(1)+y(3));
dy(3)=y(4);
dy(4)=MagnetsStrength(t,leff,Iquad,kappa)*y(3)+(emit_y^2)/y(3)^3+2*K/(y(3)+y(1))
;
dy=[dy(1);dy(2);dy(3);dy(4)];

```

```

*****
function Strength=MagnetsStrength(t,leff,Iquad,kappa,Q1pos,Q2pos,Q3pos,Q4pos)
%This function calculates the magnet strength of each magnet along the beam line
Q1pos=0.08;
Q2pos=0.24;
Q3pos=0.40;
Q4pos=0.56;
if t >= Q1pos-leff/2 & t<=Q1pos+leff/2
    Strength =kappa(1,1);
elseif t>=Q2pos-leff/2 & t<=Q2pos+leff/2
    Strength =kappa(1,2);
elseif t>=Q3pos-leff/2 & t<=Q3pos+leff/2
    Strength =kappa(1,3);
elseif t>=Q4pos-leff/2 & t<=Q4pos+leff/2
    Strength =kappa(1,4);
else
    Strength=0;
end

```

```

*****
function kappa=Quad_Focusing(Iquad,g)
%This function calculates the focusing function of the quadrupole according
%to Eq. 2.5
c=2.9979*10^8;
m=9.109/10^31;
q=1.602/10^19;
e0=8.854/10^12;
i0=4*pi*e0*m*c^3/q;
T=10*q*10^3; %Beam Energy in eV
gamma=T/(m*c^2)+1;
beta=sqrt(1-1/gamma^2);
kappa=g*Iquad*q/(m*c*beta*gamma);

```

```

*****
function K=Perveance(Ib)
%This program calculates the beam generalized perveance according to Eq. 2.9
c=2.9979*10^8;

```

```

m=9.109/10^31;
q=1.602/10^19;
e0=8.854/10^12;
i0=4*pi*e0*m*c^3/q;
T=10*q*10^3; %Beam Energy
gamma=T/(m*c^2)+1;
beta=sqrt(1-1/gamma^2);
K=(2*Ib/i0)*1/(beta*gamma)^3; %Beam Perveance

```

## A2: Code to calculate beam size, beam envelope slope and emittance

```

% Program EmitCalc.m
% Emittance Calculator
% Created by: Diktys Stratakis
%
%This program calculates the beam emittance, beam size and slope of the envelope
from
%the reconstructed phase-space
%
clear all;
Jold=imread('yyp_11mA_4keV_cs34_a.bmp'); %Read Beam Photo
J = Jold(:,:,1);
for Bkgr=0:10 % subtract background
J(J<Bkgr)=0.0;
Screen_Radius=886 % Screen Radius in pixels
T=31.75/Screen_Radius; %mm per pixel; 31.75mm is the radius, in mm, of our
screen
Hor_Size = size(J, 2); % # of pix horizontally
Ver_Size = size(J, 1); % # of pix vertically
% -- Calculate Moments
ixc = 0; iyc = 0; % Centroids in pixels
xrms = 0; yrms = 0; xymom = 0; % 2nd moments in pixels
for ix = 1:Hor_Size
for iy = 1:Ver_Size
ixc = ixc + ix*double(J(iy,ix));
iyc = iyc + iy*double(J(iy,ix));
xrms = xrms + (ix^2)*double(J(iy,ix));
yrms = yrms + (iy^2)*double(J(iy,ix));
xymom = xymom + (ix*iy)*double(J(iy,ix));
end
end
INT =sum(sum(J)); % Total Intensity (Eq. 2.47)
iix = (ixc/INT); iiy= (iyc/INT); % Centroid
xrms = 1*T*sqrt((xrms/INT)-(iix^2)); % Envelope

```



```

yrms = 1*T*sqrt((yrms/INT)-(iyy^2));
xymom = (T^2)*((xymom/INT)-(iix*iyy)); % Angle

X_envelope(Bkgr+1)=2*xrms; %units are mm
Xp(Bkgr+1)=4*xymom/X_envelope(Bkgr+1);% Beam Slope of Envelope (in mrad)
emittance(Bkgr+1)=4*sqrt((xrms^2)*(yrms^2)-xymom^2) %(in μm); This is 4xrms
emittance
%Twiss Parameters
beta(Bkgr+1)=xrms^2/(emittance(Bkgr+1)/4);
gama(Bkgr+1)=yrms^2/(emittance(Bkgr+1)/4);
alpha(Bkgr+1)=sqrt(beta(Bkgr+1)*gama(Bkgr+1)-1);

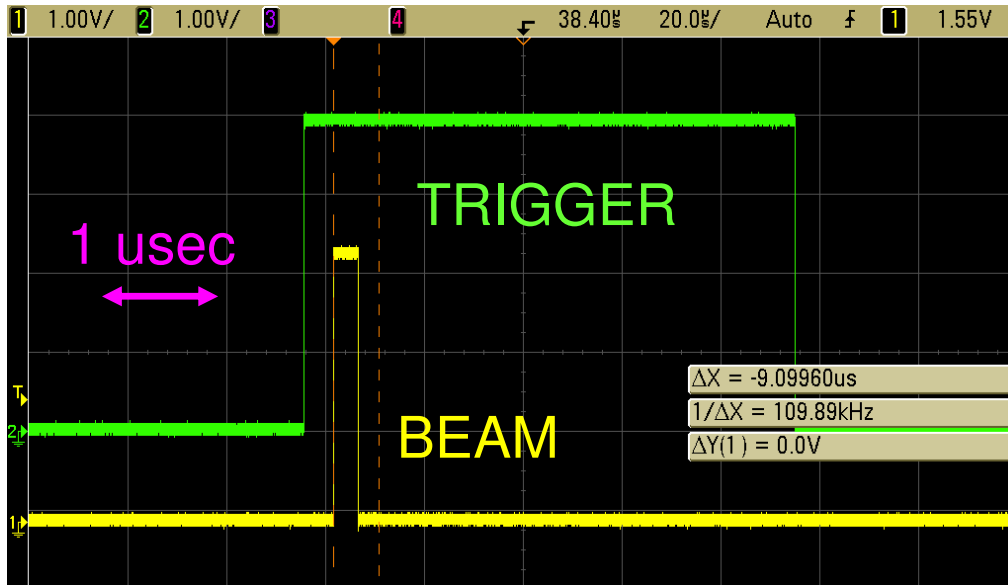
slope(Bkgr+1)=-alpha(Bkgr+1)/beta(Bkgr+1); % This is the beam slope (Eq. 4.4)
end

```

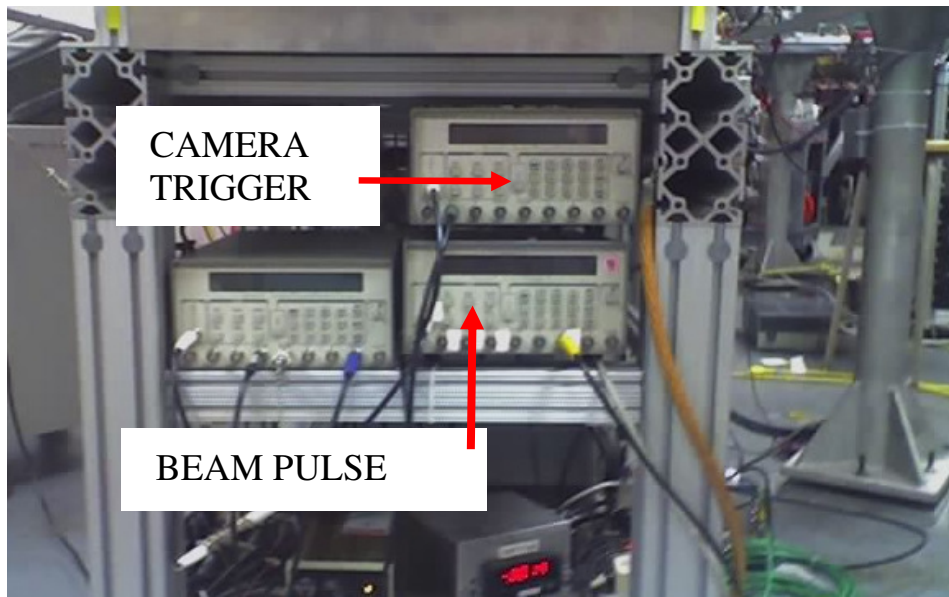
## Appendix B: Camera Operating Procedures

Here we will list the precautions that we have to take in order to successfully operate the camera, control hardware and imaging software.

- An external trigger must be applied to synchronize the camera gate to the beam pulse by using the pulse generator shown in Fig. B.1(b). The camera gate opens when the trigger arrives. The gate closure is determined by the exposure time set by XCAP. A good practice is to set it as low as possible to maximize the signal to noise ratio.
- The trigger has to be applied 5  $\mu\text{s}$  ahead the beam pulse and has to be at least 100  $\mu\text{s}$  long. The trigger and beam pulse reading at the scope is illustrated in Fig. B.1(a).
- The camera has a read out time of 33 msec. Therefore trigger frequency cannot exceed 1000/33 Hz.



(a)



(b)

B.1: External trigger application: (a) Scope reading; (b) Pulsers that control camera and beam on UMER

## Appendix C: XCAP Automation

As shown in Sec. 4.3.4 XCAP can be thought as a slave of Labview. In other words, it performs an action (captures a beam photo) only if Labview instructs it (by sending a text message). In this section we describe the procedure we use to make XCAP such a slave. The idea is the following: In XCAP you first create two scripts to carry out a loop. One script ('loop.scr') will contain the body of the loop. Another script ('setup.scr') will set up XCAP, and will perform the loop N times (where N equals the number of photos you are interested to take).

'Setup.scr' will do the following:

- A) By assuming that the beam and the camera are turned on, it will activate the sequence capture window in XCAP.
- B) Activate the RS-232 Control window so that XCAP can communicate with Labview in the magnet control computer.
- C) Run script 'loop.scr', the body of the loop.

The 'loop.scr' will do the following:

- 1) Capture a beam photo when it receives the text message from Labview via RS-232
- 2) Increment the single buffer that the sequence capture will record to, so that the next time the loop is executed, the image will be stored in the next frame buffer.
- 3) Open COM port in RS-232 control and enable communication between XCAP and Labview.
- 4) Send a confirmation signal to the magnet control computer via RS-232 signal.
- 5) Close COM port in RS-232 Control.
- 6) Repeat steps 1-5 until all photos where captured

In order to create those scripts in XCAP we have to do step by step the following procedure. Note that this procedure needs to be done once. First, we create a temporary "loop.scr" file:

1. From the Scripts menu in XCAP, select "Script Record".
2. Click Browse, and save to file loop.scr, then click Accept.
3. Click Record.
4. Click Stop.
5. Close "Script Record" window.

When setup.scr runs, it will run in a "Script Play" window. When it plays 'loop.scr', it will open a second script play window. So, you will need to record 'setup.scr' in the same environment as when 'setup.scr' is run:

6. From the Scripts menu, select "Script Play".

Now to record setup.scr:

7. Select "Script Record" from the Scripts menu.
8. Click Browse, save to file setup.scr, then click Accept.
9. Click Record.

Now to set up the sequence capture. You will be capturing a single image, and you want the first image to be saved to buffer 0. You also need to set up the RS-232 event start parameters:

10. From the Capture menu, select "Sequence Capture: Video to Frame Buffers".
11. Uncheck "Start/End All Buffers".
12. Select "Event Start".
13. Select the "Capture Event" tab.
14. Select "RS-232" as the event type.
15. For "RS-232 Port", select the COM port you will be using.
16. Set up the other RS-232 Port options as required.

Now to open and set up the RS-232 Control window:

17. From the Utility menu, select "RS-232 Control".
18. Select Setup from the Controls menu, and set up the RS-232 port parameters as required. Make sure "RS-232 Port" remains set to "None - Disabled".

Next you will have to open and set up the Black Board, so that cell A0A0 starts out containing the first buffer you wish to capture to (buffer 0):

19. From the Utility menu, select "Black Board".
20. Left click on cell A0A0, and set A0A0=0.

The next step will be to execute the body of the loop, 200 times:

21. From the Scripts menu, select "Script Play".
22. Click Browse, and browse for loop.scr. Click Accept.
23. Set "Repeat Script Count" to 200.

24. Click Play.

Now, you are done recording setup.scr:

25. In the "Script Record" window, click Stop.

26. Close the "Script Record" window.

Finally, before you record loop.scr, you will have to close the Script

Play window that was opened in step 6 above:

27. Close the "Script Play" window.

Next, you will be recording the body of the loop:

28. From the Scripts menu, select "Script Record".

29. Click Browse, save to file loop.scr, then click Accept.

30. Click Record.

Next, you will want to set the sequence capture window so that a sequence of length one is recorded, into the buffer that matches the number in black board cell A0A0:

31. In the "Video to Frame Buffers" window, right click in the "Starting Frame Buffer" box.

32. Select "BlackBoard Read".

33. In the "Starting Frame Buffer" box, type "BB Read=A0A0", and hit Enter.

34. Right click in the "Starting Frame Buffer" box and select "Key Entry".

35. Right click in the "Ending Frame Buffer" box.

36. Select "BlackBoard Read".

37. In the "Ending Frame Buffer" box, type "BB Read=A0A0", and hit Enter.
38. Right click in the "Ending Frame Buffer" box and select "Key Entry".

Now, you will want to record the sequence:

39. In the "Video to Frame Buffers" window, click Record.
40. Send a RS-232 signal (text message) with LabView from the linux computer.
41. Wait for the sequence capture to finish (only 1 image will be captured).

Next, you will want to increment the number in black board cell A0A0, so that the next time the loop plays, the sequence will be captured into the next frame buffer. To do this, you will write the current frame buffer to black board cell A0A1, and then set black board cell A0A0 to A0A1+1:

42. In the "Video to Frame Buffers" window, right click in the "Starting Frame Buffer" box.
43. Select "BlackBoard Write".
44. In the "Starting Frame Buffer" box, type "BB Write=A0A1", and hit Enter.
45. Right click in the "Starting Frame Buffer" box and select "Key Entry".
46. In the "Black Board" window, left click on cell A0A0, and set  $A0A0=A0A1+1$

Next, you will want to enable the RS-232 port in "RS-232 Control", send the RS-232 signal, and then disable the RS-232 port:

47. In the "RS-232 Control" window, set "RS-232 Port" to whichever COM



port you will be using.

48. In the "XMT String" box, type the string you want to send.

49. Click "ReXMT String".

50. Set "RS-232 Port" to "None - Disabled".

You are now done recording loop.scr:

51. In the "Script Record" window, click Stop.

52. Close the "Script Record" window.

Now, when you just run setup.scr by selecting "Script Play" from the Scripts menu, the setup script will set up XCAP and then perform the loop (loop.scr) whenever it gets instructed by Labview.

## Bibliography

- [1] J. Wei, Y.Y. Lee, D. Raparia, J. Sandberg, J. Tuozzolo, and W.T. Weng, "Spallation Neutron Source Ring - Status, Challenges, Issues, and Perspectives," Proc. IEEE 2003 PAC Conf., Portland, OR, p. 571 (2003).
- [2] P.G. O'Shea and H.P. Freund, "Free-Electron Lasers: Status and Applications," *Science*, 292, 1853 (2001).
- [3] S. S. Yu, B. G. Logan, J. J. Barnard, F. M. Bieniosek et al, *Nucl. Fusion* 47, 721 (2007).
- [4] U. Linz and J. Alonso, *Phys. Rev. ST Accel. Beams* 10, 094801 (2007).
- [5] M. H. D. O. Sampa et al., *Radiation Physics and Chemistry* 71, 459 (2007).
- [6] I. Haber, G. Bai, S. Bernal et al, *Nucl. Instrum. Methods Phys. Res. A*, 577, 150 (2007).
- [7] M. Reiser, *Theory and Design of Charge Particle Beams*, (John Wiley & Sons, Inc., New York, 1994).
- [8] A. Friedman, "Simulation of Intense Beams for Heavy Ion Fusion," *Nucl. Instrum. and Methods Phys. Res. A* 544, 160 (2005).
- [9] R. A. Kishek, and D. Stratakis, Private Communication (2005).
- [10] R.A. Kishek, G. Bai, S. Bernal, D. Feldman, T.F. Godlove, I. Haber, P.G. O'Shea, B. Quinn, C. Papadopoulos, M. Reiser, D. Stratakis, K. Tian, C.J. Tobin, and M. Walter, "UMER: An Analog Computer for Dynamics of Swarms Interacting via Long-Range Forces," *Nucl. Instrum. Methods Phys. Res. A* 561, 266-271 (2006)

- [11] P.G. O'Shea et al., "The University Maryland Electron Ring (UMER)," Nucl. Instrum. Methods Phys. Res. A 464, 646-652 (2001).
- [12] Claude Lejeune and Jean Aubert, Adv. Electron. Electron Phys., Suppl. 13A, 159 (1980).
- [13] M.G. Minty and F. Zimmerman, Measurement and Control of Charged Particle Beams, Springer, Berlin (2003)
- [14] S. Bernal and D. Stratakis, unpublished data (2005).
- [15] S. G. Anderson, J. B. Rosenzweig, G. P. LeSage and J. K. Crane, "Space-charge effects in high brightness electron beam emittance measurements," Phys. Rev. ST Accel. Beams 5, 014301 (2002).
- [16] S. Humphries, Charged Particle Beams (Wiley Interscience, New York, 1990)
- [17] N. H. Abel, J. Reine Angew. Math. 1, pp153-157.
- [18] J. Radon, "On the determination of functions from their integral values along certain manifolds", Math. Phys. Klasse, 69, 262-277 (1917).
- [19] O. R. Sander et al., IEEE Transactions on Nuclear Science NS-26, 3417 (1979)
- [20] J. S. Fraser, IEEE Transactions on Nuclear Science NS-26, 1641-1645 (1979)
- [21] C. B. McKee, P. G. O'Shea, J. M. J. Madey, "Phase space tomography of relativistic beams," Nucl. Instrum. Methods Phys. Res. A 358, 264 (1995)
- [22] H. Oghaki et al., Nucl. Instrum. Methods Phys. Res. A 528, 366 (2004).
- [23] R. Conolly et al., Nucl. Instrum. Methods Phys. Res. A 443, 215 (2000).

- [24] V. Yakimenko, M. Babzien, I. Ben-Zvi, R. Malone, and X. -J. Wang, “Electron beam phase-space measurement using a high precision tomography technique,” *Phys. Rev. ST Accel. Beams* 6, 122801 (2003).
- [25] H. Li PhD Dissertation, “Control and Transport of Intense Electron Beams,” p102-p117, University of Maryland College Park (2004)
- [26] B. E. Carlsten, and D. T. Palmer, *Nucl. Instrum. Methods Phys. Res. A* 425, 37 (1999).
- [27] P. Piot, Y. -E. Sun, and K. -J. Kim, *Phys. Rev. ST Accel. Beams* 9, 031001 (2006)
- [28] P. A. Seidl, J. Armijo, D. Baca et al., *Nucl. Instrum. Methods Phys. Res. A* 577, 215 (2007).
- [29] D. P. Grote, J. W. Kwan, and G.A. Westenskow, *Nucl. Instrum. Methods Phys. Res. A*, 577, 58 (2007).
- [30] P. Seidl, C. M. Celata, A. Faltens, E. Henestroza and S. A. MacLaren, *Phys. Rev. ST Accel. Beams* 6, 090101 (2003).
- [31] H.E. Kandrup, C.L. Bohn, R.A. Kishek, P.G. O’shea, M. Reiser, and I.V. Sideris, “Chaotic Collisionless Evolution in Galaxies and Charged-Particle Beams,” *Annals of the New York Academy of Sciences* 1045, 12–33 (2005).
- [32] C. Nipoti, P. Londrillo, and L. Ciotti, *Mon. Not. R. Astron. Soc.*, 344, 748-760 (2003).
- [33] R.A. Kishek, P.G. O’Shea, S. Bernal, I. Haber, J. Harris, Y. Huo, H. Li, and M. Reiser, "The University of Maryland Electron Ring: A Platform for Study of

Galactic Dynamics on a Laboratory Scale," *Annals of the New York Academy of Sciences* 1045, 45-54 (2005).

- [34] B. E. Carlsten, *Nucl. Instrum. Methods Phys. Res. A* 285, 313 (1989)
- [35] X. Qiu, et al., *Phys. Rev. Lett.* 76, 4002 (1996).
- [36] D. Alesini, et al. *Nucl. Instrum. Methods Phys. Res. A* 568, 488 (2006).
- [37] D. H. Dowell et al., *Nucl. Instrum. Methods Phys. Res. A* 507, 327 (2003).
- [38] F.J. Sacherer, "RMS Envelope Equations with Space Charge", *IEEE Trans. Nucl. Sci.* NS-18, 1105 (1971).
- [39] M. Reiser, et al. *Proceedings of the 1999 Particle accelerator Conference*, New York, NY (IEEE, New York, 2007), p. 234
- [40] A. C. Kak, and M. Slaney, "Principles of Computerized Tomographic Imaging," New York, NY, IEEE Press, 1988.
- [41] D. Stratakis and R. A. Kishek, Private Communication (2006).
- [42] F. Zhou, A. Kabel, J. Rosenzweig, R. Agustsson, G. Andonian, D. Cline, A. Murokh, and V. Yakimenko, *Phys. Rev. ST Accel. Beams* 9, 114201 (2006).
- [43] D. Stratakis, R. A. Kishek, H. Li, S. Bernal, M. Walter, B. Quinn, M. Reiser, and P. G. O'Shea, *Phys. Rev. ST Accel. Beams* 9, 112801 (2006).
- [44] R.A. Kishek, S. Bernal, C.L. Bohn, D. Grote, I. Haber, H. Li, P.G. O'Shea, M. Reiser, and M. Walter, "Simulations and experiments with space-charge-dominated beams", *Physics of Plasmas* 10, 2016 (2003).
- [45] A. Kishek, S. Bernal, M. Reiser, M. Venturini, J. G. Wang, I. haber, and T. F. Godlove, *Nucl. Instrum. and Methods Phys. Res. A* 415, 417 (1998).

- [46] Haber, S. Bernal, C. M. Celata, A. Friedman, D. P. Grote, R.A. Kishek, B. Quinn, P.G. O'Shea, M. Reiser, and J.-L. Vay, "Collective Space-Charge Phenomena in the Source Region," Nucl. Instrum. Methods A 519, 396 (2004).
- [47] S. Bernal, R. A. Kishek, M. Reiser, and I. Haber, "Observations and simulations of transverse density waves in a collimated space-charge dominated electron beam", Phys. Rev. Lett. 82, 4002 (1999).
- [48] R. A. Kishek, P. G. O'Shea, and M. Reiser, "Energy Transfer in nonequilibrium space-charge-dominated beams," Phys. Rev. Lett. 85, 4514 (2000).
- [49] R. Noble and J. Spencer, 2007 Particle accelerator Conference, Albuquerque, NM (IEEE, New York, 2007) 3112
- [50] Bergoz Instrumentation, Espace Allondon Ouest 01630 Saint Genis Pouilly, France
- [51] B. Quinn et al. Particle 2003 Accelerator Conference, Portland, NM (IEEE, 2003) 2571
- [52] D. Stratakis et al. Proceedings of the 2007 Particle accelerator Conference, Albuquerque, NM (IEEE, New York, 2007), p. 2025.
- [53] I. Haber, et al. Particle accelerator Conference, Albuquerque, NM (IEEE, New York, 2007) 3564
- [54] M. Reiser, C. R. Chang, D. Kehne, K. Low, T. Shea, H. Rudd, and I. Haber, Phys. Rev. Lett., 61, 2933 (1988).

- [55] D. Kehne, Ph.D. Dissertation, "Experimental Studies of Multiple Electron Beam Merging, Mismatch, and Emittance Growth in a Periodic Solenoidal Transport Channel," University of Maryland, College Park (1992).
- [56] D. Sutter, Private Communication (2007).
- [57] D. Stratakis, K. Tian, R.A. Kishek, I. Haber, M. Reiser, and P.G. O'Shea, "Tomographic Phase-Space Mapping of Intense Particle Beams Using Solenoids," *Phys. Plasmas* 14, 120703 (2007).
- [58] Y. Cui, A. Valfells, S. Bernal, M. Reiser, P.G. O'Shea, R. A. Kishek, V. Yun, N. Rahimi, 2001 Particle accelerator Conference, Chicago, IL (IEEE, New York, 2007) p. 2976
- [59] R. A. Kishek and S. Bernal, UMER Technical Note E-RING-98-15 (1998)
- [60] S. Lund, and R. C. Davidson, *Phys. Plasmas* 5, 3028 (1998).
- [61] R. B. Fiorito and D. W. Rule, *AIP Conf. Proc.* 319, 21 (1994).
- [62] K. Tian et al, *Phys. Plasmas* 2008 (accepted for publication).
- [63] J.C. T. Thangaraj et al. Proceedings of the 2007 Particle accelerator Conference, Albuquerque, NM (IEEE, New York, 2007), p. 3570
- [64] B. L. Beaudoin et al. 2007 Particle accelerator Conference, Albuquerque, NM (IEEE, New York, 2007) 2322
- [65] K. Tian et al., *Phys. Rev. ST Accel. Beams* 9, 014201 (2006).
- [66] J. G. Wang et al., *IEEE Trans. Electron Devices* 37, 2622 (1990)
- [67] J. G. Wang et al. *All. Phys. Lett.* 62, 645 (1993)
- [68] S. Lund, et al. *Phys. Rev. ST Accel. Beams* 7, 024801 (2004)

